COMPLETE TEMPORAL MEASUREMENT OF LOW-INTENSITY AND HIGH-FREQUENCY ULTRASHORT LASER PULSES

A Dissertation
Presented to
The Academic Faculty

by

Travis Nathaniel Jones

In Partial Fulfillment
of the Requirements for the Degree
Doctor of Philosophy in the
School of Physics

Georgia Institute of Technology
December 2020

COMPLETE TEMPORAL MEASUREMENT OF LOW-INTENSITY AND HIGH-FREQUENCY ULTRASHORT LASER PULSES

Approved by:

Dr. Rick Trebino, Advisor
School of Physics
Georgia Institute of Technology

Dr. Ali Adibi
School of Electrical and Computer Engineering
Georgia Institute of Technology

Dr. Chandra Raman
School of Physics
Georgia Institute of Technology

Dr. Francisco Robles
W. H. Coulter Department of Biomedical Engineering and the School of Electrical and Computer Engineering
Georgia Institute of Technology

Dr. Carlos Silva
School of Chemistry and Biochemistry
School of Physics
Georgia Institute of Technology

Date Approved: [Nov. 17, 2020]

<u>Thinking</u>
If you think you are beaten, you are;
If you think you dare not, you don't.
If you'd like to win, but you think you can't,
It is almost a cinch you won't.

If you think you'll lose, you've lost;
For out in this world we find
Success begins with a person's will
It's all in the state of mind.

If you think you're outclassed, you are;
You've got to think high to rise.
You've got to be sure of yourself before
You can ever win the prize.

Life's battles don't always go
To the stronger or faster man;
But sooner or later the person who wins
Is the one who thinks he can!

-Walter D. Wintle

To all of those who think they can

ACKNOWLEDGEMENTS

TABLE OF CONTENTS

LIST OF FIGURES

LIST OF SYMBOLS

n_2	Nonlinear refractive index
λ_u	Wavelength light emitted by the undulator
L_u	Undulator period
γ	Relativistic Lorentz factor
λ_s	Wavelength of external source in "Seeded" Free-electron lasers
n	Harmonic integer number
t	Time
$\mathscr{E}(t)$	Temporal electric field of a laser pulse
$I(t)$	Temporal Intensity
ω	Carrier frequency
$\phi(t)$	Temporal phase
$E(t)$	Complex amplitude of the temporal electric field
$S(\omega)$	Spectral Intensity
$\varphi(\omega)$	Spectral phase
φ_1	Arrival time, group delay
φ_2	Group delay dispersion
$\mathscr{P}$	induced polarization
ε_0	Permittivity of free space
χ	Susceptibility
η	efficiency
d_{eff}	Effective nonlinear coefficient
I_{in}	Input irradiance

L	Crystal length
$\Delta\boldsymbol{k}$	Wavevector mismatch
$\boldsymbol{k}$	Wavevector
ρ	Poynting vector walk-off angle
n_e	Index of refraction for extraordinary beam
τ	Relative delay
$*$	Complex conjugate
$E_g(t-\tau)$	Gate function
E_{sig}	Nonlinear Signal Field
Z	Z error, minimized functional distance during phase retrieval
x	Steepest decent minimization factor
∇	Gradient
k	Iteration counter
G	Root-mean-squared difference between measured and retrieved traces
N	number of time/frequency points
μ	normalization constant
τ_p	Pulse length
τ_c	Coherence time
v_g	Group velocity
λ	Central wavelength
$\delta\lambda$	Bandwidth in wavelength
w_0	Focused beam spot size
$\delta\omega$	Bandwidth in angular frequency
θ	Half-crossing angle

I_{sig}	Intensity of the measured spectrogram, FROG Trace
$R(t)$	Non-instantaneous response function
$\delta(t)$	Instantaneous contribution to the response function
$\Theta(t)$	Non-instantaneous contribution
c_Θ	An adjustable complex constant used in the response function
$\mathscr{F}$	Fourier Transform
δt	Temporal range
w	Laser beam width
c	Speed of light
X_{sig}	Complex amplitude of the guess trace in derivative-free retrieval algorithm

LIST OF ABREVIATIONS

AC	Autocorrelation
BBO	Beta Barium Borate
BiBO	Bismuth Borate
BOXCARS	Box Coherent Anti-Stokes Raman Scattering
BPF	Bandpass Filter
BS	Beamsplitter
C.C.	Complex Conjugate
CG	Collinear GRENOUILLE
DFG	Difference Frequency Generation
EUV	Extreme Ultraviolet
FEL	Free-Electron Laser
FERMI	Free Electron laser Radiation for Multidisciplinary Investigations
FM	Flip Mirror
FROG	Frequency-Resolved Optical Gating
FWM	Four-Wave Mixing
GDD	Group-Delay Dispersion
GP	Generalized Projections
GRENOUILLE	Grating Eliminated No-Nonsense Observation of Ultrafast Incident Laser Light E-Fields
GVD	Group-Velocity Difference
GVM	Group-Velocity Mismatch
HGHG	High-Gain High Harmonic Generation
HS	Harmonic Separator

HWP	Half-wave plate
IAC	Interferometric Autocorrelation
IG	Induced-Grating
MOPA	Master Oscillator Power Amplifier
NIR	Near-Infrared
PG	Polarization-Gate
RANA	Retrieved-Amplitude N-grid Algorithmic
Ref	Reference
SASE	Self-Amplified Spontaneous Emission
SD	Self-Diffraction
SFG	Sum-Frequency Generation
SG	Standard GRENOUILLE
SH	Second Harmonic
SHG	Second-Harmonic Generation
TG	Transient-Grating
Unk	Unknown
UV	Ultraviolet
UVFS	Ultraviolet-Grade Fused Silica
XFEL	X-Ray Free-Electron Laser
XFROG	Cross-correlation FROG

SUMMARY

Two important frontiers in the field of ultrashort pulse measurement are the complete temporal measurement of low-intensity picosecond pulses in the near-infrared (NIR) and intense ultrashort pulses in the ultraviolet (UV) and extreme ultraviolet (EUV). The former are projected to find great use in the field of optical telecommunications, while the latter are the result of the relatively recent development of bright, coherent light sources in this wavelength range. The challenge in measuring weak pulses in the NIR is that many measurement techniques require expensive electronics and/or are complicated and difficult to align. UV pulse measurement on the other hand, due to the higher photon energies involved, is primarily hindered by slow light-matter interactions such as absorption or photoionization.

In this thesis, we develop and present two novel pulse-measurement techniques based on the widely-used method of Frequency-Resolved Optical Gating (FROG) which are aimed at addressing these challenges. The first technique, called Collinear GRENOUILLE, is an experimentally-simple and sensitive device which tests the sensitivity of second harmonic generation to measure low-intensity, picosecond pulses in the NIR. The measurement capabilities of Collinear GRENOUILLE are experimentally demonstrated by the successful measurement moderately complex pulses with femtojoule pulse energies at 800 nm. A similar measurement is also presented at 1030 nm where more efficient nonlinear crystals exist. The second technique, known as Induced-Grating Cross-correlation FROG, is designed to measure intense laser pulses in the UV and EUV. To demonstrate this technique, we first perform measurements of chirped 400 nm pulses in a

fast-responding nonlinear medium. We show that the resulting traces contain the complete electric field of the UV pulse we intended to measure. We further confirm these measurement by developing a modified phase-retrieval algorithm to reconstruct the pulse from the measured traces. Next, we performed similar measurements in a slowly-responding medium. FROG typically requires a fast nonlinear-optical processes to measure pulses, however once the response of the medium in accounted for, the measurements made using the IG XFROG technique indicate that accurate measurements of the pulse can still be made using a slow light-matter interaction. In the case of slow media, the IG XFROG technique is first demonstrated using absorption from amplified pulses at 400 nm and 267 nm. After establishing feasibility at these wavelengths, we applied this technique to EUV laser pulses from the FERMI free-electron laser at 31.3 nm, for which the dominant light-matter interaction is photoionization.

CHAPTER 1.

INTRODUCTION

1.1 Ultrashort laser pulses

Ultrashort laser pulses are extremely short bursts of light whose durations span from tens of picoseconds (1 picosecond = 10^{-12} seconds) to tens of attoseconds (1 attosecond = 10^{-18} seconds) [1]. Since the uncertainty principle dictates that short pulses in time must be broad in frequency, ultrashort pulses naturally have broad spectra. Additionally, due to their short durations, these pulses can be made to have very high peak intensities ($\sim 10^{12}$ W/cm^2). Such short bursts of light are not only scientific marvels in their own right, but also facilitate the production and study of other fascinating scientific phenomena.

Typically femtoseconds (1 femtosecond = 10^{-15} seconds) long, ultrashort pulses provide an "ultrafast camera" that enables the study and even manipulation of dynamic processes in materials on their own natural timescales. The field of Femtochemistry, for example, uses ultrashort laser pulses to study the dynamics of chemical reactions, processes which naturally occur on such ultrafast timescales [2]. Moreover, using temporally-shaped femtosecond laser pulses, the outcome of a chemical reactions can also be manipulated, in a process known as Coherent Control, to optimize the yield of one product and suppress the yield another [3]. In addition to chemical reactions, combinations of ultrashort laser pulses are also used in ultrafast spectroscopy techniques to study light-induced dynamics in a variety of other media [4].

Due to their high peak intensities, ultrashort laser pulses are also well-suited for other applications. For example, nonlinear optical processes such as second- and third-harmonic generation, and two- and three-photon fluorescence require the high intensities that are easily achieved with ultrashort pulses. Such nonlinear optical effects have not only been used to generate pulses at new frequencies [5], but have also been used to improve the resolution and depth in ultrafast microscopy, even allowing real-time imaging of biological processes in live specimen [6]. Another example is precision micromachining. When using ultrashort pulses, the optical breakdown threshold of many materials becomes well-defined. By focusing the pulse such that the intensity at the center of the focus is just above this threshold, energy deposition onto the material is more localized both in time and space when compared to conventional methods, resulting in smaller, more precise cuts and holes [7]. Additionally, such high intensity pulses can also be focused into gas jets to produce even shorter pulses, with even higher photon energies in a process known as high harmonic generation [1, 8-10].

While ultrashort pulses also find use in a great deal of other applications beyond those mentioned above, hopefully it is already clear to see that these pulses are versatile and vital tools in the advancement of scientific knowledge. Moreover, I hope to convey that optimizing the generation and characteristics of ultrashort laser pulses directly improves all of the application in which they are involved. As a result, inasmuch as it is important to develop better light sources, it is also important to develop techniques to characterize the pulses they emit. Thus, in this Chapter, a background knowledge of ultrafast lasers, ultrashort pulses, nonlinear optics, and ultrashort-pulse measurement is

established. Subsequent chapters will build upon this knowledge to introduce novel techniques for measuring low-intensity pulses in the near-infrared (NIR) and high-frequency pulses in the ultraviolet (UV) and extreme ultraviolet (EUV).

1.1.1   Generation

In the simplest case, a laser is a pumped cavity consisting of a gain medium surrounded by two mirrors: one highly reflective and one partially reflective. Indeed, the very first laser [11] was comprised of a ruby crystal with two parallel sides coated in silver and pumped with a high-powered flash lamp. Since then, several modifications to this simple design have been introduced in order to generate shorter and shorter pulses of light.

Starting with a continuous-wave laser, relatively shorter laser pulses can be generated by introducing a fast shutter into the laser cavity. Lasers lase when the total amount of gain is greater than that of the losses in the laser cavity. When a fast shutter is used in the cavity, the losses are first maximized, so that the laser does not lase and energy can build up in the gain medium. The losses are then suddenly minimized allowing the laser to lase and to generate significantly amplified, or "giant" laser pulses. When this modulation of the losses in the cavity, known as "Q-Switching" [12, 13], is repeated periodically, it can generate a train of such pulses. Fast Q-Switching can be achieved using a device known as a Pockels Cell and typically generates pulses ~10–100 ns long.

Even shorter pulses can be generated by introducing a light-absorbing medium, known as a saturable absorber into the laser cavity. As its name suggests, a saturable absorber exhibits an intensity–dependent absorption whereby light below its saturation intensity is heavily attenuated (i.e. absorbed) while light above the saturation intensity is

transmitted. Thus, during each trip around the laser cavity, the wings of the pulse, which are less intense, get attenuated, while the center of the pulse is transmitted and amplified. Attenuating the wings of the pulse has the effect of shortening the pulse on each trip around the laser. Using saturable absorbers, ultrashort pulses on the order of a picosecond have been generated [14].

Still shorter pulses have been generated by using a lasing medium with a high nonlinear refractive index, n_2. An intense beam of light, with a Gaussian beam profile for example, incident on such a medium experiences a refractive index change that depends on the local beam intensity. Larger intensities produce a larger change in the medium's index of refraction. As a result, the medium effectively acts as a lens that tightly focuses intense light, and loosely focuses weak light. This phenomenon is known as the optical Kerr effect, or Kerr-lensing [15]. By introducing optics to account for the additional focusing caused by the optical Kerr effect, the laser cavity can be aligned to collimate and amplify the intense portion of the beam while supressing the weak portion of the beam. Kerr-lensing, like saturable absorption, acts to intensify and shorten the pulse on each round trip. Pulse shortening is limited, however, by the dispersion caused by passing through the lasing medium and other optics in the cavity. Thus, a two prism pulse compressor [16] is also typically used to compensate for this dispersion. Lasers based on Kerr-lensing in a Titanium-doped Sapphire medium (Ti:Sapphire) [17] are a staple in the field of Ultrafast Optics. Very short pulses can be generated using Ti:Sapphire lasers [18], though they typically produce 1−10 nJ pulses ~10−200 fs long at 800 nm. Once generated, the energy of these femtosecond pulses can then be significantly increased via pulse

amplification techniques (see for example [19, 20]). Both unamplified and regeneratively

unamplified pulses from Kerr-lens mode-locked Ti:Sapphire lasers were used throughout

the work presented in this thesis.

1.1.2   A brief introduction to free-electron lasers

Since the first demonstration of a laser [11], the goal of many laser scientists has

been to develop laser sources that emit light in the EUV and X-ray regimes. To reach this

goal, significant effort has been devoted to the development of devices known as Free-

Electron Lasers (FELs) [21, 22]. Recently, with the advent of FEL facilities like those in

Germany [23], the U.S [24] and Italy [25], the goal of laser-like radiation in the EUV and

X-ray has been realized. During this work, I was granted the exciting opportunity to

perform measurements at the Free Electron laser Radiation for Multidisciplinary

Investigations (FERMI) facility in Trieste, Italy. Since these measurements will be

presented later in this thesis, it is potentially useful to understand (if only somewhat) how

these laser systems work as well.

Due to limitations in the reflectivity of optics in the EUV and X-ray range, FELs

emitting light in this wavelength range do not rely on cavities, but instead generate their

light via a single-pass though the laser. This process begins with generating an electron

bunch and accelerating it to speeds nearly approaching the speed of light via a linear

accelerator. Once the electron bunch has been accelerated to the desired speed, it is then

sent through a series of alternating magnets, known and as an undulator. For FELs that

operate under Self-Amplified Spontaneous Emission (SASE) [26-28], as the electron

bunch propagates through the undulator, the electrons in the bunch begin to spontaneously

emit light at a wavelength given by $\lambda_u \sim L_u/(2\gamma^2)$, where L_u is the period of the undulator, and γ is the relativistic Lorentz factor. As the electron bunch and this new wave continue to propagate, the emitted wave begins to "slice" the electron bunch into smaller bunches each separated by a distance equal to the wavelength of the emitted wave. This effect is known as microbunching. As the microbunched electrons continue to propagate through the undulator they continue to emit light at wavelength λ_u, but since they are more localized, they now do so in a more synchronized way [29]. This, in turn, leads to more microbunching (i.e. thinner, more localized slices still separated by λ_u) and significant amplification of the emitted wave. Proper choice of L_u and γ can readily yield light in the X-ray spectral range, while proper choice of the length of the electron bunch (in addition to other factors) can yield pulse durations in the fs range. Due to the spontaneous and noisy nature of the SASE process (the process starts from noise), SASE FELs typically exhibit considerable temporal instability from pulse to pulse. Approaches to reduce these fluctuations have been proposed [30] and recently implemented yielding significant improvements [31].

Alternatively, instead of relying on the spontaneous emission of the electron beam to kick-start the microbunching process, one could seed the process using coherent light from an external light source. Although coherent external light sources do not currently exist in the EUV/X-ray wavelength range, seeding is still possible via a process known as High-Gain Harmonic-Generation (HGHG) [32]. In an HGHG single-pass FEL, two undulators separated by a dispersive section are used to convert light at wavelength, λ_s, of the external source into light at one of its harmonics, λ_s/n, where n is an integer greater than

1 [33]. In the first undulator, the seed laser is used to modulate the energy of the electron beam. The dispersive section, usually comprised of four dipoles known collectively as a magnetic chicane, is then used to associate the energy of an electron to a longitudinal (i.e. temporal) position within the bunch. This causes the electrons to bunch up in a way similar to that of the SASE case. In this case however, the resulting microbunches carry spectral content at the harmonics of the seed laser. The pre-microbunched electrons are then sent through a second undulator which is tuned to amplify the light emitted at one of the harmonic wavelengths.

HGHG FELs are usually seeded with coherent light in the UV and are typically able to produce harmonics up to $n \sim 10$ (i.e. in the EUV). Even shorter wavelengths (soft X-ray) can be reached by allowing the output of an initial HGHG process to seed a second process [34]. Using a coherent light source to seed the FEL like in HGHG, provides the FEL with significantly improved temporal coherence and reduced power fluctuations when compared to SASE FELs. To date, FERMI is the only user facility to provide an FEL based on HGHG [35], and as such it provided an excellent temporally-coherent light source for the measurements provided later in this thesis.

1.1.3 *Mathematical description of ultrashort laser pulses*

Throughout this thesis, our goal will always be to develop a technique to measure the complete electric field of an ultrashort laser pulse. To do this, we start by first identifying the quantities we are trying to measure. Assuming the scalar approximation in which the light is considered to be linearly polarized, the electric field of a light pulse vs. time is given as

$$\mathcal{E}(t) \propto \frac{1}{2}\sqrt{I(t)}\exp(i[\omega_0 t - \phi(t)]) + C.C \,. \tag{1.1}$$

In Equation 1.1, and throughout this thesis, $I(t)$ refers to the pulse's temporal intensity, ω_0, refers to the carrier frequency, $\phi(t)$ refers to the pulse's temporal phase and "$C.C$" stands for the complex conjugate. In practice, the factor of ½, the factor containing the carrier frequency, and the complex conjugate are often dropped, and Equation 1.1 is reduced to the following,

$$E(t) \propto \sqrt{I(t)}\exp\left(-i\phi(t)\right). \tag{1.2}$$

The quantity $E(t)$ is known as the complex amplitude and is sufficient (and convenient) for doing calculations involving the electric field of a laser pulse.

We can also describe the pulse in the frequency domain. Taking the Fourier transform of $E(t)$ and shifting it to the pulse's central frequency yields the following expression:

$$\tilde{E}(\omega) \propto \sqrt{S(\omega)}\exp\left(-i\varphi(\omega)\right). \tag{1.3}$$

Much like in the time domain, an ultrashort laser pulse can be described in the frequency domain by its spectral intensity (i.e. spectrum), $S(\omega)$, and its spectral phase $\varphi(\omega)$. Since pulse propagation effects are more easily modelled by multiplication in the frequency domain, it is common to work with $\varphi(\omega)$ and to express it as the following Taylor series expansion:

8

$$\varphi(\omega) = \varphi_0 + \varphi_1 \frac{(\omega - \omega_0)}{1!} + \varphi_2 \frac{(\omega - \omega_0)^2}{2!} + \cdots \tag{1.4}$$

Although higher order phase terms are possible, the first three terms shown here are often sufficient to describe relatively simple ultrashort pulses. The quantity φ_1, in Equation 1.4, is given by $\left. \frac{d\varphi}{d\omega} \right|_{\omega_0}$ and is known as the group delay which is directly related to the pulse's arrival time. The quantity φ_2 is given by $\left. \frac{d^2\varphi}{d\omega^2} \right|_{\omega_0}$ and is known as linear chirp or group delay dispersion (GDD) which describes how the arrival time changes with frequency. A pulse can easily acquire positive GDD simply by propagating through a transparent medium like glass. Positive GDD causes higher wavelengths to precede lower wavelengths in the pulse while negative GDD has the opposite effect. An example of a positively linearly chirped Gaussian pulse is shown in Figure 1.1. As we can see from the plot of $E(t)$, the wavelength of the pulse is longer at negative times than it is at positive times. GDD is also clearly represented by the quadratic phase curves in the plots of $I(t)$ and $S(\omega)$. Notice here that without knowing the phase of the pulse, it would be unclear how the pulse differed from its transform limit. Clearly the phase provides additional information about the pulse that is not obvious from a plot of the pulse's intensity alone. Thus, to completely measure a pulse we will seek to measure both its intensity *and* its phase.
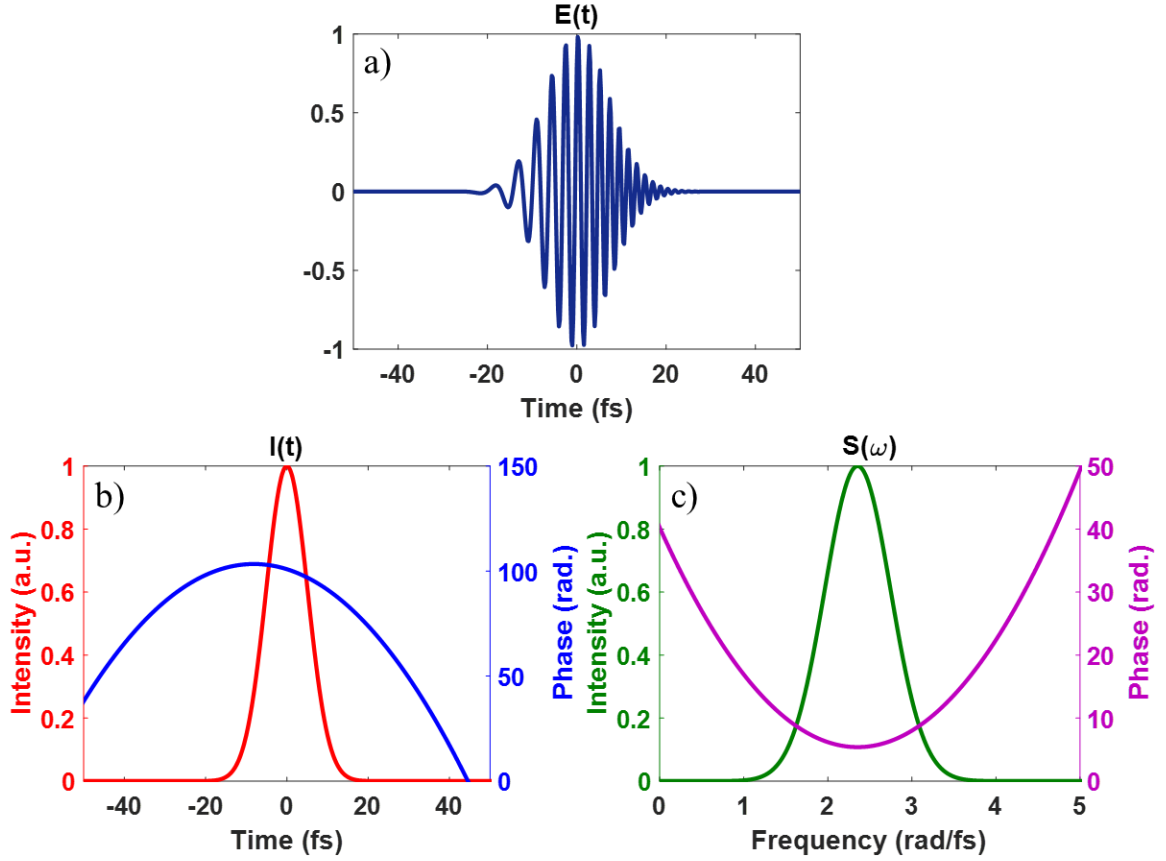
Figure 1.1 a) The electric field, b) temporal intensity and c) spectral intensity of a positively linearly chirped Gaussian pulse.

1.2 Brief discussion of relevant nonlinear-optical interactions

Nonlinear optics plays an important role in ultrafast optical science. Not only does it describe the phenomena through which ultrashort laser pulses are generated, but it also supplies a means to temporally and spectrally shape pulses, create pulses at new frequencies, and to measure the very pulses that it is used to create. In this Section, we will briefly discuss a few of the nonlinear optical processes central to the research presented in this thesis.

Very interesting optical effects can occur when a medium to responds to the strength of an external electric field in a nonlinear way. These effects can be described mathematically by accounting for higher-order contributions to an induced polarization in a the nonlinear medium. In Equation 1.5, the induced polarization, $\mathscr{P}$, has been written as a power series expansion of an external electric field, $\mathscr{E}$, up to third order.

$$\mathscr{P} = \varepsilon_0 \left[\chi^{(1)} \mathscr{E}(t) + \chi^{(2)} \mathscr{E}^2(t) + \chi^{(3)} \mathscr{E}^3(t) \right] \qquad (1.5)$$

1.2.1 Second-order effects

To visualize the nonlinear effects produced by the 2nd-order contribution to the nonlinear polarization, we simply multiply out the second term in Equation 1.5. If we allow the two factors of the field to come from two pulses with different frequencies, the result would contain terms with the following frequency components: $2\omega_1$, $2\omega_2$, $\omega_1 + \omega_2$, and $\omega_1 - \omega_2$ [5, 36]. The first two components result from each pulse interacting with itself to produce light with twice the input frequency. This nonlinear optical process is known as second harmonic generation (SHG). The third and fourth components result from the pulses interacting with each other to produce components equal to either the sum or difference of the two input frequencies. These interactions are appropriately named sum (SFG) and difference (DFG) frequency generation. Notice that frequency components of 2ω will also result from SFG when the frequencies of both pulses are the same. This result is also referred to as SHG and it will be fundamental to most of the research presented later in this thesis.

11

The efficiency, η, of an SHG process can roughly be described by the following proportionality [5, 36],

$$\eta_{SHG} \propto d_{eff}^2 I_{in} L^2 \text{sinc}^2(\Delta \boldsymbol{k} L/2) \tag{1.6}$$

where d_{eff} is known as the effective nonlinear coefficient of the medium, I_{in} is the irradiance of the fundamental input field, L is the thickness of the nonlinear medium, and $\Delta \boldsymbol{k}$ is the wavevector mismatch. From the above expression we see that choosing a medium with a large nonlinear coefficient, increasing the irradiance of the input field, increasing the thickness of the medium, and minimizing the wavevector mismatch are the main ways to optimize SHG conversion efficiency.

The wavevector mismatch, in SHG is given by $\Delta \boldsymbol{k} = 2 \, \boldsymbol{k}_{pol} - \boldsymbol{k}_{sig}$, where $\boldsymbol{k}_{pol}$ and $\boldsymbol{k}_{sig}$ are the wavevectors for the fundamental and second harmonic light respectively. When $\Delta \boldsymbol{k}$ is equal to zero, the process is said to be phase-matched and the sinc^2 factor in Equation 1.6 is maximized. Although perfect phase-matching, i.e. $\Delta \boldsymbol{k} = 0$, is only precisely achieved for one wavelength, approximate phase-matching can also be achieved for other nearby wavelengths. The range of wavelengths that achieve approximate phase-matching is known as the phase-matching bandwidth. Since ultrashort pulses have relatively broad spectra, broad phase-matching bandwidths are typically preferred to ensure that the entire spectrum of the pulse is phase-matched. Sufficiently broad phase-matching bandwidths are obtained in SHG by minimizing the product $GVM \times L$, where GVM is a quantity known as group-velocity mismatch and represents the difference in group velocity between the fundamental and second harmonic light in the medium. Minimizing this product is

12

achieved either by choosing a medium with small GVM and/or by making the medium very thin. In practice, phase-matching an SHG process is routinely achieved using thin birefringent nonlinear crystals such as Beta Barium Borate (BBO).

Indeed, thin crystals are most commonly used to perform SHG using ultrashort pulses, and as we have discussed, this will limit the efficiency of the SHG process. Later, however, there will be instances where thicker SHG crystals can be used without sacrificing phase-matching bandwidth. Though, as the crystal length increases, the SHG process will become more susceptible to another effect known as Poynting vector walk-off. Poynting vector walk-off, often called spatial walk-off, is a property of birefringent crystals which causes the energy of one beam (i.e. its Pointing vector) to propagate at an angle with respect to its wavevector. The angle between these two vectors is known as the walk-off angle and is given by Equation 1.8, where n_e is refractive index of the extraordinary polarized beam in the SHG crystal.

$$\rho = -\frac{1}{n_e}\frac{\partial n_e}{\partial \theta} \tag{1.7}$$

spatial walk-off acts to reduce the quadratic dependence on the crystal thickness in Equation 1.6 to a power less than two and thus reduce the overall efficiency of the SHG process [37]. We will consider this effect later on in this thesis when we investigate ways to maximize the SHG conversion efficiency and to measure very weak pulses.

1.2.2   3rd-order effects

If we again allow the three factors of the field to come from three different pulses and multiply out the 3rd-order term in Equation 1.5, we would find terms which carry a

variety of frequency components. Several components will be of the form, $\omega_1 - \omega_2 + \omega_3$, where one of the input frequencies is subtracted. Terms containing frequency components like this one are responsible for a variety of nonlinear effects, and particularly nonlinear-optically induced grating effects [38]. Induced grating effects are useful for a number of applications [39], and as we will see, they will be of particular interest for measuring ultrashort pulses. Later on, we will use an induced grating effect, known as a transient grating, to completely measure the electric field of ultrashort pulses in the UV and EUV.

1.3   Ultrashort laser pulse measurement

Ultrashort laser pulses are the shortest phenomena mankind has ever created. Because of this, their complete measurement has been a considerably challenging endeavor. The challenge can be described by a fundamental dilemma which is: to measure an event in time you need a shorter event. But if the event you are trying to measure is the shortest event around, then what do you use?

To solve this dilemma, we will make use of the nonlinear optical effects discussed in the previous Section and we will use the pulse to measure itself. In this Section, three pulse measurement techniques are discussed. The first two techniques are known as the intensity AutoCorrelation and Interferometric AutoCorrelation, which are not only important milestones in the field of ultrashort pulse measurement, but were critical to the development of the third technique known as Frequency-Resolved Optical Gating (FROG) upon which all of the novel research presented in this thesis is based.

1.3.1   Intensity Autocorrelation

In the early days of ultrashort pulse measurement, researchers had at their disposal two measures of the pulse. One was the spectrum of the pulse, and the other was its intensity autocorrelation. Since this is the only type of autocorrelation discussed throughout this thesis, the intensity autocorrelation will be referred to simply as the autocorrelation. Using the 2nd- and 3rd-order nonlinear-optical effects discussed in the previous Section, 2nd- and 3rd-order autocorrelations can be obtained. An experimental autocorrelation setup using SHG from two copies of the same pulse is provided in Figure 1.2. In an autocorrelation measurement, the pulse to be measured is first split into two copies using a beamsplitter. One copy of the pulse is then variably delayed with respect to the other using a translation stage. By spatially separating the beams as they pass through a lens, the two copies of the pulse are then simultaneously made to cross with a small angle, spatially overlap, and focus on to an SHG crystal.
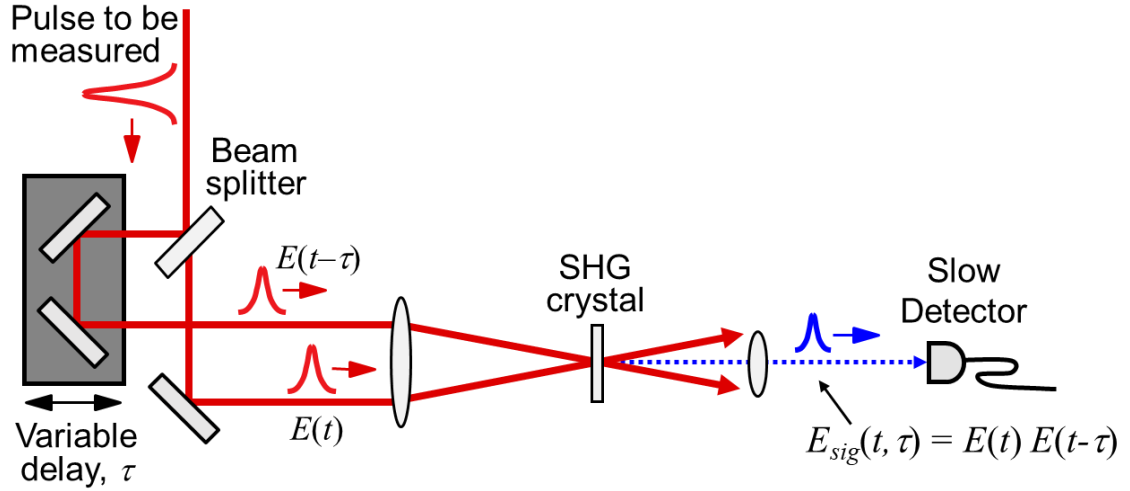
Figure 1.2 Exprimental setup for an Intensity Autocorrelator. Figure adapted from [36].

When the delay between the two copies of the pulse is large enough that the copies do not overlap in time, no SHG signal will be observed. Only when the copies temporally overlap will there be an SHG signal. Furthermore, the strength of the SHG signal will vary with the amount of temporal overlap between the two copies: the strongest signal occurring when the copies perfectly overlap in time, and weaker signals occurring when only the wings of the copies overlap. In autocorrelation measurements, the energy of the nonlinear signal is measured as a function of delay, τ, between the two copies of the pulse. This autocorrelation measurement is described mathematically by,

$$AC^{(2)}(\tau) = \int_{-\infty}^{\infty} |E(t)E(t-\tau)|^2 dt = \int_{-\infty}^{\infty} I(t)I(t-\tau)dt \qquad (1.8)$$

where the superscript "(2)" on the left side of the equation indicates the autocorrelation is of 2nd-order. As you can see from Equation 1.8, autocorrelation measurements only depend

on $I(t)$ and so do not contain phase information. Thus, if you are trying to measure the phase of your pulse, an intensity autocorrelation will not give you the information you are looking for. Additionally, if you are interested in obtaining the intensity, $I(t)$, of your pulse, this measurement cannot to provide that information either. Indeed, retrieving $I(t)$ from $AC^{(2)}$ is equivalent to the one-dimensional phase retrieval problem [38], and thus many different temporal intensities can produce the same autocorrelation. Moreover, as the pulse becomes more complicated, the autocorrelation of the pulse becomes simpler [38]. This quality of autocorrelation measurements has resulted in severe ambiguities and misinterpretations. Thus, at best, an autocorrelation measurement can only roughly approximate the duration of the pulse after a typical pulse shape is assumed.

1.3.2   Interferometric Autocorrelation
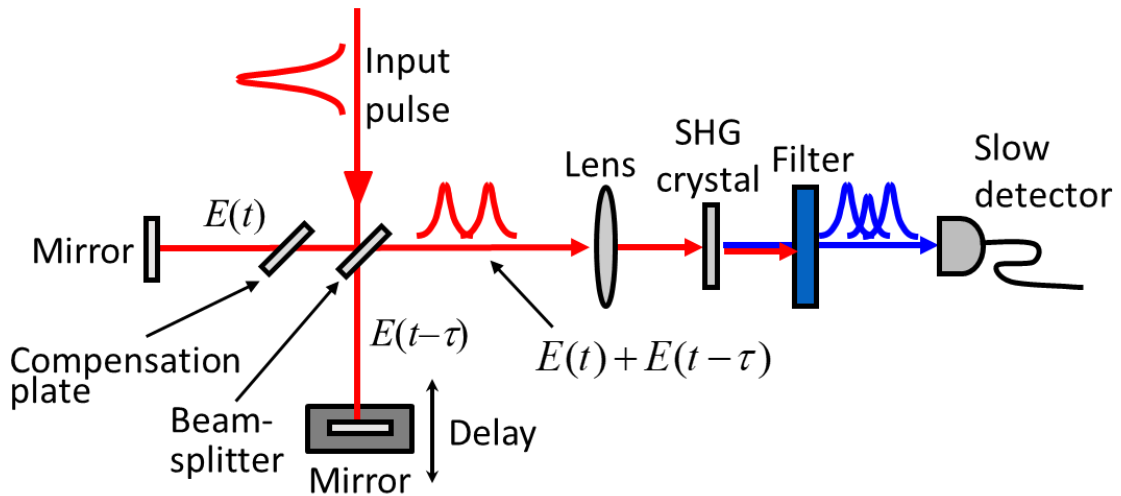
Figure 1.3 Experimental setup for an Interferometric Autocorrelator. Figure adapted from [36].

17

If we instead use a Michelson Interferometer to split and delay our pulses, we can allow the two arms of an autocorrelator to propagate collinearly as shown in Figure 1.3. This setup is known as an Interferometric AutoCorrelation (IAC), or Fringe-Resolved AutoCorrelation, arrangement. The particular IAC arrangement shown in Figure 1.3 could be called a "balanced" IAC since a compensation plate has been included to balance out the different amounts of dispersion caused by the beam passing through the glass of the beamsplitter once in one arm of the Michelson interferometer and thrice in the other. As in standard autocorrelation, interferometric autocorrelation also measures the energy of the nonlinear signal as a function of delay, τ. An IAC measurement is described mathematically by Equation 1.9.

$$IAC(\tau) = \int_{-\infty}^{\infty} |[E(t) + E(t - \tau)]^2|^2 dt \qquad (1.9)$$

To further investigate what information is provided by an IAC measurement we can expand Equation 1.9. This expansion yields the four quantities provided in Equation 1.10. Quantity a) is constant a background term resulting from the second harmonic of each individual pulse; quantity b) is the familiar form of the intensity autocorrelation from the previous Section; quantity c) is an interferogram of the pulse's electric field weighted by the sum of the intensities of the two copies of the pulse; and quantity d) is an interferogram of the second harmonic field, which after Fourier transform would yield the second harmonic spectrum provided that the measurement was made with sufficient resolution. Notice here that quantities a) and b) will not have an oscillatory term, while quantities c)

18

and d) will oscillate at ω and 2ω respectively. That fact that these terms oscillate with different frequencies will prove useful as we will later see.

$$IAC(\tau) = \text{a) } \int_{-\infty}^{\infty} I^2(t) + I^2(t-\tau)dt$$

$$\text{b) } + 4 \int_{-\infty}^{\infty} I(t)I(t-\tau)dt$$

$$\text{c) } + 2 \int_{-\infty}^{\infty} [I(t) + I(t-\tau)]E(t)E^*(t-\tau)dt + c.c$$

$$\text{d) } + \int_{-\infty}^{\infty} E^2(t)E^{*2}(t-\tau)dt + c.c$$

(1.10)

A simulated IAC measurement of an 800 nm 20 fs zero-phase Gaussian pulse is shown in Figure 1.4. Inspection of Figure 1.4(c) shows that an IAC trace has a couple of characteristic properties. The most obvious characteristic is that, as one of its names suggests, the trace has many finely-spaced fringes which carry the interferograms of Equation 1.10. The second noticeable feature is that the IAC trace has an 8:1 peak-to-background ratio. This 8:1 ratio is a direct result of the terms in Equation 1.10. Thus, in practice, an 8:1 ratio in an IAC measurement is a good indication that the measurement was performed correctly. Achieving an 8:1 ratio in the lab however, can be rather challenging because IAC requires careful alignment and thus can be difficult to align perfectly.

19
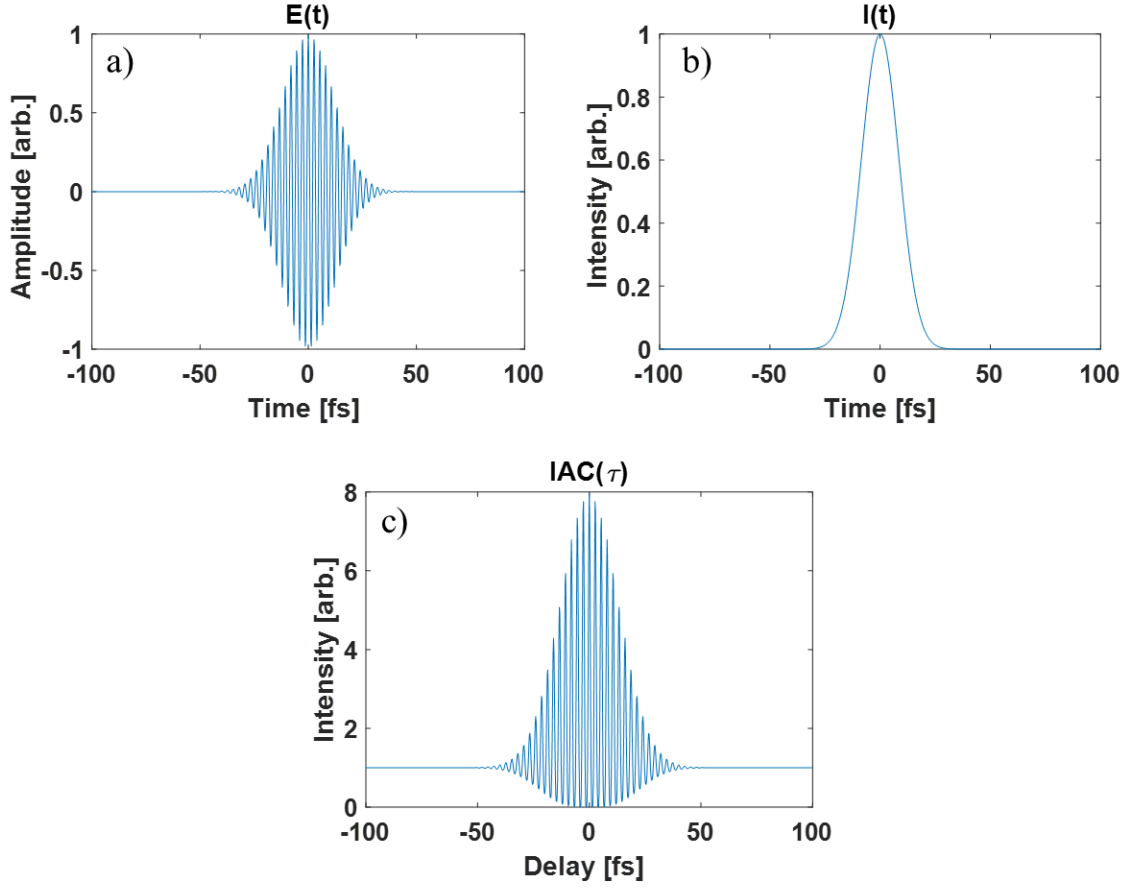
Figure 1.4 The a) the electric field b) Intensity and c) Interferometric Autocorrelation measurement of an 800 nm 20 fs zero-phase Gaussian pulse.

IAC was first demonstrated as a measurement technique for ultrashort pulses by Diels et. al in 1979 [40, 41]. Diels showed that IAC could provide some information about the chirp (i.e. phase) of the pulse via characteristic changes in the shape of the upper envelope of the IAC trace [41]. Early on it was thought that the pulse shape could be uniquely determined (up to the direction of time) using the information provided by the IAC together with the fundamental pulse' spectrum [42]. However is was later shown that even simple, clearly-distinguishable pulses yielded IACs that were so similar as to be effectively indistinguishable in practical situations [43]. And, like autocorrelation

measurements, as the complexity of the pulse increases, the IAC measurement of the pulse get simpler, making it impossible to reliably obtain $I(t)$ from a pulse's IAC.

1.3.3 Frequency-Resolved Optical Gating (FROG)

In the early 1990's the technique known as Frequency-Resolved Optical Gating (FROG) was first introduced [44]. An experimental setup for FROG based on SHG is shown in Figure 1.5. The experimental setup for FROG mimics that of the autocorrelator except for one key difference; the slow detector in the autocorrelator has been replaced by a spectrometer. Instead of measuring the energy of the signal as a function of delay, FROG measures the *spectrum* of the signal as a function of delay. Thus we can say that FROG, in its simplest and most general description, is any spectrally-resolved autocorrelation.
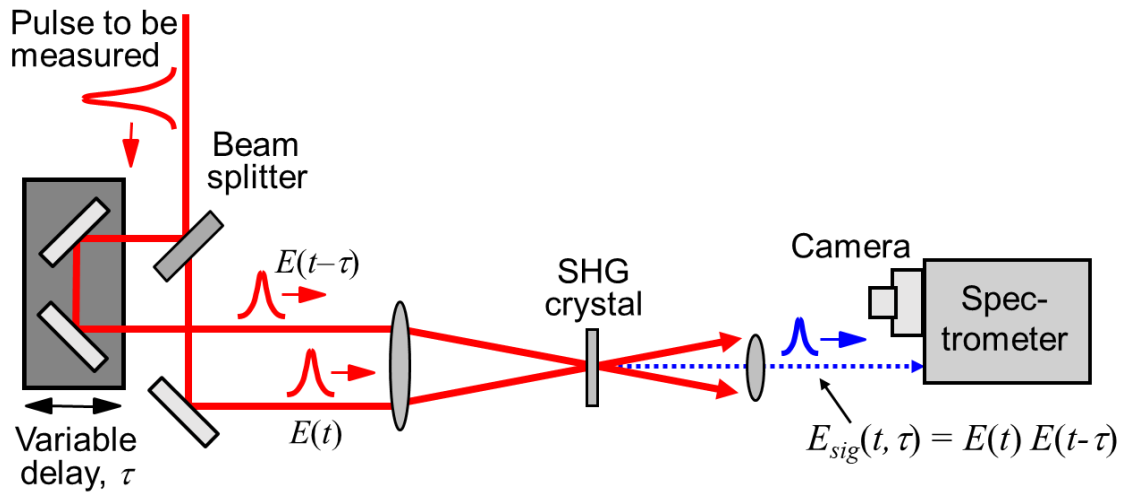
Figure 1.5 Experimental setup for Second-Harmonic Generation (SHG) FROG. Figure adapted from [36].

21

The SHG version of FROG shown in Figure 1.5 is the most sensitive and most commonly used version of FROG, but as the description given above suggests, FROG is a general technique, which can use also 2nd- and 3rd-order nonlinear processes [38]. Likewise, interferometric FROG has also been demonstrated [45, 46]. Simply put, FROG can use any fast (and even slow) nonlinear-optical process that produces a spectrally-resolvable signal.

Measuring the spectrum of the signal as a function of delay yields a frequency vs. delay plot of the pulse which is known as a spectrogram, or FROG trace. Mathematically, a FROG trace, is generally described by Equation 1.11.

$$I_{FROG}(\omega, \tau) = \left| \int_{-\infty}^{\infty} E(t)E_g(t - \tau) \exp(-i\omega t)\, dt \right|^2 \tag{1.11}$$

From Equation 1.11, we see that the FROG trace is given as the square magnitude of the Fourier transform of the pulse, $E(t)$, times a delayed gate function, $E_g(t-\tau)$. As mentioned, FROG works for a variety of nonlinear interactions and the gate function $E_g(t-\tau)$ depends on the nonlinear interaction being used. Since the product of $E(t)$ and $E_g(t-\tau)$ describes the signal field produced during a given nonlinear interaction, this product is typically referred to as E_{sig}. The signal fields, E_{sig}, for the SHG, Polarization-Gate (PG), and Self-Diffraction (SD) variations of FROG are provided in Equation 1.12.

$$E_{sig}(t, \tau) = \begin{cases} \textbf{SHG}: E(t)E(t - \tau) \\ \textbf{PG}: E(t)|E(t - \tau)|^2 \\ \textbf{SD}: E(t)^2 E^*(t - \tau) \end{cases} \tag{1.12}$$

PG and SD FROG are two examples of FROG variations based on the 3rd-order effects alluded to earlier in Section 1.2.2. A third induced grating effect known as a

22

transient grating is also commonly used in FROG. This variation is appropriately named Transient-Grating (TG) FROG. Depending on which pulse gets delayed however, standard TG FROGs can also be described by either the PG or SD signal field [38].

Once a spectrogram has been measured, FROG then employs an iterative phase-retrieval algorithm to reconstruct the intensity *and* phase of the pulse from the measured FROG Trace. This can be done because, unlike retrieval in the previously mentioned techniques, which equated to the ill-posed one-dimensional phase retrieval problem, retrieving the pulse from its spectrogram, i.e. FROG trace, is related to the *two-dimensional* phase retrieval problem for which an essentially unique solution exists [38]. Since we will undergo the process of adapting the FROG algorithm to suit a new signal field later in this thesis, it is beneficial to take some time now to describe the algorithm in some detail.

A general iteration in the algorithm works as follows: Using an initial guess for the pulse, we first generate $E_{sig}(t, \tau)$ for our nonlinear interaction according to Equation 1.12. We then take a 1D Fourier transform of this signal field to yield $\tilde{E}_{sig}(\omega, \tau)$, where the tilde indicates that we have taken a Fourier transform. Next, we enforce what is known as the data constraint on our guess. This step involves replacing the magnitude of our guess trace with the square root of the measured trace. Once this step is completed the guess trace is then inverse Fourier transformed to yield $E'_{sig}(t, \tau)$, where the prime indicates the magnitude replacement. This updated signal field is then used to make a better guess for the pulse and the process renews, ideally improving upon the guess for the pulse on each iteration.

In the generalized projections (GP) version of the FROG algorithm, the next guess for the pulse is generated by minimizing Equation 1.13 with respect to $E_{sig}^{(k+1)}$.

$$Z = \sum_{i,j=1}^{N} \left| E_{sig}^{(k)}(t_i, \tau_j) - E_{sig}^{(k+1)}(t_i, \tau_j) \right|^2 \qquad (1.13)$$

The minimization of Equation 1.13 is achieved using steepest decent minimization. First we calculate the negative gradient of Z with respect to $E^{(k+1)}(t_i)$. To do this we compute the following:

$$\nabla Z^{(k)} = - \left. \frac{\partial Z}{\partial E^{(k+1)*}(t_k)} \right|_{E^{(k+1)}(t_k) = E^{(k)}(t_k)} \qquad (1.14)$$

Next, using this derivative, we then update the field according to the method of steepest decent (where the negative sign has been included in Equation 1.14):

$$E^{(k+1)}(t_k) = E^{(k)}(t_k) + x^{(k)} \cdot \nabla Z^{(k)}(t_k) \qquad (1.15)$$

From Equation 1.15 we see that in order to update the field we must first solve for $x^{(k)}$. To do this we begin by substituting Equation 1.15 into Equation 1.13 for the given signal field. In the case of SHG FROG, for example, Equation 1.13 becomes:

$$Z = \sum_{i,j=1}^{N} \left| E_{sig}^{(k)}(t_i, \tau_j) - \left[E^{(k)}(t_i) + x^{(k)} \cdot \nabla Z^{(k)} \right] \left[E^{(k)}(t_i - \tau_j) + x^{(k)} \cdot \nabla Z^{(k)}(t_i - \tau_j) \right] \right|^2 \quad (1.16)$$

In this case, after fully expanding out Equation 1.16 we find that this equation becomes a 4th-order polynomial in $x^{(k)}$. The value of $x^{(k)}$ that minimizes Z can then be easily calculated by finding the global minimum of this polynomial. A similar process can be carried out for the other signal fields in Equation 1.12.

24

Finally, to assess the convergence of the algorithm, FROG then computes the rms. difference between the measured and retrieved traces. This error measure is called the "FROG" error, or "G" error and is defined as [38]:

$$G^{(k)} = \sqrt{\frac{1}{N^2} \sum_{i,j=1}^{N} \left| I_{FROG}(\omega_i, \tau_j) - \mu I_{FROG}^{(k)}(\omega_i, \tau_j) \right|^2} \qquad (1.17)$$

Since 1991, FROG has developed into an accurate, and highly reliable technique for measuring ultrashort pulses. Moreover, it has proven to be very general and capable of measuring pulses from the simple to the complex [47] and from the EUV [48] through the IR [49]. In the next two Sections we will discuss the two versions of FROG most relevant to the research presented in this thesis.

1.3.4 GRENOUILLE

After first showing that it was possible to measure the complete electric field of ultrashort laser pulses, one of the next steps for FROG was to make pulse measurement easy. In 2001, an experimentally simpler version of SHG FROG was introduced [50]. This version of FROG is known as GRating Eliminated No-Nonsense Observation of Ultrafast Incident Laser Light E-Fields, or GRENOUILLE, which means "frog" in French.

To simplify the experimental setup for SHG FROG, GRENOUILLE made two key innovations. The first innovation was the use of a Fresnel Biprism. A Fresnel biprism is simply a prism with a very large apex angle, the function of which is shown in Figure 1.6.
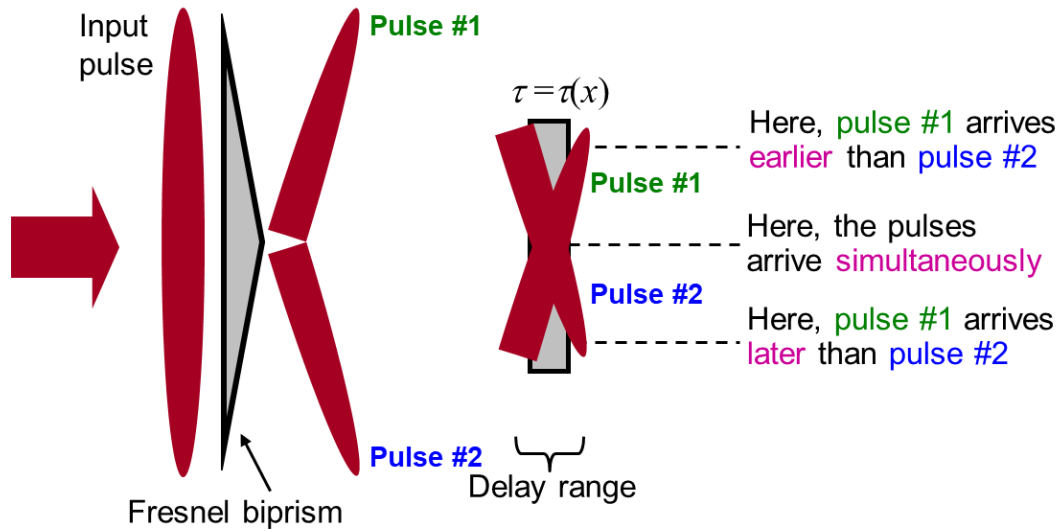
Figure 1.6 Simultaneously splitting and crossing two beams using a Fresnel biprism. Figure adapted from [36].

Sending a wide beam through a Fresnel biprism naturally splits the beam into two halves and crosses them at an angle. What's more, as the beams cross, they also create a range of delays as shown in Figure 1.6. Splitting, crossing, and variably delaying two copies of a pulse is exactly what is done in a standard SHG FROG. Thus, the beamsplitter, mirrors, and delay stage in standard SHG FROG can all be replaced by a single optic, the Fresnel biprism.

The second innovation in GRENOUILLE is the use of a thick SHG crystal. As we have discussed before, GVM limits phase-matching bandwidth, so the SHG crystals used in FROGs are typically kept thin. However, if we allow the crystal to be thick, very narrow phase-matching bandwidth results. Since phase matching in SHG depends on the angle of the input beam with respect to the crystal's optic axis, this means that for a given input angle we only get a very narrow portion of the SH spectrum at that particular angle. Thus,

if we increase the range of divergence angles in the beam by focusing tightly into the SHG crystal, it is easy to envision that we will get range of different exit angles and hence different wavelengths exiting the crystal at these different angles [50, 51]. Placing a lens one focal length after the crystal then allows us to map crystal exit angle (i.e. wavelength) to position on a detector and spectrally resolve the SH light. Spectrally resolving the SHG signal is exactly what the spectrometer does in the standard SHG FROG! Thus, a sufficiently thick crystal can naturally be used to replace the spectrometer in SHG FROG.

So how does GRENOUILLE's thick crystal work? Well, since the crystal's phase-matching bandwidth determines GRENOUILLE's spectral resolution, the following condition must be satisfied:

$$GVM \times L \gg \tau_p$$

(1.18)

where τ_p is the pulse length. This expression ensures that the phase-matching bandwidth of the crystal is smaller than (and hence able to resolve) the bandwidth of the pulse. It is worth noting that this is opposite of the condition typically used in FROG, where we would want the phase-matching bandwidth to be broader than the pulse's spectrum. In addition to having sufficient resolution in GRENOUILLE, we would also like to make ensure that the crystal does not significantly broaden the pulse and wash out any of its fine temporal structure. To ensure this, the following condition must also be satisfied:

$$GVD \times L \ll \tau_c \,.$$

(1.19)

In Equation 1.19, *GVD* is known as the group velocity *difference* and is given by

$\frac{1}{v_g(\lambda_0-\delta\lambda/2)}$ - $\frac{1}{v_g(\lambda_0+\delta\lambda/2)}$ where $\delta\lambda$ represents the bandwidth of the pulse, and τ_c represents the pulse

coherence time, which describes the shortest temporal feature in the pulse.

With as few as four optics: a cylindrical focusing lens, a biprism, a thick crystal and

another lens, GRENOUILLE is very simple device able to measure ultrashort laser pulses

on a single-shot. GRENOUILLE works well for measuring moderately complex fs pulses

with pulse energies in the nJ to pJ range. In later Chapters, we will seek to extend

GRENOUILLE's capabilities to be able to measure ps pulses with pulse energies in the fJ

range.

1.3.5 Transient-Grating FROG
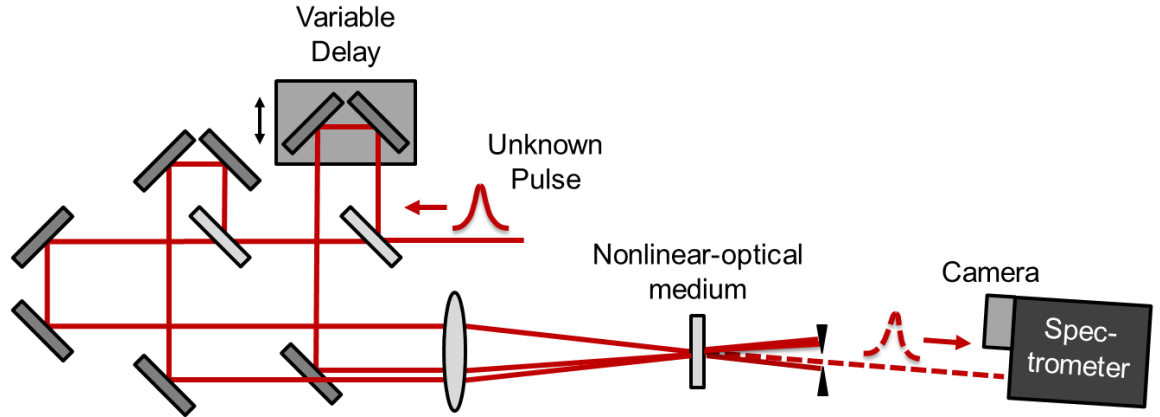
Figure 1.7 An experimental setup for Transient Grating FROG.

A schematic of a TG FROG apparatus is shown in Figure 1.7. In a standard TG

FROG measurement, two copies of an unknown pulse are used to generate an interference

pattern (i.e. grating) in the nonlinear-optical medium, while a third copy of the pulse is

28

variably delayed and diffracted from this grating. And as usual the spectrum of the diffracted beam is measured as a function of delay.

Transient Gratings are also a phase-matched nonlinear-optical effect. Here, considering the case where all three pulses have distinct frequencies Δk can be written as $\Delta k = k_1 - k_2 + k_3 - k_{sig}$, where k_i represents the wavevector of the ith input beam and k_{sig} is the wavevector of the signal beam (dashed line in Figure 1.7). In the case of degenerate beams, where two pulses of wavelength λ_{excite} create the grating, and a pulse of wavelength λ_{probe} diffracts, it can be shown that achieving $\Delta k = 0$, is equivalent to satisfying a condition known as the Bragg Condition which states that $\sin \theta_{probe} = \frac{\lambda_{probe}}{\lambda_{excite}} \sin \theta_{excite}$. Here, θ_{probe} and θ_{excite} are the half-crossing angles of the probe and excite beams. From the Bragg condition, we can see that phase-matching can be directly achieved via proper choice of beam geometry. In the case of fully degenerate beams, a beam geometry known as the BOXCARS geometry [52] is usually used. Here, the three input beams are aligned so that they are co-parallel and form three corners of a square at the lens. After the nonlinear medium, the signal beam emerges at the fourth corner of the square. Using the BOXCARS geometry, it is easy to show that the beam whose wavevector gets subtracted in the expression for Δk given above is the beam diagonally opposite the signal beam. This subtraction in the phase matching equation results in a complex conjugation in the signal field. Thus generally, the Transient Grating signal field is given by: $E_{sig} = E_1 E_2^* E_3$. In the fully degenerate case it is easy to show that depending on which pulse is delayed, either the PG or SD signal field will be obtain obtained.

1.3.6   Cross-Correlation FROG

In the previously mentioned FROG techniques, the unknown pulse is used to measure itself, in what is known as a self-referenced measurement. However, once a pulse has been measured, if it is relatively simple, it can be used to measure a more complex pulse. In this case, the previously measured simple pulse acts as the reference pulse for the more complex pulse. This technique is known as Cross-Correlation FROG [53]. Cross-Correlation FROG or "X" FROG has been used extensively to measure a wide variety of pulses. Indeed, XFROG has been demonstrated using DFG [53], SFG [54], PG [55], TG [56] and other nonlinearities [57, 58]. The methods discussed in Chapters 3-5 make use of a novel combination of Transient Grating and Cross-Correlation FROG which we have called Induced-Grating XFROG.

CHAPTER 2.

Content in this Chapter originally appeared as two papers:

Travis Jones, Peter Šušnjar, Rok Petkovšek, Rick Trebino, "High-Sensitivity, Simple Frequency-Resolved-Optical-Gating Device," IEEE Journal of Quantum Electronics, 56, 3, 1-6, (2020).[59]

and

Peter Šušnjar, Travis Jones, Rick Trebino and Rok Petkovšek, "Crystal-Configuration Considerations for Higher-Sensitivity Picosecond-Pulse SHG FROG," in IEEE Journal of Quantum Electronics, vol. 56, 2, 1-8, (2020).[60]

2.1 Motivation

Ultrashort laser pulses require detailed intensity-and-phase measurement in order to achieve the required degree of control over the pulse. Such measurement techniques are now readily available. However, an important frontier in this field is the measurement of low-intensity light pulses with energies of ~10 fJ, especially those with relatively long pulse lengths of ~10 ps. For example, such pulses will likely play key roles in next-generation optical telecommunications. Weak pulses can also occur when only a small fraction of the power is available for measurement in a continuous monitoring arrangement in which the bulk of the pulse energy is required for an application. Also, fiber lasers, which necessarily have small beam areas, often emit low-energy ps pulses that are too weak to measure with current pulse-measurement techniques. Finally, a common approach for many additional applications of short-pulse laser systems is to begin with a low-pulse

energy oscillator, whose characteristics can be manipulated with ease, and then amplify the resulting pulses to high energies in one or more amplifier stages (so called MOPA –master oscillator, power amplifier configuration). For flexible operation, a gain-switched diode can also be implemented as the oscillator, which is typically highly chirped and therefore requires custom chirp compensation to reach the desired shorter pulse duration [61]. However, if the oscillator pulse cannot be measured, it is difficult to know what to do when the measurable high-energy pulse lacks the desired properties: which device is at fault, the oscillator or the amplifier? Measuring pulses directly from a laser requires a self-referenced technique, and a reliable and general such technique is frequency-resolved optical gating (FROG) [38, 62-64]. FROG, like essentially all other pulse-measurement techniques, however, was designed for measuring pulses from relatively high-power fs lasers. These methods typically require the use of thin nonlinear-optical crystals and so cannot measure weak pulses.

A practical self-referenced technique for the complete measurement of weak ps pulses has been a long-standing unsolved problem that has attracted numerous extremely clever, yet only partial, solutions. For example, fast detectors and ultrahigh-bandwidth oscilloscopes are common, but such oscilloscopes are extremely expensive (>$100,000), fragile, and complex; they yield only the pulse intensity and not the phase; and they lack the temporal resolution to measure pulses shorter than ~50 ps, far too slow for many applications. In addition, many techniques can measure very weak pulses [65, 66], but they require a previously measured reference pulse. One self-referenced method, a version of FROG, has been shown capable of measuring extremely weak (~1 fJ), fs pulses, but it

requires an aperiodically poled LiNbO$_3$ waveguide in order to achieve a long interaction length in the nonlinear medium for greater sensitivity, which is difficult to work with, expensive, and not readily available [67, 68]. Another version of FROG has achieved pJ sensitivity using an optical fiber as the nonlinear medium, but it is difficult to align and involves detection at the input wavelength (typically 1.5 μm), which requires an expensive IR camera [38, 69]. Others use high-speed modulators or other ultrahigh-bandwidth electronics, which are also very expensive [70-77]. Still others involve very complex apparatuses, such as tomography [78]. Some involve techniques that only measure the coherent artifact and so cannot distinguish a stable train of short simple pulses from an unstable train of longer more complex pulses [79].

Thus, it has simply not been possible to measure the complete intensity and phase of weak laser pulses in a way that is both reliable and practical. The lack of such a technique discourages laser-system monitoring and severely complicates potential new telecommunications approaches, in which details of the pulse's intensity and phase (e.g., phase-shift-keying) often play key roles. In this Chapter we present two practical, self-referenced, and highly sensitive FROG techniques for measuring weak fs and ps pulses in time.

2.2   A sensitive GRENOUILLE Device for weak pulses at 800 nm

In this section we introduce the Collinear GRENOUILLE (CG), to be distinguished herein from Standard GRENOUILLE (SG). Like SG, CG also uses the natural angular phase-matching dispersion of a thick crystal to provide the necessary spectral resolution to measure a pulse [50, 51]. Sufficient spectral resolution is still achieved by ensuring that the

product of the group-velocity mismatch (GVM) between the fundamental and SH light, and the interaction length of the crystal, L, is much larger than the temporal length of the measured pulse, τ_p : GVM $\times$ L $\gg \tau_p$. The length of the crystal is instead limited by the much less stringent condition involving group-velocity dispersion (GVD) between the extreme wavelengths in the bandwidth of the fundamental pulse. As a result, we ensure that GVD $\times$ L $\ll \tau_c$, where τ_c is the coherence time (the duration of the shortest temporal structure) of the input pulse, as in SG.

To enable the measurement of such long, weak pulses, we replace SG's Fresnel biprism and line-focus beam geometry with a collinear point-focus beam geometry and optimal focal-spot size. This improves the device efficiency by increasing the intensity of the input pulse at the nonlinear crystal. We note that using a collinear geometry and scanning the relative delay with a traditional translation stage sacrifices SG's single-shot functionality, but for the high-rep-rate (up to 100 GHz) trains of weak pulses typically encountered, single-shot operation is inappropriate and is always sacrificed for improved sensitivity. Indeed, even without its single-shot capability, GRENOUILLE, like other FROG variations, can still tell whether a given pulse train is stable and provide the best available measurement of the typical pulse in that case [62-64]. Furthermore, when using a collinear geometry, one could generate an "interferometric FROG" (IFROG) trace [46]. Such fringe-filled traces have been used for few-fs pulses and have some advantages for such extremely short pulses. However, collecting such a fringe-filled trace for, say, a ~10 ps pulse, increases the data collection time, and is not necessary since a standard SHG FROG trace already yields a complete temporal measurement of the pulse without the

fringes. For these reasons, we believe these fringes should be removed, and they can be, by carefully under-sampling the IFROG trace [45], Fourier filtering [45], or dithering one arm of the interferometer [67]. To demonstrate, in the two measurements reported here, we performed one fringe-resolved measurement, where we used Fourier filtering to remove the fringes and extract the SHG FROG trace as in [45], and one where the fringes were washed out by dithering the fixed arm of the interferometer as in [67].

We also note that measuring pulses also requires efficient conversion of the complete spectrum of the pulse. In birefringent nonlinear crystals, phase-matching is fulfilled for a single wavelength at a single angle relative to the crystal's optical axis due to angular variation of the extraordinary refractive index. By focusing the beam tightly into a nonlinear crystal, sufficient divergence of the beam can be used to cover all of the phase-matching angles within the spectrum of the pulse. However, the same angular variation also produces spatial walk-off between the fundamental and second-harmonic beams and consequently reduces conversion efficiency. Thus, when selecting the focusing conditions there is a trade-off between the shortest measurable pulse and the weakest measurable pulse. Simply put, the tighter the focusing, the shorter the pulse (i.e. the more broadband a pulse) that can be measured, while focusing more loosely provides a longer interaction length and better conversion efficiency, enabling the measurement of weaker pulses.

This tradeoff was investigated in [60] and an optimal focusing condition, provided in Equation 2.1, was obtained, where w_0 is the spot size, ρ is the walk-off angle and $\delta\omega$ is the pulse bandwidth in angular frequency.

$$w_0 < \frac{4\tan(\rho)}{GVM\delta\omega} \qquad (2.1)$$

2.2.1 Experimental Setup
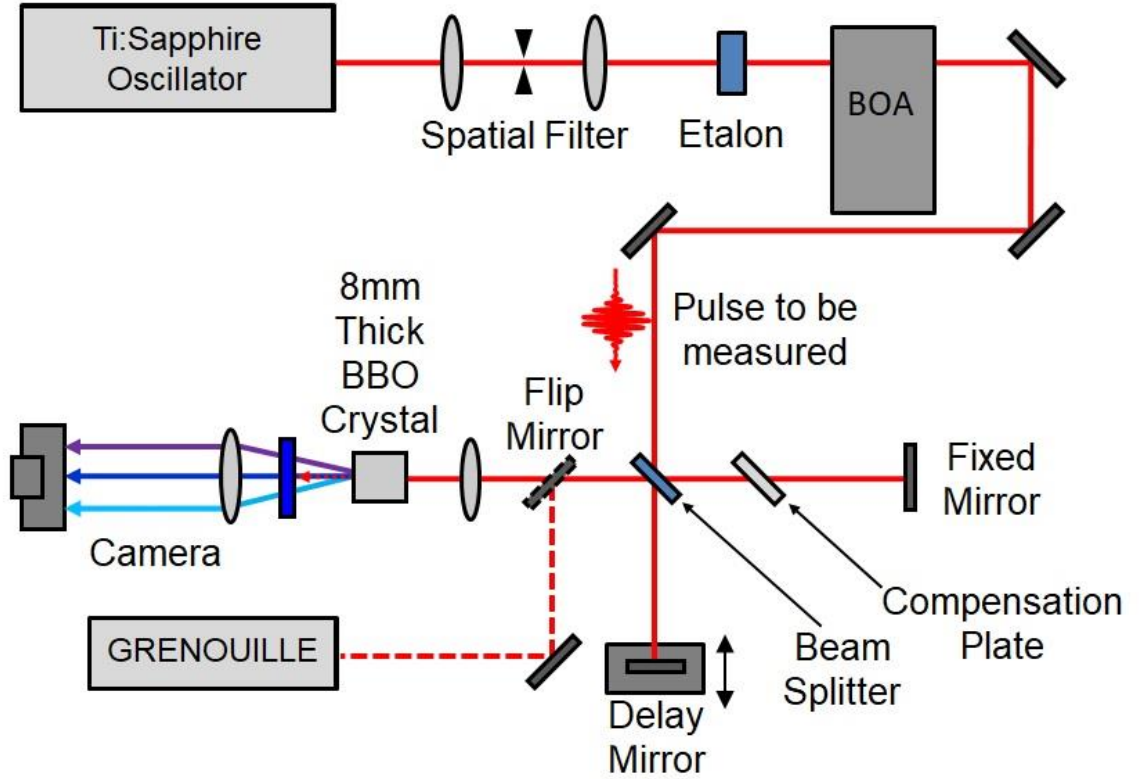
Figure 2.1 Experimental setup used in proof-of-principle demonstration of Collinear GRENOUILLE (CG).

To test our device, we performed two experiments using the output of a KM Labs Ti:Sapphire oscillator, which emitted ~7.5 nJ pulses with 30 nm bandwidth FWHM at a repetition rate of 90 MHz. In the first experiment, we tested our device's ability to measure complex pulses at relatively high pulse energies and compared it to an SG device. The experimental setup is shown in Figure 2.1. We generated a complex pulse by sending the

output of our oscillator through a 23.8 μm-spaced etalon with 50% reflectivity on both surfaces. This created a pulse consisting of a series of pulses each separated by 159 fs. A Swamp Optics BOA compressor was then used to compensate for the group delay dispersion in the setup.

In this first experiment, the input pulse energy was relatively high, around 550 pJ. This first experiment serves as a proof-of-principle measurement of the CG technique. Our CG used a balanced Michelson interferometer in which the beams were split and recombined using a 3-mm-thick 50/50 plate beam-splitter made of N-BK7 glass. Dispersion between the arms of the Michelson was balanced using a 3-mm-thick anti-reflection coated compensation plate of the same material. A Newport MFN25PP translation stage was used to vary the length of the delay arm of the Michelson interferometer. A flip mirror was placed after the beam-splitter of the Michelson to allow for easy transition between CG and SG measurements. For the 30 nm bandwidth pulses measured in this initial demonstration, the task of ensuring complete phase-matching was given priority over conversion efficiency, so a relatively tight focus was used to cover the relatively large range of phase-matching angles involved. Thus, when the flip mirror was out of the beam path, the beams were focused relatively tightly using a 50 mm spherical lens onto an 8 mm Type-I BBO. The unconverted fundamental light was removed using a bandpass colored glass filter (Thorlabs, FGS900-A) while the frequency-resolved SH light was mapped onto a Pixelink Pl-A741 camera using a 15 cm spherical lens. A CG trace was captured by scanning the delay arm of the Michelson 5000 steps at the finest step size which was 0.49 fs. This measurement took roughly 85 min to complete. A pause of ~0.7 s

37

was used to let the stage settle before acquiring the spectrum at each delay. It is worth noting here that this acquisition time could be significantly reduced if a fast camera and stage combination similar to that in [46] is used. Later, a conventional SHG FROG trace was extracted from the CG trace using Fourier filtering and background subtraction [45]. After the CG measurement, the delay mirror was placed near zero delay, the flip mirror was placed in the beam path, and the fundamental light was then measured using a standard Swamp Optics GRENOUILLE (8-50).

In the second experiment, we tested the measurement sensitivity of our device by measuring a weak double-pulse with 1.3 ps separation. The setup is shown in Figure 2.2. In this experiment, the output of our oscillator was sent through a 5 nm bandpass filter and an additional Michelson interferometer, which was used to generate the double pulse. The pulse was attenuated using a pair of variable attenuators, such that the measured average power before entering the measurement apparatus was reduced to 4.3 µW. Given our 90 MHz repetition rate, this yields an average double-pulse total energy of nearly 48 fJ and thus a measurement sensitivity of ~24 fJ per pulse.
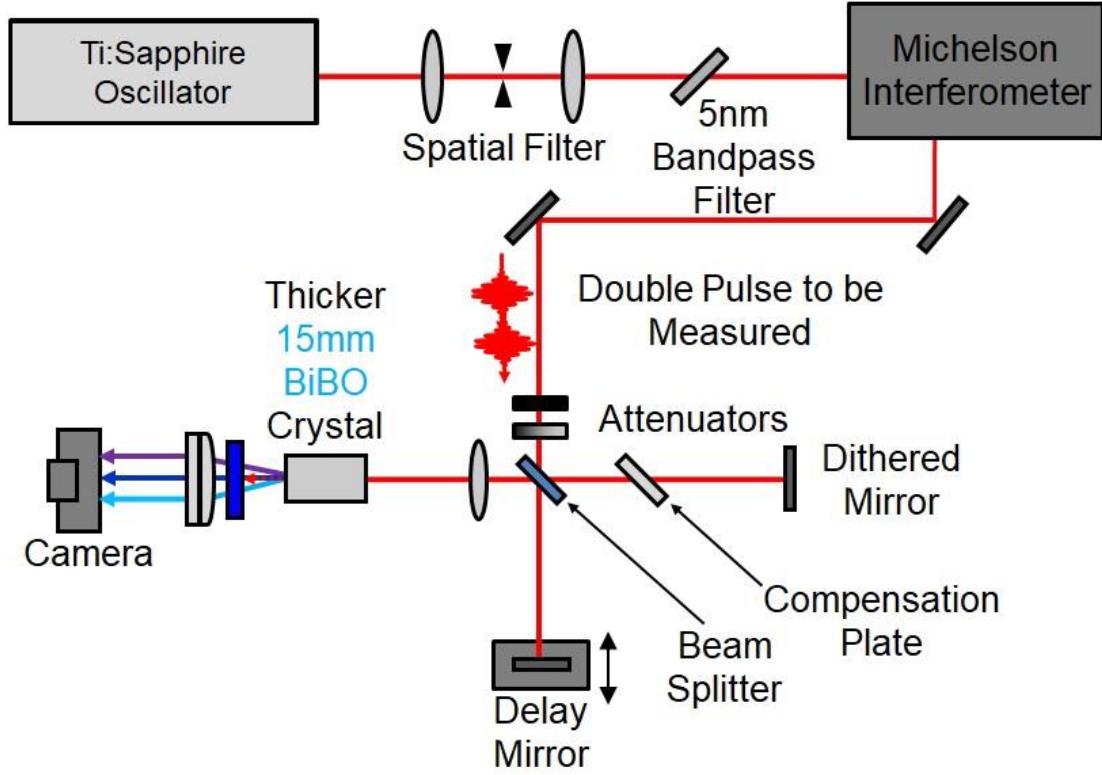
Figure 2.2 Experimental setup used in second (more sensitive) demonstration of CG.

Due to its higher nonlinear coefficient, higher GVM, and lower Poynting vector walk-off angle near 810 nm compared to BBO [80], in this measurement, we used a 15 mm BiBO crystal as the SHG crystal. We also used a 100 mm lens to focus the beams into the crystal. As mentioned, the size of the beam at the focus is an important parameter to consider, because it impacts both phase matching and conversion efficiency. Although we did not measure the profile of the focused beam using the 100 mm lens, we did make two such measurements using a 150 mm and 125 mm focusing lens which yielded FWHM beam diameters of 38.3 μm and 32.8 μm, respectively. Based on these measurements, we estimate the spot size using the 100 mm lens to be 27 μm±2 μm. Using the methods

discussed in [81] and [60] we estimate in Figure 2.3(a) the spectral resolution and in Figure 2.3 (b) the phase-matched SH bandwidth vs. focused beam diameter. Specifically, we estimate that our 27 μm spot size should yield a spectral resolution of ~0.077 nm and support ~1.6 nm of SH bandwidth—an SH bandwidth close to that expected from our spectrally narrowed pulse (~1.7 nm). Furthermore, this spot size yields a confocal parameter, $b = 2\pi n w_0^2/\lambda_0$, of 10.3 mm and an L/b ratio of ~1.46 which is should also be close to the theoretical value for optimal conversion efficiency according to [82], where our A and B are approximately 40 and 14 respectively.
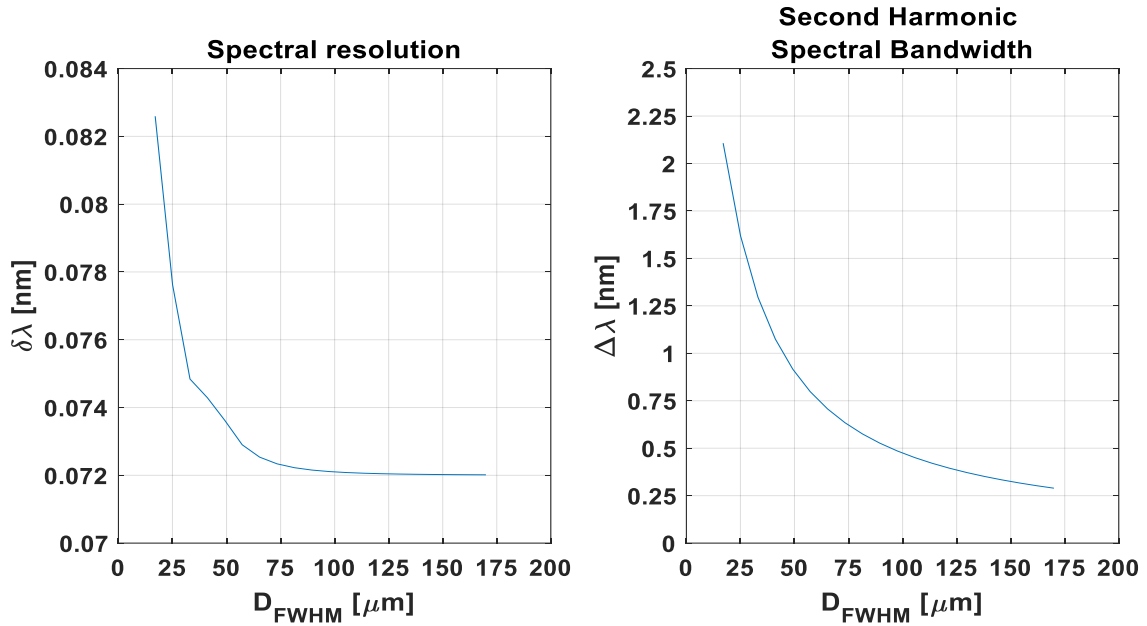
Figure 2.3 Theoretical plots of (a) spectral resolution and (b) phase-matched second harmonic (SH) spectral bandwidth (FWHM) vs. focused beam diameter using a 15mm BIBO crystal. A spot size of 27 μm phase matches ~1.6 nm of SH bandwidth.

Following the crystal, vertical and horizontal cylindrical lenses—with 100 mm and 50 mm focal lengths respectively—were also introduced to form a makeshift anamorphic lens placed 10 cm after the focus. The vertical lens, placed one focal length away, mapped

40

wavelength onto position on a detector, while the horizontal lens imaged the second harmonic light from the crystal onto only 4-5 pixels of our sensor in the non-critical dimension thus improving our signal to noise ratio. To remove the interferometric fringes in this measurement, we dithered the fixed arm of the measurement apparatus by attaching a piezo chip to the fixed mirror and driving it with a frequency of 50 Hz and an amplitude corresponding to nearly half the fundamental wavelength. Although much more sensitive cameras exist, such as the I-CCD used in [67], we again used our modest Pixelink camera to record the trace. However, notably, this time a 0.5 s integration time was used and 10 frames were averaged at each delay for an effective integration time of nearly 5 s. The trace was measured using 160 delay steps at 27 fs per step. This measurement took approximately 15 min. We compared this measurement to a high-resolution spectrometer, as this pulse was outside the measurement range of our available GRENOUILLE.

2.2.2 Results and Discussion
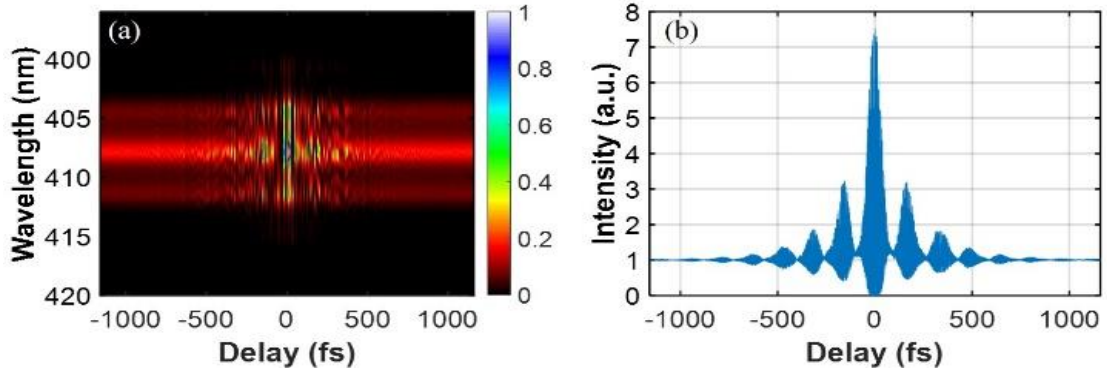
Figure 2.4 (a) Measured SHG IFROG trace and (b) normalized Interferometric Autocorrelation.

In Figure 2.4(a), we plot our measured CG trace from the first experiment. By summing over the vertical dimension of the CG trace, we can obtain the interferometric autocorrelation (IAC) which we plot, normalized relative to the background, in Figure 2.4(b). Similar to [45], we performed a 2D Fourier-filtering and subtracted a background equal to the average of 70 delays at the end of the trace to extract the standard SHG FROG trace from the CG trace. All experimental CG traces were calibrated using the characteristic peaks in the traces and a curve-fitting scheme as described in [83].

In Figure 2.5, we plot the measured and retrieved results obtained using both CG and SG from the first experiment. The measured CG (Figure 2.5(a)) and SG (Figure 2.5(c)) traces were binned to a 256×256 array. We retrieved each pulse using the newly developed and highly reliable RANA Approach for SHG FROG [84, 85]. The FROG errors for the SG and CG traces were 0.0068 and 0.0062 respectively. Figure 2.5(e) and Figure 2.5(f) attest to the excellent agreement achieved between the CG and SG retrieved results.

42
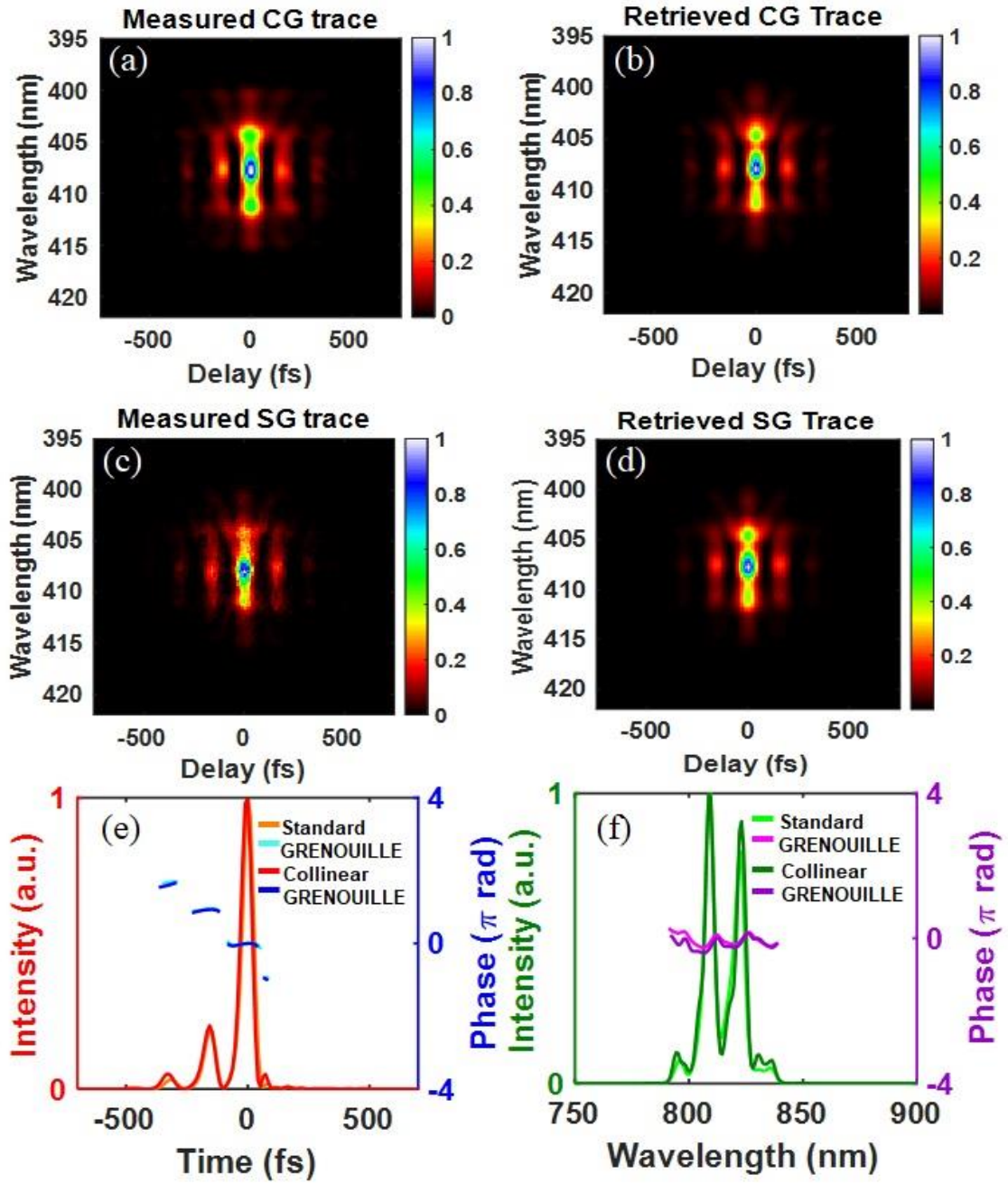
Figure 2.5 Results from the first, proof-of-principle Collinear GRENOUILLE (CG) experiment.
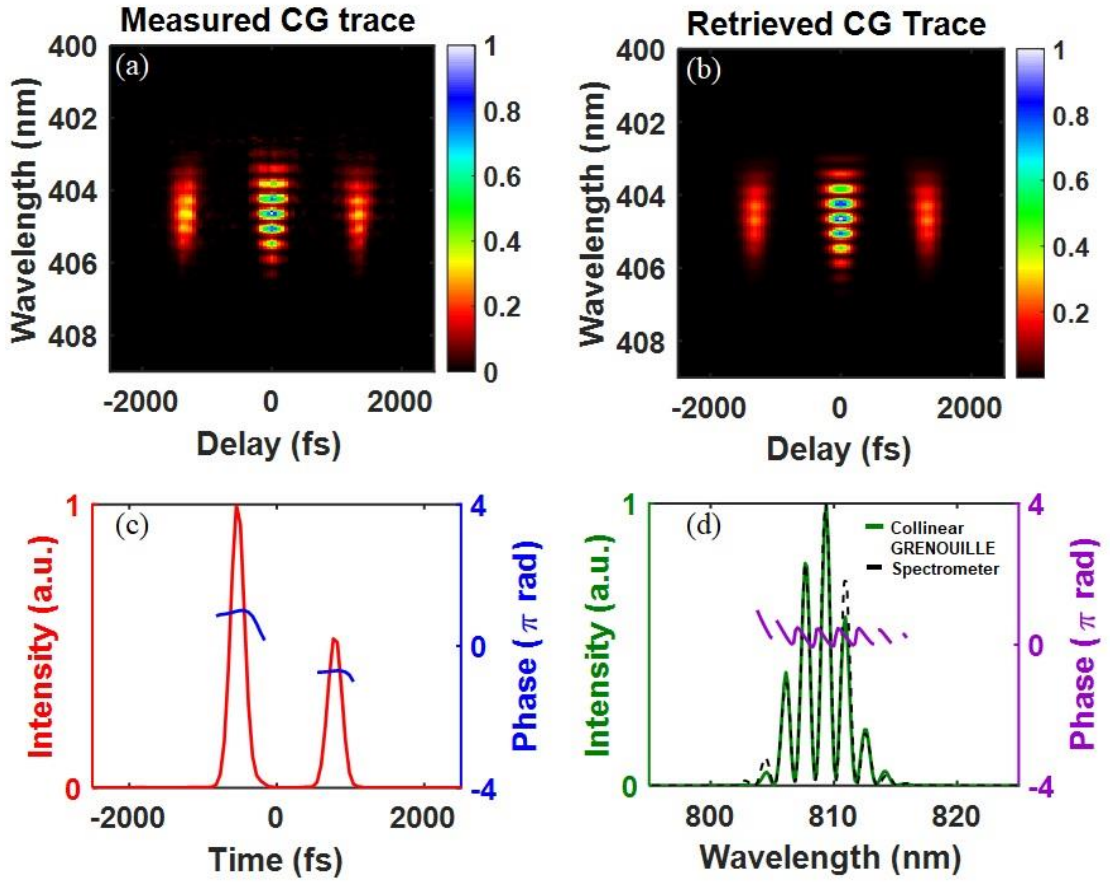
Figure 2.6 Results of the second, high-sensitivity Collinear GRENOUILLE experiment.

In Figure 2.6, we plot the results from the second, more sensitive measurement of a double pulse. After light Fourier-filtering and background subtraction, this trace was also binned to a 256×256 array. Since our focal spot size phase-matched an SH bandwidth slightly narrower than the expected SH bandwidth from our pulse, we then performed a standard frequency marginal correction to the measured trace [38]. Alternatively, a tighter focusing lens could have been used, which would yield a smaller spot size and would phase-match a broader SH bandwidth, more easily capturing the entire bandwidth of our

pulse. We again retrieved the pulse using the RANA Approach for SHG FROG. The FROG error for this CG measurement was 0.0066. Upon close inspection of the trace, residual spectral fringes can be seen in the side lobes of the trace, which should not be present after background subtraction. We believe these residual fringes are a result of either instability in the Michelson that generates the double pulse or more likely a stray reflection. Despite this, very good agreement was still achieved between CG and the high-resolution spectrometer.

2.2.3 Conclusions

To summarize, we have developed a practical, self-referenced pulse-measurement technique for weak picosecond pulses based on GRENOUILLE. To enhance GRENOUILLE's sensitivity, we traded its crossed-beam line-focus geometry and single-shot functionality for a point-focus collinear-beam geometry and a delay line. Using GRENOUILLE's thick crystal, along with a collinear beam geometry, maximizes SHG efficiency and makes Collinear GRENOUILLE substantially more sensitive than current GRENOUILLEs and FROGs. Our demonstration of the Collinear GRENOUILLE technique involved measuring two complex pulses: one consisting of a relatively high-energy train of multiple pulses produced by an etalon and a 48 fJ double pulse from a Michelson interferometer. We confirmed the results of our measurements with a standard GRENOUILLE and a high-resolution spectrometer, respectively, achieving excellent agreement in both cases. Sensitivity can be further improved using a more sensitive camera and/or by accepting a lower signal-to-noise ratio in the measured trace, the latter of which is readily handled by the FROG algorithm [38] in conjunction with the RANA approach.

These modifications should take the sensitivity to sub-fJ levels. Also, as the repetition rate of lasers increases, for example, to the nearly 100 GHz rep rates expected of next-generation telecommunication systems, even weaker and/or longer pulses should be measurable using this device.

2.3　A sensitive FROG Device for weak pulses at 1030 nm

2.3.1　Experimental Setup

For our highly sensitive SHG FROG for measuring pulses at 1030 nm we chose a PPLN crystal as it proved to be the best nonlinear crystal in terms of conversion efficiency among those compared [60]. A collinear geometry was applied with a pulse and its delayed replica propagating along the same path. The SHG is more efficient in that way, because the tightly focused beams fully overlap within the entire length of the crystal. The collinear geometry also allowed us to use the same, standard PPLN crystal with a period of 6.26 μm, optimal for SHG around 1030 nm, while we would need a custom one to achieve QPM in a non-collinear geometry. We washed out interferometric fringes between a pulse and its replica to the level of noise by dithering a mirror in one arm of the Michelson interferometer used for generation of delayed replica. The mirror was mounted on a linear translation stage with a piezo actuator that was driven by a triangular voltage signal with a frequency of 20 Hz. The amplitude of the signal was precisely chosen, such that the stage would move over exactly two interferometric fringes. Guided by our previous tests on conversion efficiency, we tightly focused the beam into a crystal to a focal spot of about 5 μm. The focal spot served as an entrance slit of a spectrometer, which was built right after the crystal. In addition to high SHG conversion efficiency, this is an important contribution to increased

46

sensitivity of this FROG system as no signal light is lost due to coupling in a spectrometer. Spherical mirrors with 250-mm and 500-mm focal lengths were used for re-collimation and focusing, and a 25-mm-wide reflective diffraction grating with a ruling of 1800 lines/mm was used for dispersing a SH light. They were placed in an asymmetric Czerny-Turner geometry with angles optimized for minimal aberrations. The SH light was detected by a standard monochromatic CMOS industrial camera. The spectrometer was calibrated with a double pulse with a known delay between the pulses. A spectral fringe depth above 60 % was achieved for the delay of 27 ps giving a rough approximation of spectral resolution of 33 pm.

2.3.2   Experimental Results
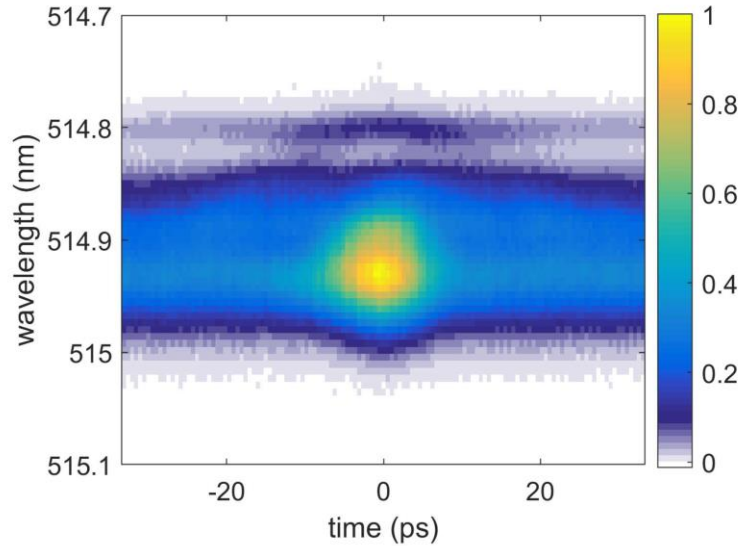
Figure 2.7 Measured SHG FROG trace of a 20 fJ at 1030 pulse before trace processing. Figure taken from [60].

47
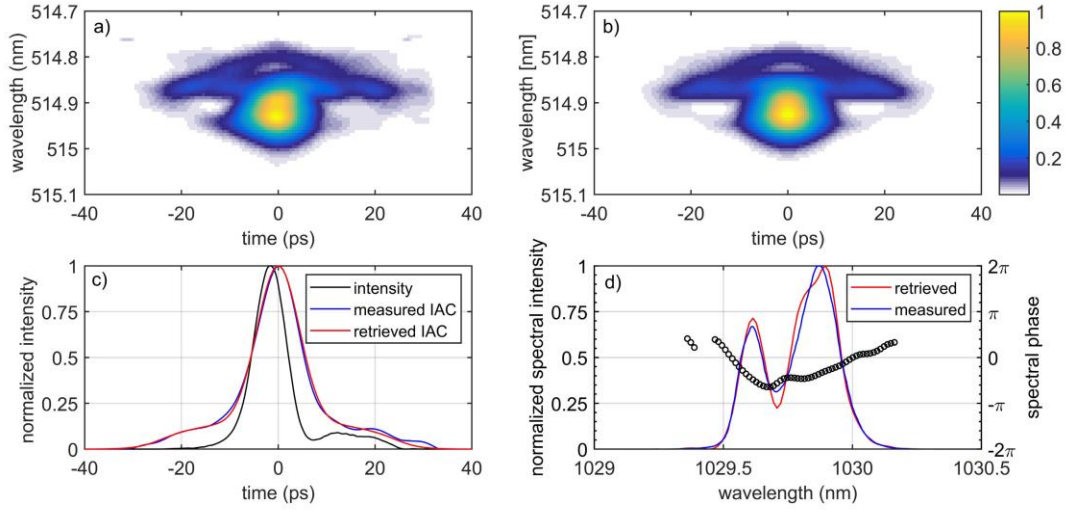
Figure 2.8 SHG FROG measurement of an internally-built mode-locked fiber oscillator. Figure taken from [60].

2.3.3 Discussion

We performed an SHG FROG measurement of an in-house built SESAM-mode locked fiber oscillator with a central wavelength of 1029.8 nm and a repetition rate of 37 MHz. The FROG trace shown in Figure 2.7 was recorded with an average power of 750 nW, corresponding to a pulse energy of 20 fJ. With an integration time of the camera set to 1 s, the measurement took about 3 minutes. The delay marginal of the measured FROG trace had a ratio of background vs. peak of 1:2.96, very close to the expected 1:3 (for an intensity autocorrelation with background to which it corresponds). We also evaluated the presence of background noise from the edges of the trace to be 1/568 of the peak value at zero delay. To prepare the trace for retrieval, we subtracted the background which was calculated as an average over the first and the last five delay points. After that, a mild high frequency noise Fourier filtering was performed to yield a trace shown in Figure 2.8(a).

For the retrieval we used the RANA algorithm [7]. A low G error of 0.0084 and a good agreement between the retrieved and measured spectrum of the pulse (see Figure 2.8(d)) confirm the successful retrieval of a 7.6-ps-long pulse with an accompanying, weak satellite pulse(s). A sensitivity of the SHG FROG setup given in terms of product of average and peak power of the weakest detectable pulse can be therefore estimated to 2×10^{-3} $(\text{mW})^2$.

CHAPTER 3.

This Chapter originally appeared as a paper by the author:

Travis Jones, William K. Peters, Anatoly Efimov, Richard L. Sandberg, Dmitry Yarotski, Rick Trebino, and Pamela Bowlan, "Encoding the complete electric field of an ultraviolet ultrashort laser pulse in a near-infrared nonlinear-optical signal," Opt. Express **28**, 26850-26860 (2020) [86]

3.1 Motivation

Ultrashort laser pulses in the UV spectral range provide access to higher-energy electronic transitions and achieve a tighter focus than visible or near-infrared (NIR) pulses and so play important roles in time-resolved spectroscopy [87-90], nanolithography [91] and micromachining [92, 93]. Of course, any application of UV ultrashort pulses requires measuring their complete electric field for optimizing and confirming the characteristics of the light source. UV pulse measurement can also serve as a phase and amplitude sensitive detector for measuring the complex response of a sample, as in multidimensional spectroscopies [94, 95].

One of the main challenges in measuring UV pulses is detection, since wavelengths below about 200 nm are outside of the range of standard silicon detectors and so require more expensive, specialized UV cameras. It can also be challenging to find a nonlinear medium that is transparent in the UV and has the required nonlinear-optical phase-matching characteristics. Deeper in the UV, optical components such as lenses and mirrors also become less available. FROG has been applied to measure 400 nm femtosecond pulses

by difference frequency generation with an 800 nm pulse, which conveniently produces a nonlinear signal in the NIR [53]. However, finding an appropriate medium that is transparent and has the birefringence required for phase matching at wavelengths shorter than 400 nm in a second-order nonlinear optical process is challenging.

Therefore, measurement of UV pulses most commonly uses third-order nonlinear optical signals such as PG [96, 97], SD [98-102], and TG [52, 103-106], which can often be accomplished in any transparent medium. Still, most of these methods require detecting a nonlinear signal at the UV pulse wavelength. FROG spectrograms can be measured for deeper UV pulses which are absorbed by or ionize the nonlinear medium using methods based on spectrally resolved photoemission [48, 107], or reflection by plasma mirrors produced by intense NIR pulses [108].

In this Chapter, a variation of TG XFROG is demonstrated in which the transient grating is induced by two copies of the unknown UV pulse. This grating is then probed by a known NIR reference pulse, yielding a signal pulse at the same wavelength as the probe pulse, which can then be easily detected. Importantly, this technique involves scanning the delay *between the UV pulses*, rather than the reference-pulse delay as in standard TG FROG [52, 56, 104]. This allows the retrieval of the UV-pulse phase information, which would otherwise not be available. This variation on TG XFROG is referred to as Induced-Grating XFROG (IG XFROG). Proof-of-principle measurements of pulses centered at 400 nm with an 800 nm reference pulse are presented. The measurements presented show that IG XFROG spectrograms contain the 400 nm pulse phase information. A novel generalized

projections algorithm is also discussed and used to reconstruct the 400 nm pulse's intensity and phase.

3.2   Using NIR nonlinear-optical signals to measure UV pulses

The IG XFROG technique is based on standard TG FROG [52, 104]. Compared to the other 3rd-order FROG geometries, TG FROG has several advantages for UV pulse measurement: it uses a nonlinear process that can be phase-matched by satisfying the Bragg condition, $\sin(\theta_{probe}) = (\lambda_{probe} / \lambda_{excite}) \sin(\theta_{excite})$; its signal is spatially separated from the input beams and so is background-free; and polarizers, which introduce dispersion, are not needed.

In a typical TG FROG measurement, the pulse to be characterized is split into three parallel beams that cross and spatially overlap at the focus of a lens at the nonlinear medium [52, 104]. Two of the beams temporally overlap and interfere, inducing the transient grating, while the third beam diffracts from it forming the nonlinear signal. A TG FROG trace is the spectrum of the diffracted pulse versus the delay between the diffracted pulse and the transient grating. In TG cross-correlation FROG, or TG XFROG, a characterized reference pulse is available, and it induces the grating and the diffracted unknown pulse forms the nonlinear signal [100, 101]. In standard TG XFROG, the spectrogram contains phase information only of the pulse that *diffracts* from the grating, and not of the pulses that *induce* it. As a result, when measuring a UV pulse, the UV pulse must probe the grating, not induce it, and the nonlinear signal will necessarily be at the same UV wavelength, thus requiring UV detection.

IG XFROG uses a similar $\chi^{(3)}$ process, but instead produces a nonlinear signal at the reference pulse wavelength, in the visible or NIR, avoiding the need for UV light detection. Instead of diffracting the unknown pulse from the transient grating, two copies of the unknown UV pulse induce the transient grating, as shown in Figure 3.1. Then the longer-wavelength reference pulse diffracts from the grating to form an easily detectable nonlinear signal centered at the reference pulse wavelength. The key to measuring a spectrogram that contains the UV pulse's phase information is to vary the delay between the UV pulse replicas, maintaining the reference probe pulse at zero delay. Intuitively, one can consider that the UV pulse-pair only induce a grating when they temporally overlap, so the contrast or grating fringe depth is best at zero delay and the instantaneous wavelength of the UV pulse determines the periodicity of the grating. Thus, the transient grating contrast and phase versus delay between the UV pulses contains both the intensity and phase information about the UV pulse, which is probed and read-out by the longer-wavelength, diffracted reference pulse. More precisely, each UV pulse generates a coherence in the nonlinear-optical medium that lives for the dephasing time, usually referred to as T_2. But this time is generally very short for condensed phases and in this work we consider the coherent response to be instantaneous and representable by a delta function.

53

Figure 3.1 Schematic of the beam geometry used in IG XFROG. Bragg condition: sin $\theta_{ref} = (\lambda_{ref} / \lambda_{unk})$ sin θ_{unk}, where E_{ref} is the probe pulse and E_{unk} is the excite pulse. θ_{ref} and θ_{unk} represent the half-crossing angles for the reference and unknown pulses.

3.3 Generalized-projections phase-retrieval algorithm for IG XFROG

The IG XFROG technique discussed above results in the following nonlinear signal:

$$E_{sig}(t, \tau) = E_{ref}(t)E_{unk}^*(t)E_{unk}(t - \tau)$$

(3.1)

The reference, unknown, and signal fields are E_{ref}, E_{unk}, and E_{sig}, respectively, with the

delay, τ in one of the unknown fields. Measuring the spectrum of this nonlinear signal

versus τ results in a FROG trace, $I_{sig}(\omega, \tau)$, given by,

$$I_{sig}(\omega, \tau) = \left| \int_{-\infty}^{\infty} E_{ref}(t)E_{unk}^*(t)E_{unk}(t - \tau) \exp(-i\omega t)\, dt \right|^2$$

(3.2)

Using Equations 3.1–3.2, the generalized-projections phase-retrieval algorithm can be

applied to extract $E_{unk}(t)$ from the FROG trace [38]. Following the usual procedure, the

first step is to make an initial guess for $E_{unk}(t)$, which is usually taken to be random noise.

54

This guess and the known reference field $E_{ref}(t)$ are then used to calculate $E_{sig}(t, \tau)$ from Equation 3.1. Next, $E_{sig}(t, \tau)$ is Fourier transformed to the frequency domain and its magnitude is replaced by the square root of the measured trace yielding $\tilde{E}'_{sig}(\omega, \tau)$. $\tilde{E}'_{sig}(\omega, \tau)$ is then inverse Fourier transformed to the (t, τ) domain where it is used to update the next guess for the unknown pulse. In order to obtain $E_{unk}(t)$ for the next iteration, we minimize the following functional distance:

$$Z^{(k)} = \sum_{i,j=1}^{N} \left| E_{sig}^{(k)}(t_i, \tau_j) - E_{ref}(t_i) E_{unk}^{*(k+1)}(t_i) E_{unk}^{(k+1)}(t_i, \tau_j) \right|^2 \tag{3.3}$$

where superscripts k and $k + 1$ denote the current and next iteration respectively. Equation 3.3 takes into account the functional form of the nonlinear signal field, $E_{sig}(t, \tau)$, for the Induced Grating XFROG trace, and is otherwise known as the mathematical form constraint. Again, following the approached discussed in [38], to find an updated guess for the unknown field, Equation 3.3 is minimized with respect to the unknown field via the method of steepest descent in which the equation for updating the field is given by Equation 3.4 where $x^{(k)}$ is a scalar multiplier. The expressions for derivatives are given by Equation 3.5 and Equation 3.6 where the k and $k + 1$ superscripts have been suppressed for simplicity,

$$E_{unk}^{(k+1)} = E_{unk}^{(k)} - x^{(k)} \nabla Z^{(k)} \tag{3.4}$$

$$\frac{\partial Z}{\partial Re\{E_{unk}(t_k)\}} \sum_{j=1}^{N} \begin{bmatrix} -E_{sig}(t_k, \tau_j)E_{ref}^*(t_k)E_{unk}^*(t_k - \tau_j) \\ +E_{unk}(t_k)\left|E_{ref}(t_k)E_{unk}(t_k - \tau_j)\right|^2 \\ -E_{sig}(t_k + \tau_j, \tau_j)E_{ref}^*(t_k + \tau_j)E_{unk}(t_k + \tau_j) \\ +E_{unk}(t_k)\left|E_{ref}(t_k + \tau_j)E_{unk}(t_k + \tau_j)\right|^2 \\ +c.c \end{bmatrix} \quad (3.5)$$

$$\frac{\partial Z}{\partial Im\{E_{unk}(t_k)\}} \sum_{j=1}^{N} \begin{bmatrix} -iE_{sig}(t_k, \tau_j)E_{ref}^*(t_k)E_{unk}^*(t_k - \tau_j) \\ -iE_{unk}(t_k)\left|E_{ref}(t_k)E_{unk}(t_k - \tau_j)\right|^2 \\ +iE_{sig}(t_k + \tau_j, \tau_j)E_{ref}^*(t_k + \tau_j)E_{unk}(t_k + \tau_j) \\ -iE_{unk}(t_k)\left|E_{ref}(t_k + \tau_j)E_{unk}(t_k + \tau_j)\right|^2 \\ +c.c \end{bmatrix} \quad (3.6)$$

Note, that in writing these equations, it is necessary to know which of the two unknown pulses is delayed, due to the complex conjugate in Equation 3.1. Placing the delay in the other copy of the unknown pulse slightly changes the equations above.

3.4 Experimental setup

Figure 3.2 shows a schematic of the experimental setup used for proof-of-principle demonstrations of the IG XFROG method discussed above. For the light source, we used a regenerative Ti:Sapphire amplifier with pulses centered near 800 nm at a 1 KHz repetition rate. The laser beam was first split (BS1 in Figure 3.2) into two replicas. A less intense replica (~10%) of the pulse energy was used for the reference pulse, which was characterized with a commercial GRENOUILLE device [50] by introducing a flip mirror (FM). The reference pulse used in the measurements provided in the next Section was approximately 160 fs long with a small amount of predominantly quadratic spectral phase (chirp). The temporal intensity and phase of this pulse is shown in the inset in Figure 3.2.
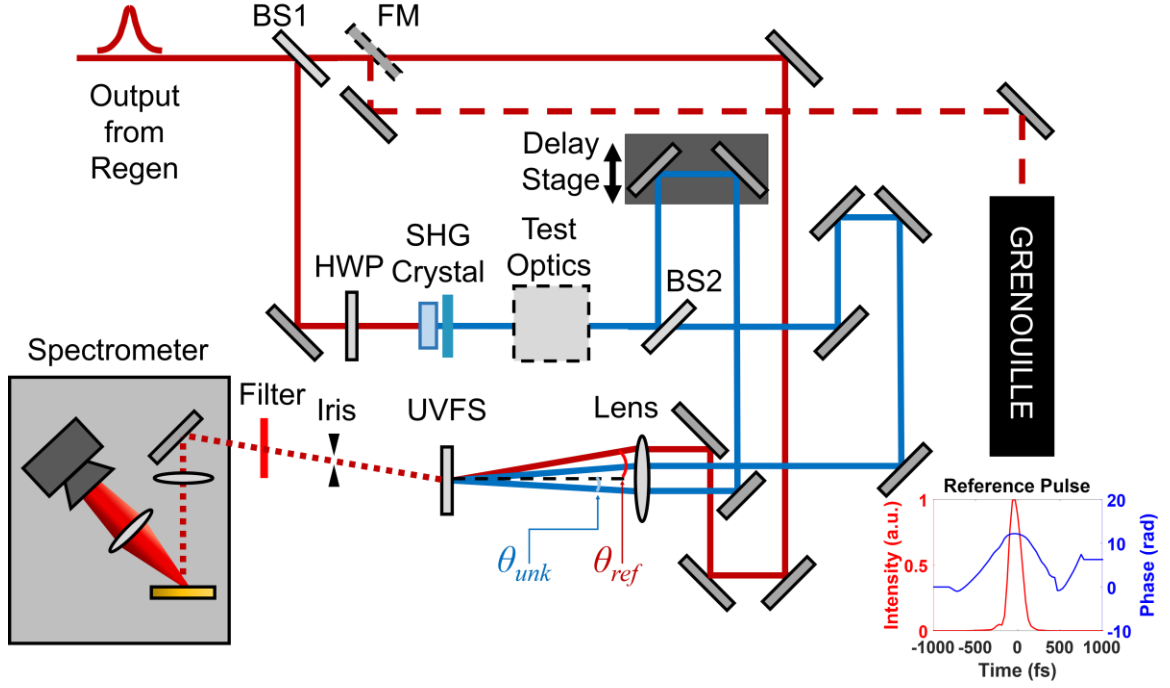
Figure 3.2 Experimental setup for IG XFROG.

To generate the unknown UV pulses, the more intense replica of the beam (~90%) was converted to 400 nm in a 0.5 mm-thick BBO SHG crystal. A half-wave plate (HWP) is used before the second harmonic generation (SHG) crystal so that the resulting 400 nm pulses have the same polarization as the reference pulse. To produce the transient grating, a 50/50 beam splitter (BS2) was used to generate two replicas of the 400 nm pulse. All three beams propagated parallel and along a horizontal line to a 250 mm focal length lens, so that they spatially overlapped and focused at the sample. The spot size of the 400 nm beams at the focus was approximately 40 μm FWHM. Phase matching in these experiments simply requires satisfying the Bragg condition for the input beams, or that $\sin(\theta_{ref}) = (\lambda_{ref}/\lambda_{unk})\sin(\theta_{unk})$. To satisfy this, we used half-crossing-angles of approximately 1.72° and 3.43° for the unknown (excite) and reference (probe) beams,

respectively. The nonlinear medium was UV fused silica. The 800 nm nonlinear signal was detected with a homemade imaging spectrometer. To collect the FROG traces, a motorized delay stage was used to vary the delay of one 400 nm pulse, and the spectrum of the diffracted NIR reference pulse was measured as a function of delay.

3.5 Results

Two sets of measurements were performed to test the performance of IG XFROG. In the first one, the 400 nm pulse was intentionally chirped by a known amount using 0 mm, 20 mm, and 50 mm pieces of SF11 glass (the "test optic" in Figure 3.2). The top row in Figure 3.3 shows the results of these measurements. To extract $E_{unk}(t)$ from the measured traces, we applied the GP algorithm discussed in Section 3.3.
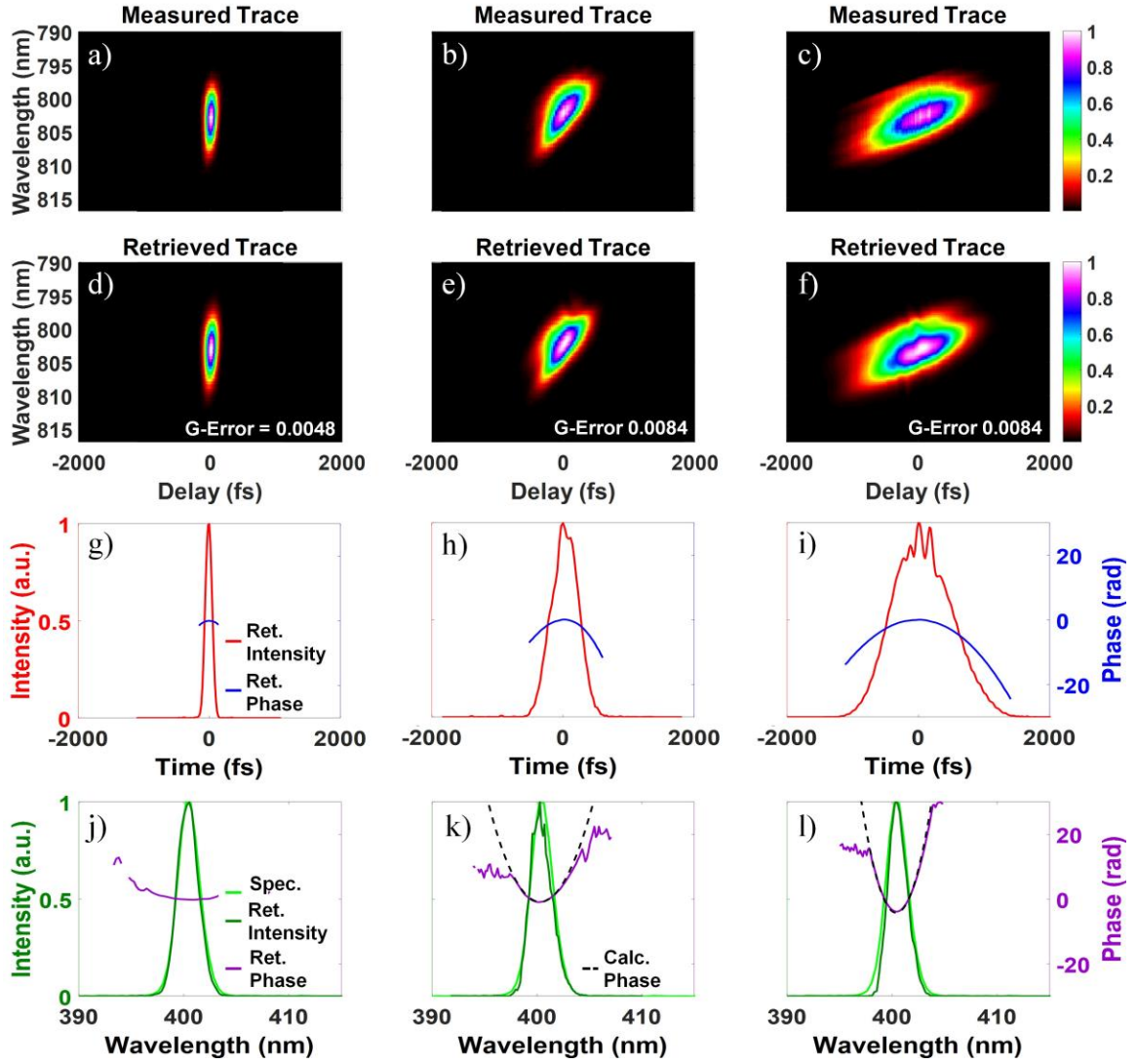
Figure 3.3 Measurements of chirped 400 nm pulses using an 800 nm reference pulse.

The accuracy of the reconstruction is typically quantified by the *G* error. As usual, the *G* error on each iteration is defined as [38]:

$$G^{(k)} = \sqrt{\frac{1}{N^2} \sum_{i,j=1}^{N} \left| I_{FROG}(\omega_i, \tau_j) - \mu I_{FROG}^{(k)}(\omega_i, \tau_j) \right|^2} \qquad (3.7)$$

where the index k indicates the kth iteration and μ is a real normalization constant used to minimize $G^{(k)}$. And G (without a superscript) is the resulting rms error when the algorithm is finished running. G errors of about 1% or less indicate convergence and a good measurement for the types of pulses and traces considered here.

The reconstructed traces along with their G errors (rms differences between the measured and retrieved traces) are provided in Figure 3.3(d)–Figure 3.3(f). The reconstructed pulse shapes in the time and frequency domains are shown in Figure 3.3(g)–Figure 3.3(i) and Figure 3.3(j)– Figure 3.3(l) respectively. Independently measured spectra (light green) are overlaid for comparison, as well as the calculated spectral phases (black, dashed lines).

As a second test of this method, double pulses, produced by a Michelson interferometer (the "test optic" in Figure 3.2), were measured. These measurements are shown in Figure 3.4 for three different double pulse separations, again showing the measured traces, the reconstructed traces from the GP algorithm, G errors, and the reconstructed pulses in the time and frequency domains.
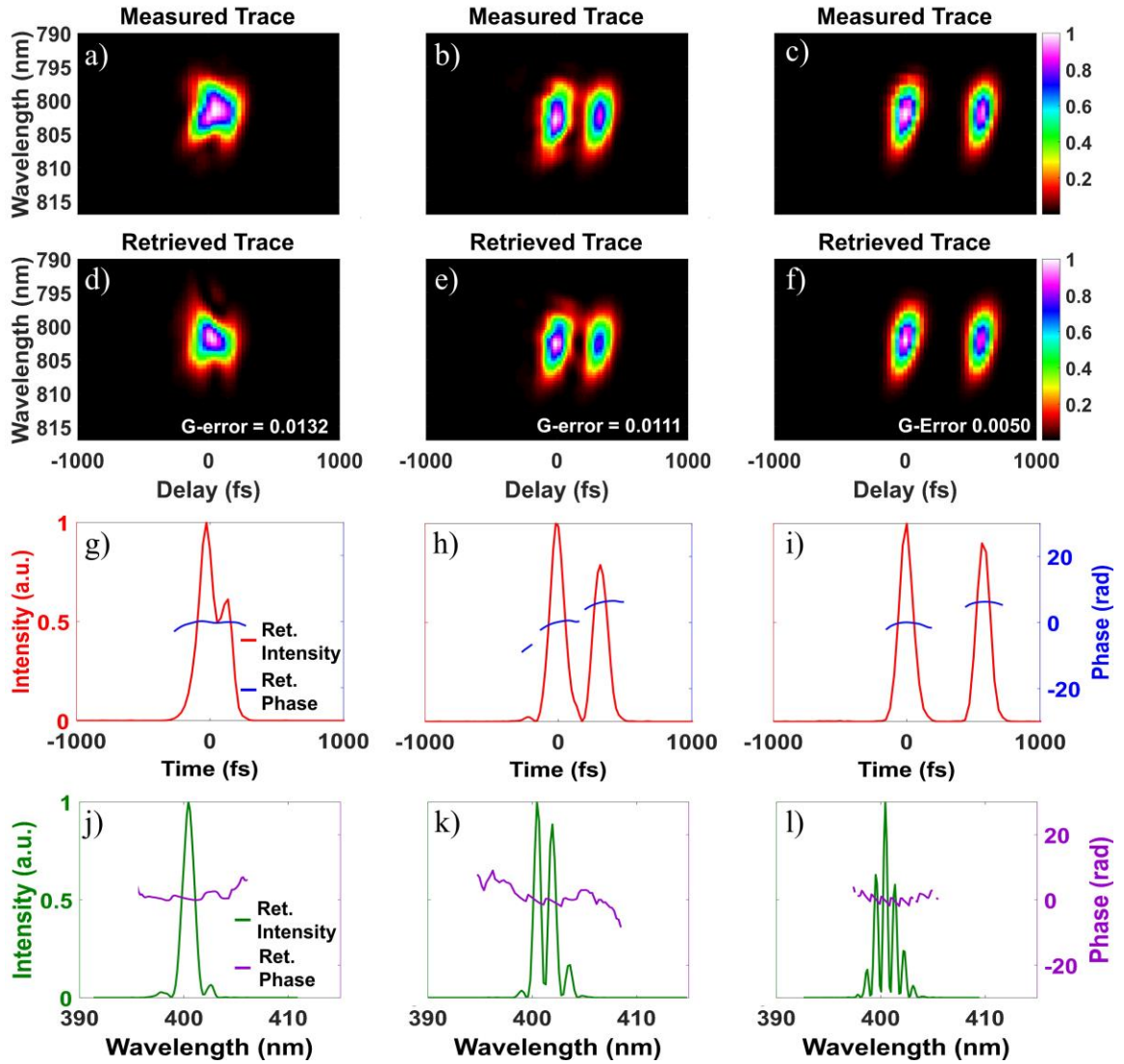
Figure 3.4 Experimental results from the series of variable-separation double pulse measurements. Columns correspond to near-zero separation (left), ~300 fs separation (center), and ~600 fs (right).

3.6   Discussion

The measurements in Figure 3.3 demonstrate that IG XFROG spectrograms contain the 400 nm pulse phase and amplitude information. A convenient feature of these spectrograms, similar to other types of FROG based on third-order nonlinear optical effects [38], is that the pulse shape can often be intuitively read directly from the FROG trace. Figure 3.3 shows that chirp in the 400 nm pulse results in a tilted FROG trace where the amount of tilt depends on the amount of chirp. Similarly, the FROG traces for the double pulses in Figure 3.4 have an intensity profile vs. delay that follows that of the double pulses' temporal intensity. As is the case with other third-order FROG variations, these traces also indicate the absence of a direction-of-time ambiguity. Note that the appearance of the traces depends on the pulse duration of the NIR reference pulse relative to the 400 nm pulses. Figure 3.4 is an example of this. Here, the NIR and 400 nm pulses (before the "test optic") have similar pulse durations. Thus, as we varied the double pulse separation, the reference pulse was only long enough in time to maintain sufficient temporal overlap with one of the pulses in the double pulse. If the reference pulse were instead long enough to maintain temporal overlap with both pulses in the double pulse, then the Induced Grating XFROG trace would look more similar to a typical self-referenced double-pulse FROG trace [38], with a three-lobed structure (see Appendix A).

Prior to their retrieval, each of the measured traces in Figure 3.3 and Figure 3.4 were binned to 128×128 arrays except for the trace in Figure 3.3(c) which was binned to a 256×256 array. The second row of Figure 3.3–Figure 3.4 shows the results of the GP phase retrieval algorithm. The *G* error for each retrieval is provided at the bottom right of each

62

retrieved trace. Convergence was typically achieved within a few minutes. In the second set of measurements, we suspect that instabilities in the Michelson interferometer used to generate the double pulse may be responsible for a higher G error, particularly in the trace with the smallest double pulse separation. Still, these measurements demonstrate that this method works for measuring more complex pulse shapes with larger time-bandwidth products.

The chirped pulses allow for another test of the measurements and reconstruction. Figure 3.3(j)–Figure 3.3(l) show the retrieved spectra compared with independently measured spectra using an Ocean Optics spectrometer. The spectra are in good agreement. Furthermore, since the shape of the spectral phase in the 400 nm pulses in Fig. 3 comes primarily from the dispersive glass that we introduced, we can also compare the retrieved spectral phases with that calculated from the Sellmeier equations for SF11 [109]. The expected GDD from the 20 mm and 50 mm pieces of SF11 was calculated to be 17721.3 fs^2 and 44257.0 fs^2, respectively. These values correspond to second-order spectral phase coefficients of 8860.7 fs2 and 22128.5 fs^2. Curves corresponding to these values are shown as black dashed lines in Figure 3.3(j)–Figure 3.3(l) and are in good agreement with the measured spectral phases. Together these checks on the spectra and spectral phase prove that the correct spectral (or equivalently temporal) electric fields were retrieved.

Measurements like those of the approximately 125 fs pulse in the first column of Figure 3.3 were obtained with a total 400 nm pulse energy of approximately 140 nJ and a 20 ms integration time on the camera. Combined with the 40 µm spot size mentioned above, this results in a fluence of ~10 mJ/cm^2 at the sample. In addition to the integration

63

time on the camera, the required amount of UV pulse fluence also depends on the reference pulse energy. Thus, by reducing the UV pulse energy and compensating this reduction with an increase in the reference pulse energy and/or camera integration time, UV pulses with considerably less pulse energy should be measurable. In this case, one should also take care not to increase the reference pulse energy too much as this could lead to increased scattered light at the signal wavelength. Furthermore, since the input polarization used is not restricted by the nonlinear interaction involved, this technique should also be applicable in instances where the measured pulse varies differently along different polarization components.

Previous work using TG XFROG has shown that the phase-matching bandwidth of a transient grating process can be very broadband [105]. The phase-matching bandwidth in these experiments is estimated to be greater than 100 nm. This could be increased, if necessary, by choosing different focusing conditions. However, even if the phase-matching bandwidth becomes limiting, for example if measuring single-cycle UV pulses, FROG spectrograms can be corrected for insufficient phase-matching bandwidth [110]. Thus there is no known strict lower limit on the duration of the unknown pulse that can be measured with IG XFROG. However, when attempting to measure extremely short pulses other challenges arise. These are the detection of the very broadband nonlinear signal, accounting for material dispersion in the nonlinear medium and other optical components [111], geometrical smearing (for multi-shot measurements), and the breakdown of the slowly-varying envelope approximation, all of which are typically solvable problems [38].

Additionally, there are no known strict requirements on the duration or complexity of the reference pulse required for Induced-Grating XFROG, provided that its intensity and phase are well characterized. Shorter or longer references pulses can in principle be used. However, to avoid unnecessarily complicating the measurement, choosing the simplest available reference pulse at the desired center wavelength is recommended (typically the NIR pulse directly out of the laser system makes a good reference pulse). Also, as in standard XFROG, for simultaneously achieving good spectral and temporal resolutions it is best to aim for equally distributing information in the measured trace between both domains of the trace (time and frequency) [38].

3.7 Conclusions

In this Chapter we introduced the IG XFROG technique for encoding the intensity and phase of a 400 nm pulse in a NIR nonlinear-optical signal. We applied a modified GP phase retrieval algorithm to reconstruct the pulse's electric field from the measured spectrogram. To test this method, we demonstrated accurate measurement of chirped 400 nm pulses and also the measurement of more complex double pulses. While the proof-of-principle tests done here were at 400 nm, this approach should be extendable deeper into the UV and potentially even into the extreme UV [112] or x-ray range, since phase matching only requires satisfying the Bragg condition. As we will see in the next Chapter, another advantage of detecting the nonlinear signal at the reference pulse wavelength is that the medium does not necessarily have to be transparent at the unknown pulse wavelength as long as the functional form of nonlinear signal is still known. Single-shot implementation of IG XFROG should also be straightforward following the approach used

for other single-shot FROG implementations [38] (see for example [105]). In conclusion, IG XFROG represents a first step towards developing an all-optical FROG method for measuring UV and possibly even higher-photon-energy femtosecond laser pulses.

CHAPTER 4.

4.1 Introduction

The recent development of bright, coherent sources of UV to EUV femtosecond pulses from optical parametric amplifiers, harmonic generation [113], or Free Electron Lasers [114, 115] allows for completely new types of time resolved spectroscopy at higher energy transitions (e.g. [116-118]), and for pushing any technique to higher spatial and temporal resolutions (e.g. [116, 119]). To successfully use any light source, whether it's to optimize the light source, or for data collection and interpretation, it's necessary to characterize it, or to unambiguously measure the amplitude and phase of the pulses.

Because ultrashort laser pulses are too fast to time-resolve with electronics, they are typically measured using a nonlinear optical interaction as the fast "time-gate" or shutter, since the light-matter interaction can be as fast as attoseconds. This concept is employed in the widely used method of characterizing ultrashort pulses, Frequency-Resolved Optical Gating (FROG) [38]. The FROG technique is quite flexible and has been applied in a wide frequency range, from the infrared to the UV, since almost any instantaneous (and some non-instantaneous [120]) nonlinear optical effects can be used as the time-gate [38]. Still, extension deeper into the UV beyond 300 nm comes with a major obstacle: in the deep UV the light-matter interaction in almost any material is dominated by absorption from photoexcitation of electrons across the bandgap or photoionization, a process that lasts for picoseconds to nanoseconds [121], significantly longer than the pulse itself. As a result,

most applications of FROG in the deep and extreme UV have relied on the detection of photoelectrons (e.g. [48, 122]) rather than having an optical-readout.

In this Chapter, we will see that an instantaneous medium is not required and that absorption can be used as the nonlinear optical time-gate. To do this we use the novel version of FROG discussed in the previous Chapter entitled IG XFROG [86]. In the previous Chapter, IG XFROG was introduced as a convenient method for encoding a UV pulse shape into an easily detectable NIR nonlinear optical signal, avoiding the need for specialized and expensive UV detectors. In that case, the nonlinear medium was optically transparent at the unknown pulse wavelength and had an instantaneous response.

In this Chapter, we will see that IG XFROG can also be done in an absorbing medium. The key advance, is that varying the delay between the UV pulse-pair making the grating, time-gates the nonlinear signal with the faster part of the material response, the creation of the electron-hole pairs, and separates out the very slow (picoseconds or longer) recovery of the excited state. This results in what is approximately a cross correlation of the reference and unknown UV pulses, similar to that achieved in a non-absorbing medium. The nonlinear signal still contains both an instantaneous phase-containing contribution and a non-instantaneous, non-phase-containing contribution, but these are distinguishable and can be accounted for in the phase retrieval. This is demonstrated by measuring 400 nm and 266 nm pulses in the medium ZnS. Because of the generic nature of absorption, and that all absorptive process contain an initial, coherent contribution, this technique should be extendable into the vacuum UV, EUV, and even the x-ray range.

4.2 Experimental setup

To demonstrate that femtosecond pulses using can be measured in an absorbing medium using IG XFROG, the experiment shown in Figure 4.1 was constructed. The light source was a regenerative Ti:Sapphire amplifier at a 1 KHz repetition rate and a center wavelength of 800 nm. A beam splitter (BS1) formed a NIR reference field, E_{ref} and the UV unknown field, E_{uv}. The unknown UV pulses were centered at 400 nm or 267 nm and generated by second or third harmonic generation of the 800 nm pulses in BBO crystals. BS2 formed a pair of beams from E_{uv} for generating the transient grating. All three beams were directed to a 250 mm focal length lens which focused and spatially overlapped the beams at the sample, a 1.5 mm thick ZnS crystal. The FROG trace was measured as the spectrum of the nonlinear signal versus the delay between the pair of UV pulses, or τ_{uv}. For comparison, or to find 0-delay, the reference pulse delay, τ_{ref} was also scanned. Phase matching was achieved by satisfying the Bragg condition: $\sin\theta_{ref} = (\lambda_{ref} / \lambda_{uv}) \sin\theta_{uv}$. Crossing angles θ_{uv} and θ_{ref} were approximately 1.72° and 3.43° for 400 nm and at 0.747° and 2.24° when measuring the 267 nm pulse.

To make interpretation of the measured FROG traces more intuitive, spectrally narrowing the reference pulse using a 3 nm bandpass filter (BPF) was found to be helpful. This made the reference pulse distinctly narrower than the bandwidth of the nonlinear signal. As with any version of XFROG [38, 86], the reference pulse should be known and $E_{ref}(t)$ is used as an input into the phase retrieval algorithm. The reference pulse was obtained using a reference scan in an instantaneous medium and confirmed using a GRENOUILLE device. The resulting pulse was approximately 432 fs long. As noted later,

these measurements also indicated that the reference pulse had a weak post pulse that was

~850 fs after the main pulses. This weak post pulse was accounted for in $E_{ref}(t)$ by adding

a second delayed, weaker replica of the main pulse, which made our results more accurate.
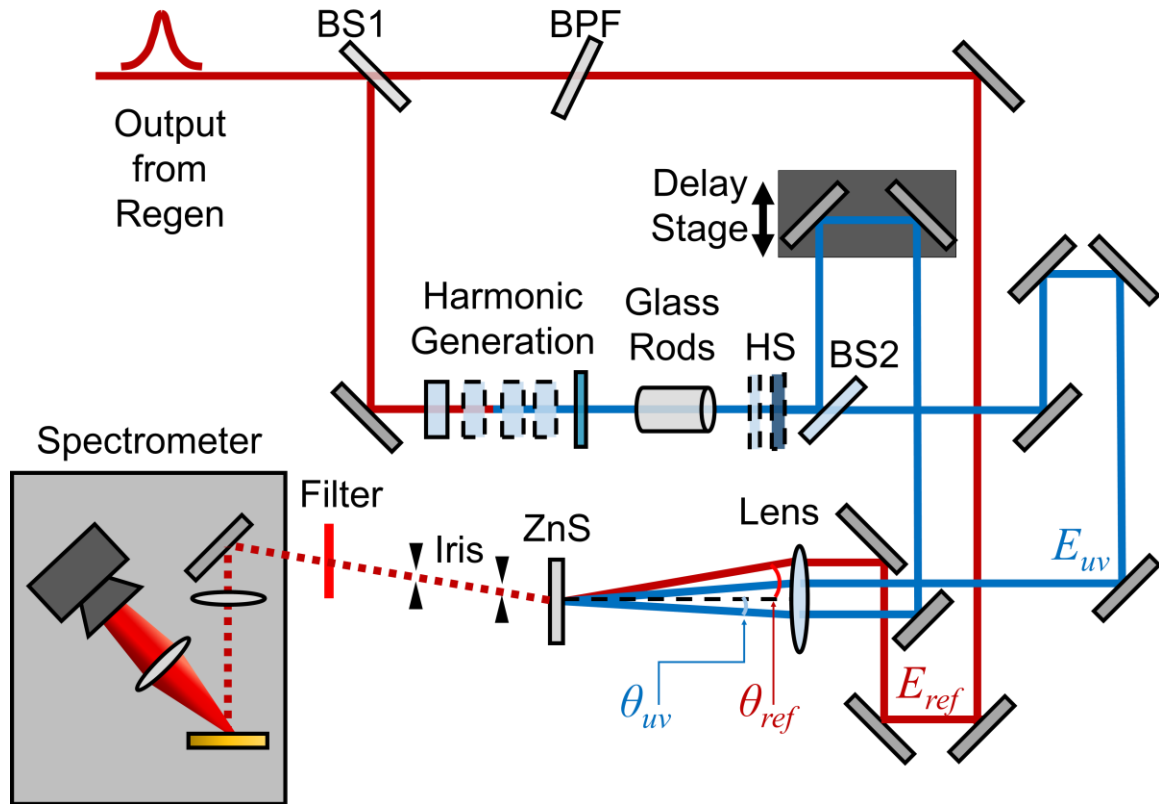
Figure 4.1 Experimental setup for Induced-Grating XFROG using a slow medium.

4.3 Results

4.3.1 *Isolating the instantaneous contribution to the nonlinear signal*

Figure 4.2(a) shows a schematic of the beam geometry used in IG XFROG to measure

UV pules where two copies of the unknown UV pulse (shown in blue) overlap in space

and time such that they induce an interference pattern which modulates the optical

properties of the medium, producing a transient grating. There are two major differences here compared to typical transient grating experiments [38, 105, 123]. One is that the unknown pulse generates the grating rather than the reference pulse. This has the major advantage of producing an NIR nonlinear signal, as we pointed out in past work [86]. The second difference is that we scan the delay between the two interfering pulses, τ_{uv}, rather than the delay of the reference pulse, τ_{ref}. As was shown in the previous chapter [86], varying τ_{uv} preserves the phase information of the UV pulses, while the nonlinear signal versus τ_{ref} would only contain the UV pulse intensity.

Another major advantage of scanning τ_{uv} in an absorptive medium is illustrated in Figure 4.2(b). Here we used ZnS as the nonlinear medium which has a bandgap of ~3.5 eV, but becomes absorptive at around 400 nm [5]. Figure 4.2(b) and Figure 4.2(c) show the spectrally resolved nonlinear signals versus the two different delays. Figure 4.2(b), shows two distinct features: a spectrally broader component near zero delay, and a narrower-band long-lived component. The spectrally broader component is indicative of the coherent FWM process that occurs when all three pulses temporally overlap in the nonlinear medium or the initial part of photoexcitation of the electrons when they are still coherent with the light (the relevant timescale being the dephasing time [37]). The longer-lived component, which persists after the pulses no longer temporally overlap is the time-scale for relaxation of the photoexcited electrons back to their ground state (i.e., the lifetime).

In contrast, a trace versus τ_{uv} in ZnS is shown in Figure 4.2(c), which does not show the long-lived response seen in Figure 4.2(b). This is because the induced grating, and hence the nonlinear signal, only exist while the UV pulse pair temporally overlap. Thus,

the duration of the nonlinear signal is approximately reduced to the length of a cross-correlation and the new frequencies generated during the coherent FWM process are still present. This can be seen by comparison to Figure 4.2(d), which shows the same measurement made in an instantaneous medium, fused silica [86]. Still, some dephasing happens within the UV pulse duration and Figure 4.2(c) contains both a phase-containing contribution that looks like that in Figure 4.2(d) and non-phase containing contribution, the round, central portion not seen in the fused silica measurement.
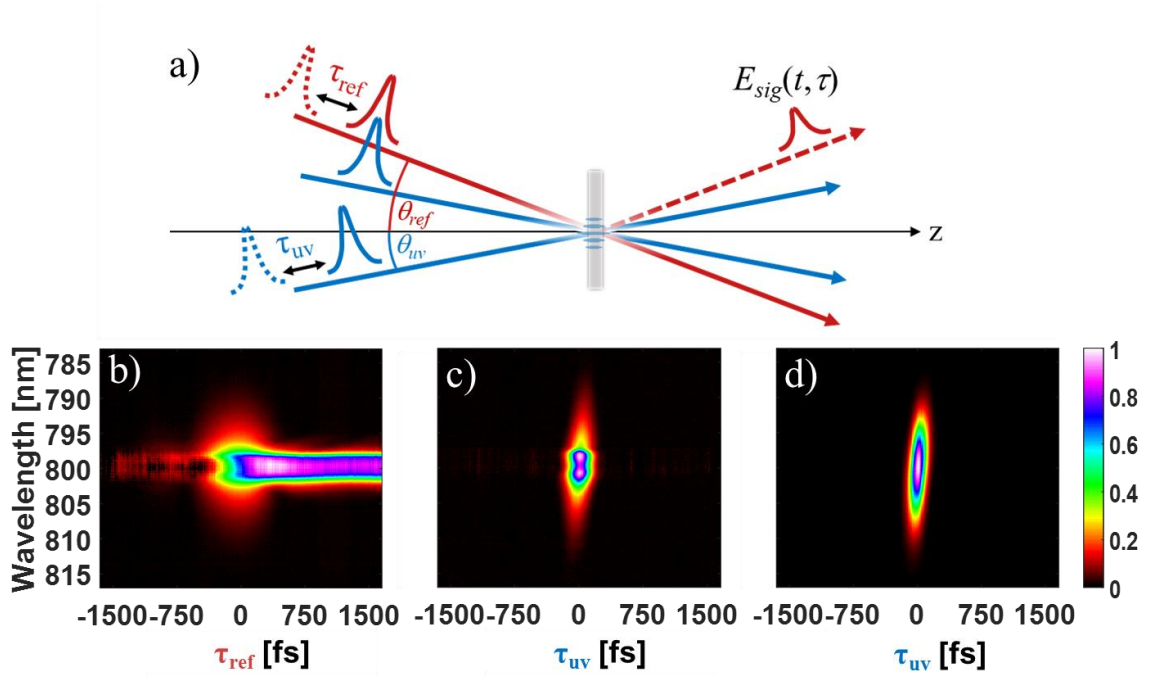
Figure 4.2 (a) A schematic of the beam geometry used in Induced-Grating XFROG. The amplitudes of raw traces generated by varying τ_{ref} (b) and τ_{uv} (c) in an absorbing medium (ZnS). (d) The intensity of the raw trace for the same measurement as (c), but instead using an instantaneous medium.

4.3.2 Generalized projections phase retrieval algorithm for slow media: Absorption

As illustrated above, the FROG trace in Figure 4.2(c) contains both an instantaneous and a non-instantaneous contribution which needs to be accounted for in the phase retrieval. We follow the approach first introduced by Delong et al. [120] where polarization gating FROG was done in the visible near a Raman resonance, which made a non-instantaneous contribution to the signal. The nonlinear signal $E_{sig}(t,\tau)$, is treated as a sum of the instantaneous and noninstantaneous contributions. Using an empirical model for the signal field we write:

$$E_{sig}(t,\tau) = E_{ref}(t - \tau_{ref}) \int_{-\infty}^{t} dt'\, R(t - t')E_{uv}^{*}(t')E_{uv}(t' - \tau_{uv}). \qquad (4.1)$$

In the above expression, $R(t)$ represents the response of the medium and is given by,

$$R(t) = \delta(t) + c_\Theta \Theta(t), \qquad (4.2)$$

where the instantaneous contribution is represented by the delta function, $\delta(t)$, the noninstantaneous contribution is represented by a Heavyside step function, $\Theta(t)$, and c_Θ is an adjustable constant. We chose this constant empirically, finding that a value of $c_\Theta = 5$, typically fit our data sufficiently well. Figure 4.3 shows an example of a simulation we did to determine $R(t)$. The comparison suggests that the simple model sufficiently captures the material response.
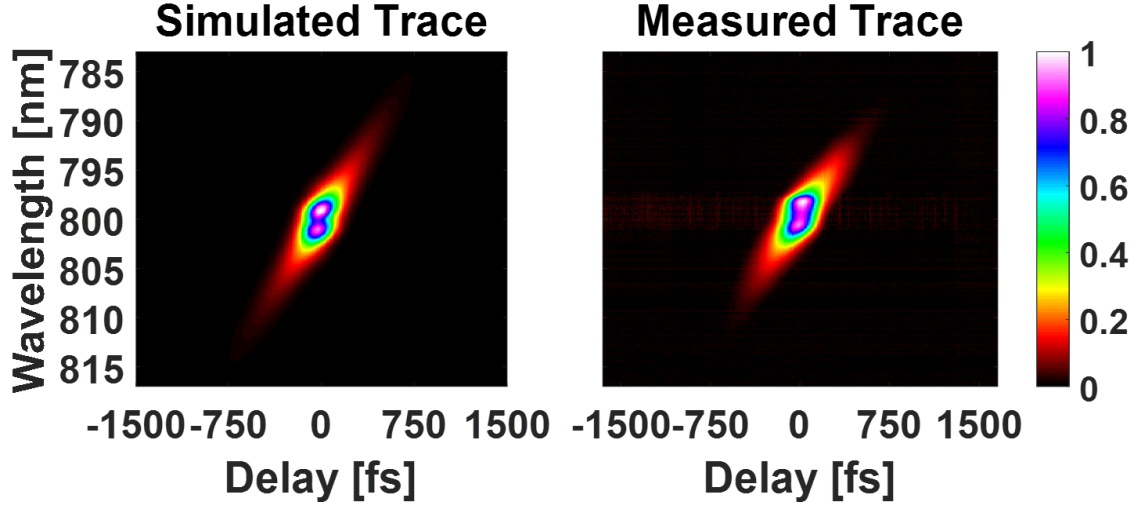
Figure 4.3 Simulated trace amplitude (left) and measured trace amplitude (right) for a chirped pulse. Simulation was generated using $E_{ref}(t)$ and $R(t)$ as described in the text above.

To retrieve the UV pulse from our spectrograms, the signal field given by Equation 4.1 and Equation 4.2 was incorporated into a modified GP phase retrieval algorithm where the FROG trace is given by $I_{FROG}(\omega, \tau) = |\mathscr{F}[E_{sig}(t, \tau)]|^2$, where $\mathscr{F}$ indicates a Fourier transformation. The algorithm that we used here follows the procedure outlined in [86], where the reference field is known, and an input, and the derivatives for the nonlinear signal given in Equation. 1 are used in the gradient minimization.

4.3.3 *IGXFROG measurements of UV pulses using an absorbing medium*

To illustrate the concept described above, that we can use absorption as the nonlinear response in a FROG measurement, we performed two sets of measurements. First we used 20 mm and 50 mm rods of SF11 glass to add chirp to test pulses centered at 400 nm. These measurements are shown in Figure 4.4(a)-(c). We used the modified GP algorithm discussed in Section 4.3.2 to reconstruct $E_{uv}(t)$ from the measured traces. The reconstructed

74

traces along with the retrieved pulses plotted vs. time and wavelength are shown in the 2nd, 3rd, and 4th rows of Figure 4.4 respectively. The second set of measurements were made on pulses centered 267 nm using a 50 mm rod of UV-grade fused silica (UVFS) to introduce chirp. These traces are shown in Figure 4.5 (a) and Figure 4.5(e). The reconstructed traces along with the retrieved pulses plotted vs. time and wavelength are shown in the 2nd, 3rd, and 4th rows of Figure 4.5 respectively. In the retrievals shown in Figure 4.4–Figure 4.5, the G errors (rms difference between the measured and retrieved trace intensities) [38] for each reconstruction were all below 1%. For each measurement, the raw trace was binned to a 128×128 array.
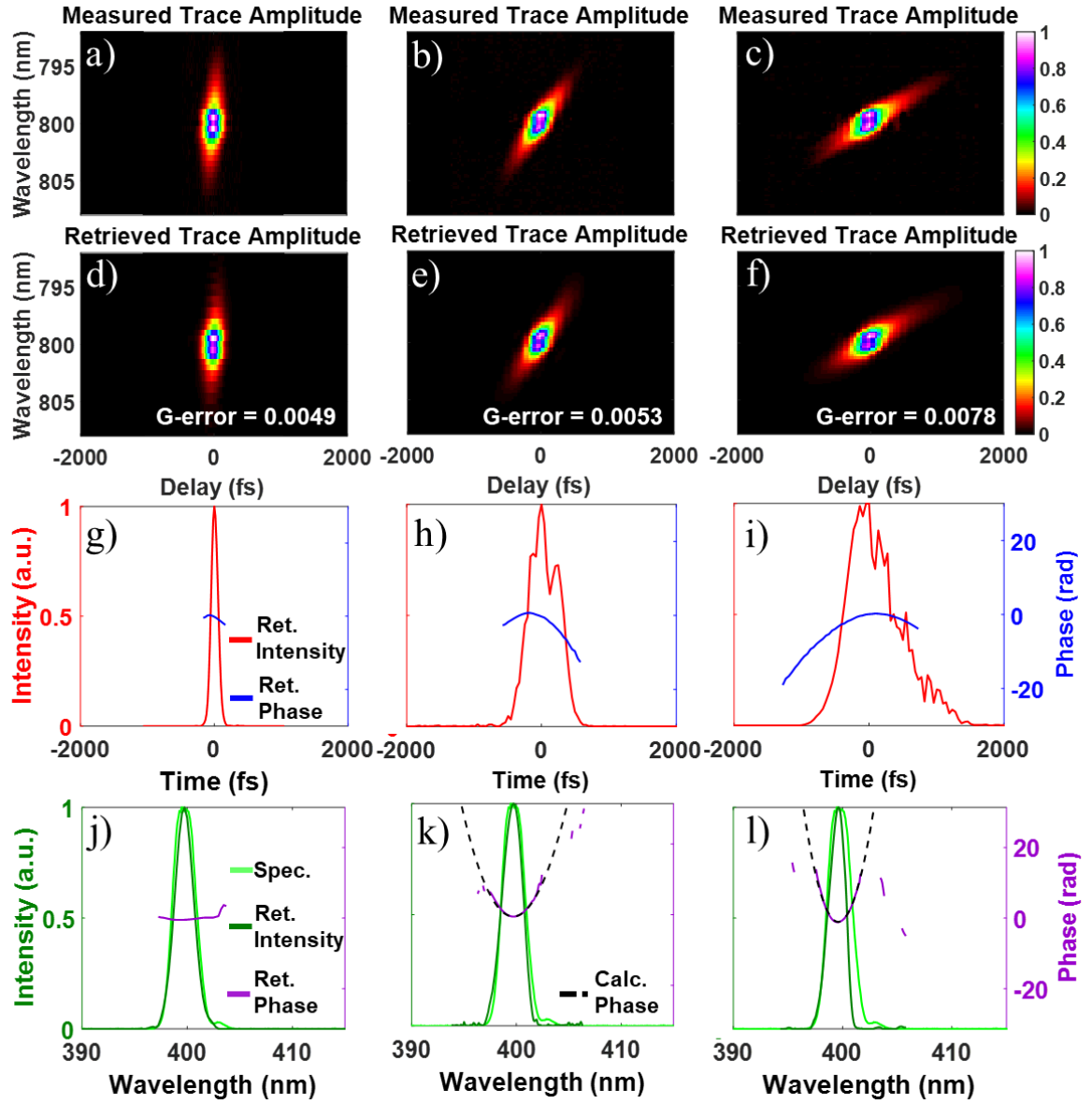
Figure 4.4 Measurements of chirped 400 nm pulses in an absorbing medium using an 800 nm reference pulse.
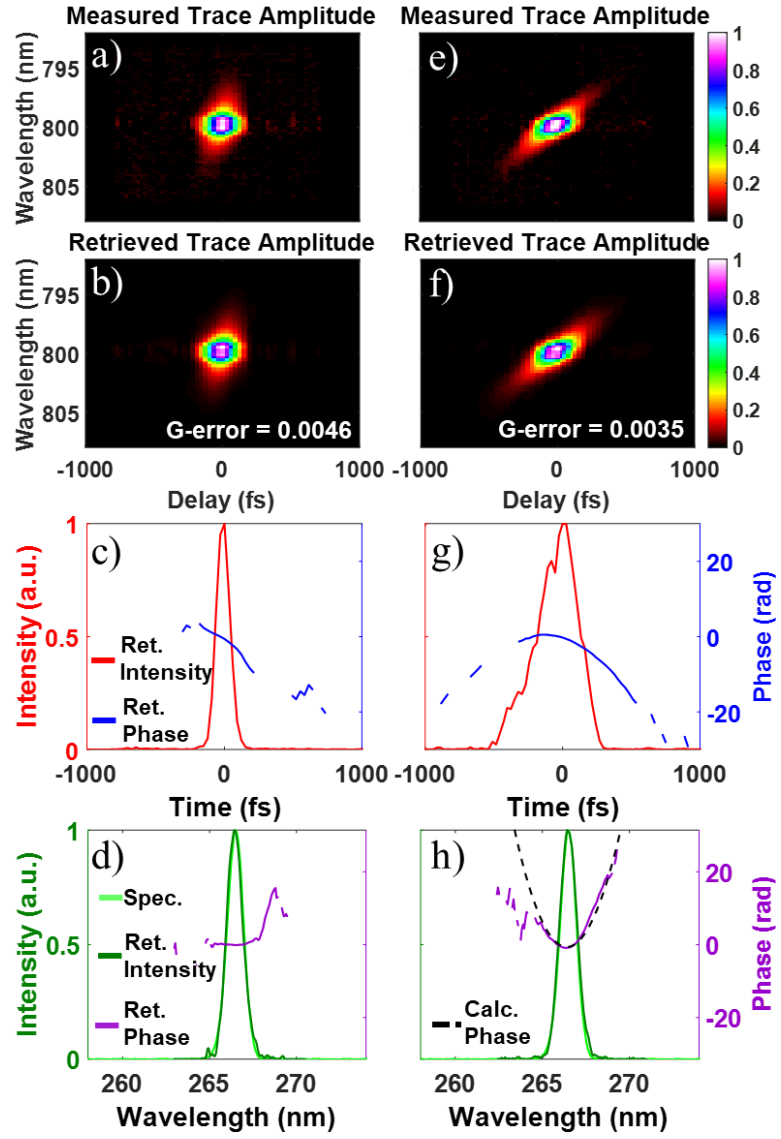
Figure 4.5 Measurements of chirped 267 nm pulses in an absorbing medium using an 800 nm reference pulse.

4.4   Discussion

The measurements presented above demonstrate that a femtosecond pulse can be measured using absorption as the nonlinear optical interaction or time-gate. As discussed in Section 4.3.1, although the absorption can take nanoseconds to recover, the fast, coherent FWM component, or the initial creation of the photoexcited carriers before they lose their coherence with the light, is an effectively instantaneous and phase-preserving process [37]. A key innovation here, is that by measuring the nonlinear signal versus the delay, τ_{uv}, between the pulses making the grating, we significantly reduce the slower incoherent contribution to the nonlinear signal. This can be understood intuitively by considering that the transient grating is only present when the interfering UV pulses temporally overlap, thus any component of the material response that lasts longer than their interference does not contribute to the nonlinear signal. Figure 4.2 illustrates this. Figure 4.2(b) shows a conventional TG measurement where the UV pulses temporally overlap and the reference pulse delay is scanned, which primarily probes the lifetime of the grating, τ_{ref}. The nonlinear signal versus the grating pulse pair delay, τ_{uv} much more closely resembles the measurement made in an instantaneous-responding medium which is shown for comparison Figure 4.2(d) (as also seen in [112]). The initial rise in the reference scan in Figure 4.2(b) contains the UV and NIR temporal profiles which could be extracted with a deconvolution [124], however this signal does not contain the phase of the UV pulse, only its amplitude.

The tilt seen in the measurements in Figure 4.4–Figure 4.5 clearly demonstrates that the IG XFROG measurements made in ZnS are sensitive to the phase of the unknown UV

78

pulses. The chirp, which was introduced with the glass rods, causes the redder colors to arrive before the bluer colors. More chirp resulted in more tilt. On top of the tilted component, there is a central region of the trace which remains unchanged when chirp is added; this is the non-phase containing contribution discussed in Sections 4.3.1 and 4.3.2 that was modeled with the step function, due to the fact that some decoherence happens within the pulse duration [37]. Note that it was important to set the delay of the reference pulse to 0-delay to maximize the relative contribution of the phase-containing contribution. 0-delay was found by performing a scan of τ_{ref} as shown in Figure 4.2(b), and then selecting the reference pulse delay which maximized the bandwidth of the nonlinear signal, was a good approach for finding 0-delay.

Appling the phase retrieval algorithm discussed in Section 4.3.2 to the measured IG XFROG traces further confirms that the pulses can be measured in an absorbing medium, and that the simple model in Equation 4.1 sufficiently captures the material response for this purpose. The reconstructed traces from each retrieval are shown in the second row of Figure 4.4–Figure 4.5. The G errors of $< 1\%$, indicate convergence of the algorithm [38]. In Figure 4.4(j)–(l) and Figure 4.5(d) and Figure 4.5(h) we compare the retrieved pulse spectrum (dark green) to an independent measurement of the pulse spectrum (light green) made using an Ocean Optics spectrometer, showing relatively good agreement. We also confirmed accurate retrievals by calculating the GDD introduced using the Sellmeier equations for SF11 [109] and UVFS [125], plotted as dashed black lines in Figure 4.4(k)-(l) and Figure 4.5(h). The calculated GDD is in good agreement with the retrieved spectral phases (purple). We note that the modulation seen the FROG traces was confirmed to be

79

from a weak post pulse in the reference pulse that came ~850 fs after the main pulse, as mentioned in Section 4.2. The long-lived grating in ZnS results in contributions to the nonlinear signal over a broad-time window, so that the weak post pulse in the reference also contributes to the nonlinear signal. Since we were not able to experimentally remove this artifact, incorporating the post pulse into our reference pulse shape as a weak replica of the main pulse made the IG XFROG retrievals more accurate.

An interesting direction for future work could be to develop an algorithm which extracts both the UV pulse and the medium's response function, similar to the double blind-FROG approach [38, 126]. Another option could be to extract the material response from a reference scan [124, 127]. Nevertheless, the measurements provided here indicate that the simple model in Equation 4.1 is sufficient, and this approach has the major advantage of being easy and fast to implement in the phase retrieval algorithm.

4.5   Conclusion

In summary, proof-of-principle measurements which demonstrate IG XFROG's ability to measure UV pulses using band-gap absorption as the nonlinear optical time-gate we demonstrated. We have seen that by scanning the delay between the two UV pulses, IG XFROG selectively detects the instantaneous, phase-preserving contribution to the nonlinear signal, the FWM part of the photoexcitation where the light remains coherent with the photoexcited electrons. A simple model for the response of the medium was also introduced and incorporated into a modified GP phase retrieval algorithm. This algorithm was used to retrieve chirped UV pulses centered at 400 nm and 267 nm from experimentally measured traces and showed that accurate measurements of the pulse's

spectral phase are obtained. While we demonstrated this method at 400 and 267 nm, the process of absorption, whether it is across the bandgap or into the continuum, (i.e. photoionization) is not strongly dependent on wavelength. Thus, these measurements suggest that IG XFROG is applicable deeper into the UV. As we will see in the next chapter, single-shot IG XFROG measurements should also be feasible [128] potentially giving access to single-shot optical-read-out pulse measurement from the UV to the x-ray range.

CHAPTER 5.

5.1   Introduction

Recent advances in ultrafast EUV and X-ray light sources provide direct access to fundamental time and length scales for biology, chemistry and materials physics [25, 129, 130]. However, such light pulses are challenging to measure due to the need for femtosecond time resolution at difficult-to-detect wavelengths. Also single-shot measurements are needed because severe pulse-to-pulse fluctuations are common. Here we demonstrate single shot, complete field measurements by applying a novel version of Frequency Resolved Optical Gating (FROG) [38]. An EUV FEL beam creates a transient grating containing the pulse's electric field information which is read out with a 400 nm probe pulse. By varying the time delay between two copies of the EUV pump, rather than between the pump and the probe, we separate the needed coherent wave-mixing from the slow incoherent response. Because this approach uses photoionization, it should be applicable from the vacuum ultraviolet to hard X-rays.

5.2   Motivation

Ultrafast EUV and X-ray FELs promise truly new insights by combining the coherence of lasers with X-ray scattering and spectroscopy [25, 129, 130]. However, to fully realize this potential, new diagnostics for complete field (amplitude and phase) measurement of these pulses are needed [131-134]. Most FELs display significant jitter in intensity, spectrum, and pulse duration, which limits signal-to-noise and resolution. Shot-

by-shot measurements of the pulse shapes would ameliorate many of these limitations. Also, more complete diagnostics can lead to better understanding and control, including new capabilities to produce sub-femtosecond pulses [135] and two-color pulses [136]. Moreover, complete field measurements would extend broadband phase-sensitive spectroscopies like 2D spectroscopy to shorter wavelengths [137].

Femtosecond pulses cannot be fully characterized with typical electronics, which are far too slow. However, attosecond resolution is accessible with nonlinear optics, where the light-matter interaction provides a fast "shutter". This concept is widely used, for example in FROG [38], which allows the electric field to be extracted from a spectrally resolved nonlinear optical signal versus delay (the FROG trace). A wide variety of nonlinear processes may be employed for FROG, although an instantaneous material response is preferred.

Extending FROG to shorter wavelengths is problematic for several reasons: first, short-wavelength spectrometers are low-throughput; second, nonlinear optics with EUV and X-ray pulses is in its infancy, with few reports [138-140] demonstrating coherent wave-mixing; and third, the dominant process is photoionization, with a slow material recovery. These difficulties have led to the use of photoelectron-based techniques for measuring EUV and X-ray pulses [48, 133, 134, 141-143].

In this paper we demonstrate an optically-detected measurement of short wavelength femtosecond pulses, addressing each challenge. First, diffracting an optical probe from an EUV-induced grating transfers the EUV pulse information to an optical field and allows high-efficiency detection and a single-shot geometry. Transient gratings have long been

used for FROG [38], but their potential to shift detection to a convenient wavelength was only recently recognized [86]. Second, introducing pulse-front-tilt in the probe beam allows sufficient time resolution [144], despite severe phase-matching angles, to identify the coherent four-wave-mixing (FWM) response of interest. Third, scanning the EUV pulse-pair separation uses the sub-femtosecond dephasing time of photoionization as an instantaneous gate [37]. We present a first demonstration by measuring the intensity and phase of 31.3 nm pulses at the FERMI FEL [25].

5.3 Experimental setup

Figure 5.1 summarizes our method. Two copies of the EUV beam (figure 1a) create an interference pattern, causing a spatial modulation in the sample's optical properties known as a transient grating [39]. An optical probe diffracts from the perturbed sample, gaining information about the material response and the EUV pulses. For optimal efficiency, the probe incidence angle should satisfy the phase matching, or Bragg, condition [39]; the large wavelength difference requires a steep probe angle (~45°). Unfortunately, steep angles would decrease time resolution to more than a picosecond because the probe averages over a time range $\delta t = (w/c) \tan \theta_{opt}$, where w is the probe beam width and c is the speed of light. Since the coherent FWM here is very short-lived, this averaging can blur the needed information. We overcome this by using a grism to introduce angular dispersion, so the optical pulse front impinges parallel to the sample surface [145, 146]. Figure 5.1(b) also shows how the crossing angle is used to map EUV pulse-pair delay to position for single-shot measurements. Imaging the sample along the in-page direction and spectrally resolving along the out-of-page direction yields the FROG trace. A novel

phase retrieval algorithm, taking the material response into account, is applied to extract

the amplitude and phase of single EUV pulses from the FROG traces (Fig, 1c).
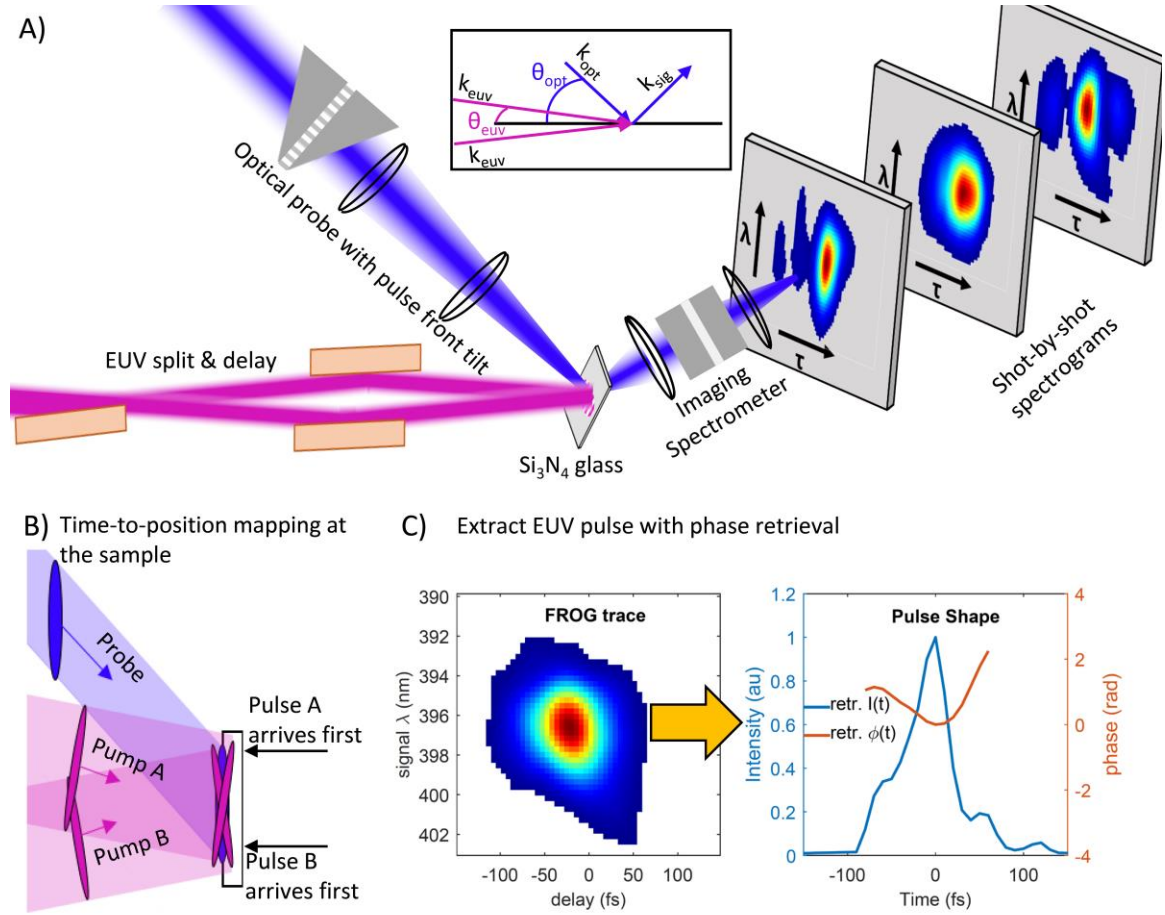
Figure 5.1 A) Experimental setup used to measure EUV pulses from the FERMI FEL.

5.4 FROG in the presence of Photoionozation

FROG almost always uses an instantaneous nonlinear response (with notable exceptions [120, 147]); however, our signal arises from photoionization (Figure 5.2(a)), causing a long recovery time [148]. Consequently, extracting the pump pulse from pump-probe data (Figure 5.2(b)) would require a challenging deconvolution [124, 134, 149]. Instead, we use the transient grating to separate the coherent FWM interaction, here present only near time zero, from the long-lived signal. A grating is only created if the material polarization induced by the first copy of the pump survives until the second copy arrives; this timescale is the dephasing time, and is related to the free induction decay [37]. By choosing a sample with a featureless absorption spectrum at the pump wavelength, the dephasing time will be nearly instantaneous. Consequently, even if the pump-excited sample has a slow recovery (Figure 5.2(b)), a transient grating as a function of pump-pump delay will roughly resemble a cross correlation made using an instantaneous medium [112] (Figure 5.2(c)).

Physically, an ionized atom supports a material polarization until the outgoing wave-packet loses spatial overlap with its hole. After that, the nonlinear signal contains only frequencies already in the probe, has no phase relationship with the pump, and can be considered an incoherent pump-probe signal. The difference between coherent FWM and incoherent pump-probe is demonstrated in Figure 5.2(b) by the increase in bandwidth at time zero compared to later times. By inspection of Figure 5.2(b) and Figure 5.2(c), we see that this extra bandwidth is present in Figure 5.2(c), indicating the coherent FWM response is preserved.
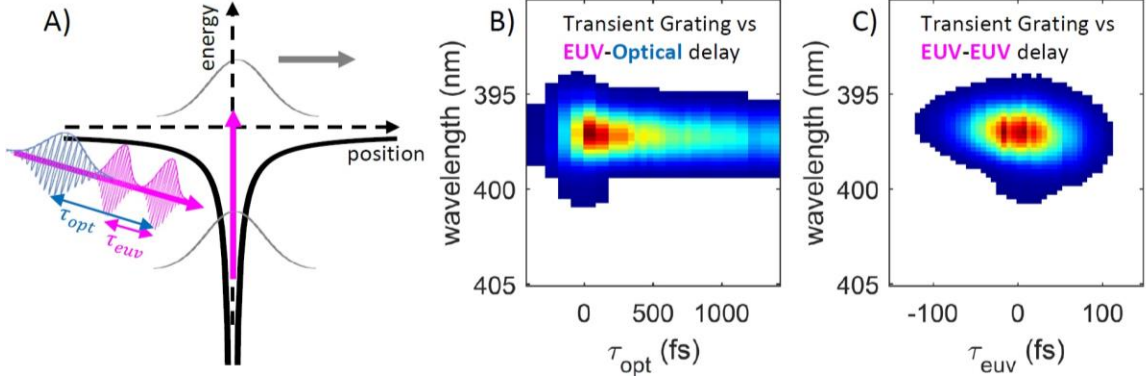
Figure 5.2 Isolating the coherent material response. A) An electron absorbs a single photon from the EUV pulse pair: while the outgoing wave-packet overlaps the nascent hole, a coherent polarization exists. B) The spectrally-resolved signal versus pump-probe delay. C) Signal versus pump-pair.

5.5   Modeling the nonlinear signal field

Now that we have demonstrated that the spectrogram preserves the coherent FWM process, we can implement FROG in the EUV using photoionization and scanning the pump-pump delay. While this largely isolates the coherent FWM, there remains some incoherent response that must be taken into account. The general theory for resonantly-excited FWM involves a triple convolution with response functions describing material evolution after each pulse and for each possible time-ordering [132]. Due to the iterative nature of FROG phase retrievals, it seems highly desirable to seek a simplified treatment. In general the FROG trace is given by,

$$I_{FROG}(\omega, \tau) = \left| \mathscr{F}_t \left(\mathrm{E_{sig}}(t, \tau) \right) \right|^2,$$

87

where $\mathscr{F}_t$ indicates a Fourier transformation with respect to time. To write down the signal field, $E_{\text{sig}}(t, \tau)$, we note that the timescale for an electron to leave an atom is known to be on the order of tens of attoseconds, [150] which we take to be essentially instantaneous. We therefore neglect the response function associated with material evolution between the two copies of the pump pulse. We also neglect material evolution after the non-resonant probe. This allows us to simplify the signal field to:

$$E_{sig}\big(t, \tau_{opt}, \tau_{euv}\big) = E_{opt}\big(t - \tau_{opt}\big) \int_{-\infty}^{t} R(t - t')E_{euv}(t')E_{euv}^*(t' - \tau_{euv})dt'$$

where $R(t)$ is a response function describing the material response to having absorbed one EUV photon and is the material response function given by:

$$R(t) = \delta(t) + c_\theta \Theta(t),$$

where $\delta(t)$ is the Dirac delta function, representing the coherent FWM, $\Theta(t)$ is the Heaviside step function, representing the incoherent part of the response, and c_θ is an adjustable complex constant empirically chosen by comparing measured data to simulated data under a wide variety of experimental conditions. This model describes an instantaneous dephasing and assumes the ground-state recovery is slow compared to the pulses. We find this simple model sufficient for applying phase retrieval to extract the EUV field.

5.6   A Derivative-Free Generalized-projections Phase Retrieval Algorithm

For pulse retrieval we developed a custom derivative-free generalized projections algorithm, since derivatives are more difficult to compute when the response is not instantaneous. The measured FROG trace is first binned onto a square $N \times N$ grid, with $N = 64$. The trace is conditioned to minimize noise contribution in a standard way. In the algorithm we use transform-limited pulse corresponding to an independently measured spectrum to seed the initial guess for the electric field $E_{euv}(t)$ to be reconstructed. The seed, along with the reference pulse $E_{opt}(t)$ and the response function $R(t)$ are then used to compute the initial $E_{sig}(t,\tau)$ through the equation above. Fast Fourier transform (FFT) is then applied on the t dimension to compute $X_{sig}(\omega,\tau) = \mathscr{F}_t[E_{sig}(t,\tau)]$. The $X_{sig}(\omega,\tau)$ is now a square matrix of complex numbers. The so called "data projection" is then implemented by replacing the magnitude of $X_{sig}(\omega,\tau)$ with experimentally measured values, followed by an inverse $\mathscr{F}_t$ to obtain $E'_{sig}(t,\tau)$. On the first iteration of the algorithm the extraction of the electric field from $E'_{sig}(t,\tau)$ is done using the simple "vanilla" approach [38] as

$$E'_{opt}(t) = \int E'_{sig}(t,\tau)d\tau$$

This new field $E'_{opt}(t)$ serves as the new seed for the next iteration. On the second and subsequent iterations the "data projection" is implemented in exactly the same manner, while the "vanilla" step is replaced with a "nonlinear projection" – a minimization of the norm

$$Z_{err} = \iint \left| E'_{sig}(t,\tau) - E_{opt}(t) \int_{-\infty}^{t} R(t-t') E_{euv}(t') E^*_{euv}(t'-\tau) dt' \right|^2 dt \, d\tau$$

where the $2N$ individual real and imaginary values of the field $E_{euv}(t)$ at each of N time points comprise the vector of independent variables. To simplify implementation and avoid potential derivation errors we employ a simple derivative-free simplex downhill minimization routine in this step. This routine takes a set of $2N+1$ vectors, each of length $2N$. Each vector in the set is formed by taking $E'_{euv}(t)$ from the previous iteration and perturbing one of its $2N$ values (real or imaginary part of the electric field at one of N time points) by a small amount. This procedure forms the initial simplex with $2N+1$ apexes. The routine then allows the simplex to crawl in this space searching for a minimum of the Z_{err}. This minimization routine is fairly robust, but requires a large number of function calls to compute $E_{sig}(t,\tau)$. To accelerate these function evaluations we observe that the integral in the expression for $E_{sig}(t,\tau)$ is a convolution of the response function and the field product $E_{euv}(t') E^*_{euv}(t'-\tau)$, where τ is a parameter, so that we can utilize $\mathscr{F}_t$ to compute it, taking proper precautions against aliasing.

5.7 Experimental Results and Discussion

Figure 5.3 shows measured single-shot FROG traces along with the results of phase retrieval. The left-side column shows a measurement under FERMI's standard conditions and represents a typical pulse. The measured spectrogram reveals a small amount of chirp in the tilt, and the overall shape appears well-represented in the retrieved trace.
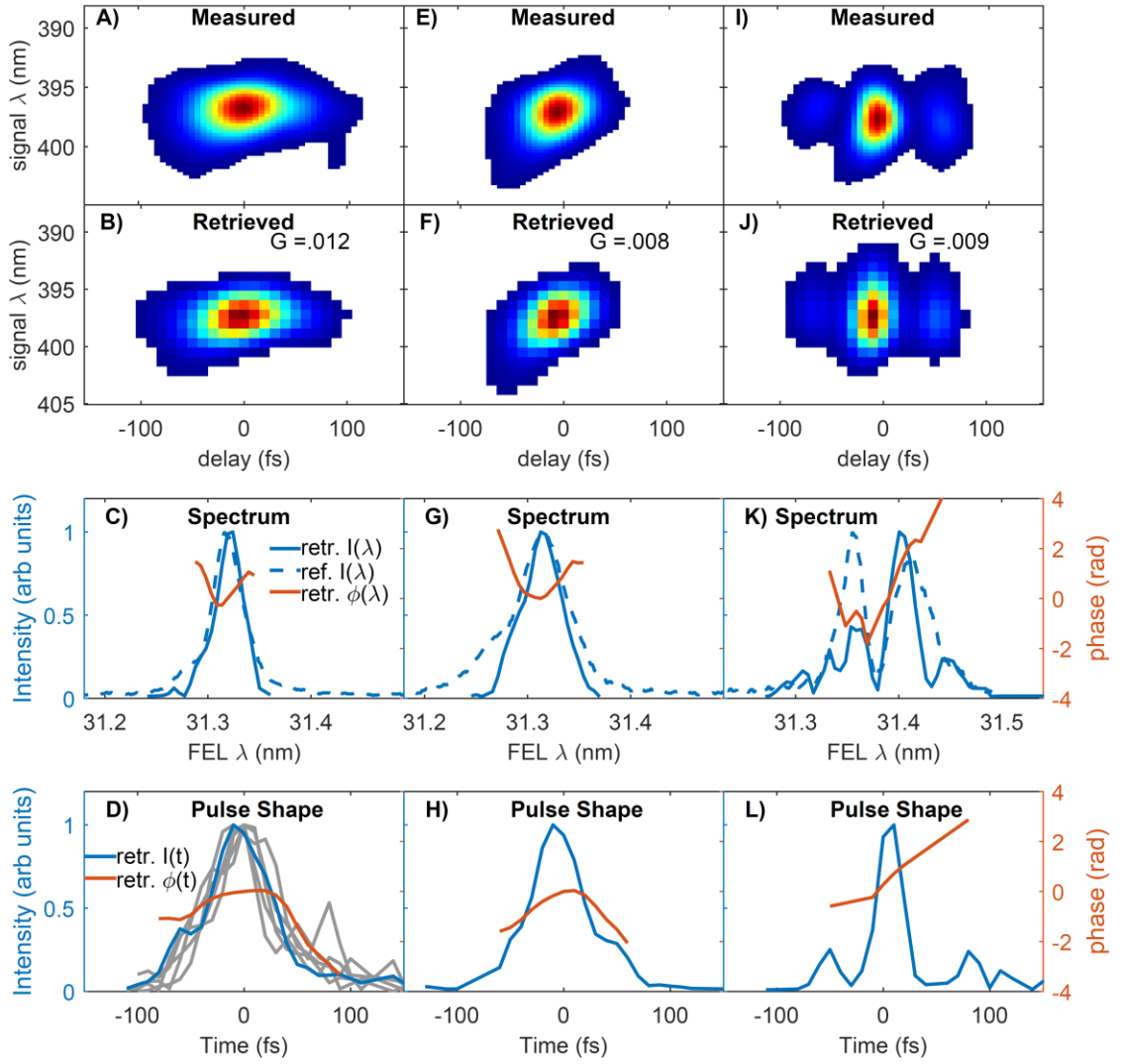
Figure 5.3 Measurements of single EUV pulses.

Figure 5.3(c) shows the retrieved spectral intensity and phase compared to an independently measured spectrum of the same pulse, showing a good match except for the tails. Figure 5.3(d) shows the retrieved pulse as a function of time, which shows a main pulse that is reasonably fit by a 71±6fs Gaussian, compared to 70fs predicted [134]. Gray

lines are retrieved intensities for several other pulses, showing good pulse-to-pulse stability as expected from a seeded FEL.

As a seeded FEL, FERMI uses an optical "seed" laser to manipulate its electron bunch in order to control the emission of EUV light. There is much interest in shaping the seed pulse to achieve more sophisticated control over the EUV pulse. The middle column of Figure 5.3, therefore, shows a measurement while chirping the seed laser, which produced more bandwidth. Interestingly, although the trace appears significantly narrowed in time, the retrieved electric field is only modestly shorter (60 fs) than in the standard configuration. This comes from the residual incoherent signal, which dominates the central portion of the spectrogram and is not indicative of pulse shape. The right-side column shows a measurement made with a low-temporal coherence FEL beam, which produced structured pulses. For these two columns, despite low retrieval errors, there are discrepancies remaining in the retrieved spectra compared to the reference spectra. It seems likely this stems from signal-to-noise limitations in the dark-blue tails of the FROG traces, which spread farther when the pump has more bandwidth, but may be due to an insufficiently accurate model for the signal. Our signal-to-noise was limited by probe scatter inside the EUV vacuum chamber, and is not indicative of the technique's limitations.

5.8   Conclusions

In summary, a novel, all-optical measurement of the pulse shape of short-wavelength FEL pulses is described which is expected to be generally applicable across the EUV, soft- and hard-x-ray spectral ranges, and also to table top EUV sources. Single-shot

measurements were achieved, paving the way for online diagnostics of detailed pulse shapes at XFEL facilities.

APPENDIX A.
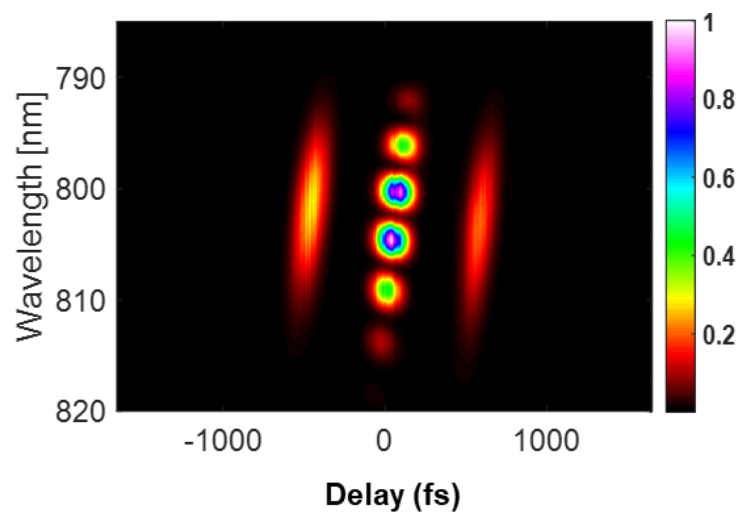
Figure A.1 Experimentally-measured IG XFROG trace of a double pulse with a temporally broad reference pulse.

REFERENCES

1. T. Gaumnitz, A. Jain, Y. Pertot, M. Huppert, I. Jordan, F. Ardana-Lamas, and H. J. Wörner, "Streaking of 43-attosecond soft-X-ray pulses generated by a passively CEP-stable mid-infrared driver," Optics express **25**, 27506-27518 (2017).

2. A. H. Zewail, "Laser Femtochemistry," Science **242**, 1645 (1988).

3. A. Assion, T. Baumert, M. Bergt, T. Brixner, B. Kiefer, V. Seyfried, M. Strehle, and G. Gerber, "Control of Chemical Reactions by Feedback-Optimized Phase-Shaped Femtosecond Laser Pulses," Science **282**, 919 (1998).

4. M. Maiuri, M. Garavelli, and G. Cerullo, "Ultrafast Spectroscopy: State of the Art and Open Challenges," Journal of the American Chemical Society **142**, 3-15 (2020).

5. R. Boyd, *Nonlinear Optics* (Academic Press, 2008).

6. W. R. Zipfel, R. M. Williams, and W. W. Webb, "Nonlinear magic: multiphoton microscopy in the biosciences," Nature Biotechnology **21**, 1369-1377 (2003).

7. X. Liu, D. Du, and G. Mourou, "Laser ablation and micromachining with ultrashort laser pulses," IEEE Journal of Quantum Electronics **33**, 1706-1716 (1997).

8. M. Lewenstein, P. Balcou, M. Y. Ivanov, A. L'Huillier, and P. B. Corkum, "Theory of high-harmonic generation by low-frequency laser fields," Physical Review A **49**, 2117-2132 (1994).

9. Z. Chang, A. Rundquist, H. Wang, M. M. Murnane, and H. C. Kapteyn, "Generation of coherent soft X rays at 2.7 nm using high harmonics," Physical Review Letters **79**, 2967 (1997).

10. I. P. Christov, M. M. Murnane, and H. C. Kapteyn, "High-harmonic generation of attosecond pulses in the "single-cycle" regime," Physical Review Letters **78**, 1251 (1997).

11. T. H. Maiman, "Stimulated Optical Radiation in Ruby," Nature **187**, 493-494 (1960).

12. F. J. McClung, and R. W. Hellwarth, "Giant Optical Pulsations from Ruby," Journal of Applied Physics **33**, 828-829 (1962).

13. F. J. McClung, and R. W. Hellwarth, "Characteristics of giant optical pulsations from ruby," Proceedings of the IEEE **51**, 46-53 (1963).

14. R. Paschotta, and U. Keller, "Passive mode locking with slow saturable absorbers," Applied Physics B **73**, 653-662 (2001).

15. E. P. Ippen, "Principles of passive mode locking," Applied Physics B **58**, 159-170 (1994).

16. R. L. Fork, O. E. Martinez, and J. P. Gordon, "Negative dispersion using pairs of prisms," Optics Letters **9**, 150-152 (1984).

17. D. E. Spence, P. N. Kean, and W. Sibbett, "60-fsec pulse generation from a self-mode-locked Ti: sapphire laser," Optics letters **16**, 42-44 (1991).

18. U. Morgner, F. X. Kärtner, S.-H. Cho, Y. Chen, H. A. Haus, J. G. Fujimoto, E. P. Ippen, V. Scheuer, G. Angelow, and T. Tschudi, "Sub-two-cycle pulses from a Kerr-lens mode-locked Ti: sapphire laser," Optics letters **24**, 411-413 (1999).

19. D. Strickland, and G. Mourou, "Compression of amplified chirped optical pulses," Optics Communications **55**, 447-449 (1985).

20. M. Pessot, J. Squier, G. Mourou, and D. J. Harter, "Chirped-pulse amplification of 100-fsec pulses," Optics letters **14**, 797-799 (1989).

21. J. M. Madey, "Stimulated emission of bremsstrahlung in a periodic magnetic field," Journal of Applied Physics **42**, 1906-1913 (1971).

22. D. A. Deacon, L. Elias, J. M. Madey, G. Ramian, H. Schwettman, and T. I. Smith, "First operation of a free-electron laser," Physical Review Letters **38**, 892 (1977).

23. W. a. Ackermann, G. Asova, V. Ayvazyan, A. Azima, N. Baboi, J. Bähr, V. Balandin, B. Beutner, A. Brandt, and A. Bolzmann, "Operation of a free-electron laser from the extreme ultraviolet to the water window," Nature photonics **1**, 336-342 (2007).

24. P. Emma, R. Akre, J. Arthur, R. Bionta, C. Bostedt, J. Bozek, A. Brachmann, P. Bucksbaum, R. Coffee, and F.-J. Decker, "First lasing and operation of an ångstrom-wavelength free-electron laser," nature photonics **4**, 641-647 (2010).

25. E. Allaria, R. Appio, L. Badano, W. Barletta, S. Bassanese, S. Biedron, A. Borga, E. Busetto, D. Castronovo, and P. Cinquegrana, "Highly coherent and stable pulses from the FERMI seeded free-electron laser in the extreme ultraviolet," Nature Photonics **6**, 699-704 (2012).

26. A. Kondratenko, and E. Saldin, "Generating of coherent radiation by a relativistic electron beam in an ondulator," Part. Accel. **10**, 207-216 (1980).

27. R. Bonifacio, C. Pellegrini, and L. Narducci, "Collective instabilities and high-gain regime free electron laser," in *AIP Conference Proceedings*(American Institute of Physics1984), pp. 236-259.

28. E. Saldin, E. Schneidmiller, and M. V. Yurkov, *The physics of free electron lasers* (Springer Science & Business Media, 1999).

29. G. Margaritondo, "X-Ray Light Sources," (2020).

30. J. Feldhaus, E. L. Saldin, J. R. Schneider, E. A. Schneidmiller, and M. V. Yurkov, "Possible application of X-ray optical elements for reducing the spectral bandwidth of an X-ray SASE FEL," Optics Communications **140**, 341-352 (1997).

31. J. Amann, W. Berg, V. Blank, F. J. Decker, Y. Ding, P. Emma, Y. Feng, J. Frisch, D. Fritz, J. Hastings, Z. Huang, J. Krzywinski, R. Lindberg, H. Loos, A. Lutman, H. D. Nuhn, D. Ratner, J. Rzepiela, D. Shu, Y. Shvyd'ko, S. Spampinati, S. Stoupin, S. Terentyev, E. Trakhtenberg, D. Walz, J. Welch, J. Wu, A. Zholents, and D. Zhu, "Demonstration of self-seeding in a hard-X-ray free-electron laser," Nature Photonics **6**, 693-698 (2012).

32. L. H. Yu, "Generation of intense uv radiation by subharmonically seeded single-pass free-electron lasers," Physical Review A **44**, 5178 (1991).

33. K.-J. Kim, Z. Huang, and R. Lindberg, *Synchrotron radiation and free-electron lasers* (Cambridge university press, 2017).

34. E. Allaria, D. Castronovo, P. Cinquegrana, P. Craievich, M. Dal Forno, M. Danailov, G. D'Auria, A. Demidovich, G. De Ninno, and S. Di Mitri, "Two-stage seeded soft-X-ray free-electron laser," Nature Photonics **7**, 913-918 (2013).

35. C. Bocchetta, "FERMI@ Elettra FEL Conceptual Design Report," Elettra-Sincrotrone, Trieste, Italy (2007).

36. R. Trebino, "Ultrafast Optics Course."

37. A. Weiner, *Ultrafast optics* (John Wiley & Sons, 2011).

38. R. Trebino, *Frequency-Resolved Optical Gating: The Measurement of Ultrashort Laser Pulses* (Springer US, 2000).

39. H. J. Eichler, P. Günter, and D. W. Pohl, *Laser-induced dynamic gratings* (Springer, 2013).

40. J.-C. Diels, E. W. Van Stryland, and D. Gold, "Investigation of the Parameters Affecting Subpicosecond Pulse Durations in Passively Mode Locked Dye Lasers," (Springer Berlin Heidelberg, Berlin, Heidelberg, 1978), pp. 117-120.

41. J.-C. M. Diels, J. J. Fontaine, I. C. McMichael, and F. Simoni, "Control and measurement of ultrashort pulse shapes (in amplitude and phase) with femtosecond accuracy," Applied Optics **24**, 1270-1282 (1985).

42. K. Naganuma, K. Mogi, and H. Yamada, "General method for ultrashort light pulse chirp measurement," IEEE Journal of Quantum Electronics **25**, 1225-1233 (1989).

43. J. Chung, and A. Weiner, "Ambiguity of ultrashort pulse shapes retrieved from the intensity autocorrelation and the power spectrum," IEEE Journal of Selected Topics in Quantum Electronics **7**, 656-666 (2001).

44. D. Kane, and R. Trebino, "Measuring the intensity and phase of a femtosecond pulse using spectrally resolved self-diffraction," in *Annual Meet. Opt. Soc. Amer.*(1991).

45. I. Amat-Roldán, I. G. Cormack, P. Loza-Alvarez, E. J. Gualda, and D. Artigas, "Ultrashort pulse characterisation with SHG collinear-FROG," Optics express **12**, 1169-1178 (2004).

46. G. Stibenz, and G. Steinmeyer, "Interferometric frequency-resolved optical gating," Optics express **13**, 2617-2626 (2005).

47. X. Gu, L. Xu, M. Kimmel, E. Zeek, P. O'Shea, A. P. Shreenath, R. Trebino, and R. S. Windeler, "Frequency-resolved optical gating and single-shot spectral measurements reveal fine structure in microstructure-fiber continuum," Optics letters **27**, 1174-1176 (2002).

48. Y. Mairesse, and F. Quéré, "Frequency-resolved optical gating for complete reconstruction of attosecond bursts," Physical Review A **71**, 011401 (2005).

49. J. M. Dudley, F. Gutty, S. Pitois, and G. Millot, "Complete characterization of terahertz pulse trains generated from nonlinear processes in optical fibers," IEEE Journal of Quantum Electronics **37**, 587-594 (2001).

50. P. O'shea, M. Kimmel, X. Gu, and R. Trebino, "Highly simplified device for ultrashort-pulse measurement," Optics letters **26**, 932-934 (2001).

51. C. Radzewicz, P. Wasylczyk, and J. Krasinski, "A poor man's FROG," Optics Communications **186**, 329-333 (2000).

52. J. N. Sweetser, D. N. Fittinghoff, and R. Trebino, "Transient-grating frequency-resolved optical gating," Optics Letters **22**, 519-521 (1997).

53. S. Linden, J. Kuhl, and H. Giessen, "Amplitude and phase characterization of weak blue ultrashort pulses by downconversion," Optics letters **24**, 569-571 (1999).

54.   Q. Cao, X. Gu, E. Zeek, M. Kimmel, R. Trebino, J. Dudley, and R. S. Windeler, "Measurement of the intensity and phase of supercontinuum from an 8-mm-long microstructure fiber," Applied Physics B **77**, 239-244 (2003).

55.   T. C. Wong, M. Rhodes, and R. Trebino, "Single-shot measurement of the complete temporal intensity and phase of supercontinuum," Optica **1**, 119-124 (2014).

56.   A. Ermolov, H. Valtna-Lukner, J. Travers, and J. R. P. St, "Characterization of few-fs deep-UV dispersive waves by ultra-broadband transient-grating XFROG," Opt Lett **41**, 5535-5538 (2016).

57.   T. Sekikawa, T. Kanai, and S. Watanabe, "Frequency-resolved optical gating of femtosecond pulses in the extreme ultraviolet," Physical review letters **91**, 103902 (2003).

58.   J. Liu, Y. Feng, H. Li, P. Lu, H. Pan, J. Wu, and H. Zeng, "Supercontinuum pulse measurement by molecular alignment based cross-correlation frequency resolved optical gating," Optics express **19**, 40-46 (2011).

59.   T. Jones, P. Šušnjar, R. Petkovšek, and R. Trebino, "High-Sensitivity, Simple Frequency-Resolved-Optical-Gating Device," IEEE Journal of Quantum Electronics **56**, 1-6 (2020).

60.   P. Šušnjar, T. Jones, and R. Trebino, "Crystal-configuration considerations for higher-sensitivity picosecond-pulse SHG FROG," IEEE Journal of Quantum Electronics **56**, 1-8 (2020).

61.   K. K. Chen, J. H. Price, S.-u. Alam, J. R. Hayes, D. Lin, A. Malinowski, and D. J. Richardson, "Polarisation maintaining 100W Yb-fiber MOPA producing µJ pulses tunable in duration from 1 to 21 ps," Optics express **18**, 14385-14394 (2010).

62.   M. Rhodes, G. Steinmeyer, and R. Trebino, "Standards for ultrashort-laser-pulse-measurement techniques and their consideration for self-referenced spectral interferometry," Applied Optics **53**, D1-D11 (2014).

63.   M. Rhodes, G. Steinmeyer, J. Ratner, and R. Trebino, "Pulse-shape instabilities and their measurement," Laser & Photonics Reviews **7**, 557-565 (2013).

64.   M. Rhodes, Z. Guang, and R. Trebino, "Unstable and multiple pulsing can be invisible to ultrashort pulse measurement techniques," Applied Sciences **7**, 40 (2017).

65.   M. H. Asghari, Y. Park, and J. Azaña, "Complex-field measurement of ultrafast dynamic optical waveforms based on real-time spectral interferometry," Optics Express **18**, 16526-16538 (2010).

66. D. N. Fittinghoff, J. L. Bowie, J. N. Sweetser, R. T. Jennings, M. A. Krumbügel, K. W. DeLong, R. Trebino, and I. A. Walmsley, "Measurement of the intensity and phase of ultraweak, ultrashort laser pulses," Optics letters **21**, 884-886 (1996).

67. S.-D. Yang, A. M. Weiner, K. R. Parameswaran, and M. M. Fejer, "Ultrasensitive second-harmonic generation frequency-resolved optical gating by aperiodically poled LiNbO 3 waveguides at 1.5?? m," Optics letters **30**, 2164-2166 (2005).

68. H. Miao, S.-D. Yang, C. Langrock, R. V. Roussev, M. Fejer, and A. M. Weiner, "Ultralow-power second-harmonic generation frequency-resolved optical gating using aperiodically poled lithium niobate waveguides," JOSA B **25**, A41-A53 (2008).

69. M. Thomson, J. Dudley, L. Barry, and J. Harvey, "Complete pulse characterization at 1.5 µm by cross-phase modulation in optical fibers," Optics letters **23**, 1582-1584 (1998).

70. Y. Park, M. Scaffardi, A. Malacarne, L. Potì, and J. Azaña, "Linear, self-referenced technique for single-shot and real-time full characterization of (sub-) picosecond optical pulses," Optics letters **35**, 2502-2504 (2010).

71. J. Bromage, C. Dorrer, I. Begishev, N. Usechak, and J. Zuegel, "Highly sensitive, single-shot characterization for pulse widths from 0.4 to 85 ps using electro-optic shearing interferometry," Optics letters **31**, 3523-3525 (2006).

72. C. Dorrer, and I. Kang, "Linear self-referencing techniques for short-optical-pulse characterization," JOSA B **25**, A1-A12 (2008).

73. C. Dorrer, and I. Kang, "Simultaneous temporal characterization of telecommunication optical pulses and modulators by use of spectrograms," Optics Letters **27**, 1315-1317 (2002).

74. C. Dorrer, and I. Kang, "Highly sensitive direct characterization of femtosecond pulses by electro-optic spectral shearing interferometry," Optics letters **28**, 477-479 (2003).

75. F. Li, Y. Park, and J. Azaña, "Complete temporal pulse characterization based on phase reconstruction using optical ultrafast differentiation (PROUD)," Optics letters **32**, 3364-3366 (2007).

76. P. Kockaert, J. Azaña, L. R. Chen, and S. LaRochelle, "Full characterization of uniform ultrahigh-speed trains of optical pulses using fiber Bragg gratings and linear detectors," IEEE Photonics Technology Letters **16**, 1540-1542 (2004).

77. J. Azaña, N. K. Berger, B. Levit, and B. Fischer, "Spectro-temporal imaging of optical pulses with a single time lens," IEEE Photonics Technology Letters **16**, 882-884 (2004).

78. I. Kang, and C. Dorrer, "Highly sensitive differential tomographic technique for real-time ultrashort pulse characterization," Optics letters **30**, 1545-1547 (2005).

79. A. Pasquazi, M. Peccianti, Y. Park, B. E. Little, S. T. Chu, R. Morandotti, J. Azaña, and D. J. Moss, "Sub-picosecond phase-sensitive optical pulse characterization on a chip," Nature Photonics **5**, 618-623 (2011).

80. "SNLO. AS-Photonics. Accessed: Feb. 2, 2020. [Online]. Available:

http://www.as-photonics.com/snlo."

81. P. O'Shea, S. Akturk, M. Kimmel, and R. Trebino, "Practical issues in ultra-short-pulse measurements with 'GRENOUILLE'," Applied Physics B **79**, 683-691 (2004).

82. H. Wang, and A. M. Weiner, "Efficiency of short-pulse type-I second-harmonic generation with simultaneous spatial walk-off, temporal walk-off, and pump depletion," IEEE journal of quantum electronics **39**, 1600-1618 (2003).

83. E. Zeek, A. Shreenath, P. O'Shea, M. Kimmel, and R. Trebino, "Simultaneous automatic calibration and direction-of-time removal in frequency-resolved optical gating," Applied physics B **74**, s265-s271 (2002).

84. R. Jafari, T. Jones, and R. Trebino, "100% reliable algorithm for second-harmonic-generation frequency-resolved optical gating," Optics express **27**, 2112-2124 (2019).

85. R. Jafari, and R. Trebino, "Extremely robust pulse retrieval from even noisy second-harmonic-generation frequency-resolved optical gating traces," IEEE Journal of Quantum Electronics **56**, 1-8 (2019).

86. T. Jones, W. K. Peters, A. Efimov, R. L. Sandberg, D. Yarotski, R. Trebino, and P. Bowlan, "Encoding the complete electric field of an ultraviolet ultrashort laser pulse in a near-infrared nonlinear-optical signal," Opt Express **28**, 26850-26860 (2020).

87. M. Bauer, "Femtosecond ultraviolet photoelectron spectroscopy of ultra-fast surface processes," Journal of Physics D: Applied Physics **38**, R253 (2005).

88. M. Chergui, "Ultrafast molecular photophysics in the deep-ultraviolet," The Journal of Chemical Physics **150**, 070901 (2019).

89. H. Ihee, J. Cao, and A. H. Zewail, "Ultrafast electron diffraction of transient [Fe (CO) 4]: determination of molecular structure and reaction pathway," Angewandte Chemie **113**, 1580-1584 (2001).

90. P. Siffalovic, M. Drescher, M. Spieweck, T. Wiesenthal, Y. Lim, R. Weidner, A. Elizarov, and U. Heinzmann, "Laser-based apparatus for extended ultraviolet

femtosecond time-resolved photoemission spectroscopy," Review of Scientific Instruments **72**, 30-35 (2001).

91. J. E. Balmer, D. Bleiner, and F. Staub, "Extreme ultraviolet lasers: principles and potential for next-generation lithography," Journal of Micro/Nanolithography, MEMS, and MOEMS **11**, 021119 (2012).

92. G. Mincuzzi, A. Bourtereau, A. Rebière, H. Laborie, M. Faucon, M. Delaigue, K. Mishchik, C. Hoenninger, E. Audouard, and R. Kling, "Pulse to pulse control in micromachining with femtosecond lasers," in *Laser-based Micro-and Nanoprocessing XIV*(International Society for Optics and Photonics2020), p. 112681F.

93. J. Klein-Wiele, J. Bekesi, and P. Simon, "Sub-micron patterning of solid materials with ultraviolet femtosecond pulses," Applied Physics A **79**, 775-778 (2004).

94. U. Selig, C.-F. Schleussner, M. Foerster, F. Langhojer, P. Nuernberger, and T. Brixner, "Coherent two-dimensional ultraviolet spectroscopy in fully noncollinear geometry," Optics letters **35**, 4178-4180 (2010).

95. B. A. West, and A. M. Moran, "Two-dimensional electronic spectroscopy in the ultraviolet wavelength range," The journal of physical chemistry letters **3**, 2575-2581 (2012).

96. D. J. Kane, A. Taylor, R. Trebino, and K. DeLong, "Single-shot measurement of the intensity and phase of a femtosecond UV laser pulse with frequency-resolved optical gating," Optics letters **19**, 1061-1063 (1994).

97. K. Michelmann, T. Feurer, R. Fernsler, and R. Sauerbrey, "Frequency resolved optical gating in the UV using the electronic Kerr effect," Applied Physics B **63**, 485-489 (1996).

98. S. Backus, J. Peatross, Z. Zeek, A. Rundquist, G. Taft, M. M. Murnane, and H. C. Kapteyn, "16-fs, 1-μJ ultraviolet pulses generated by third-harmonic conversion in air," Optics letters **21**, 665-667 (1996).

99. T. S. Clement, A. Taylor, and D. J. Kane, "Single-shot measurement of the amplitude and phase of ultrashort laser pulses in the violet," Optics letters **20**, 70-72 (1995).

100. O. Dühr, E. Nibbering, G. Korn, G. Tempea, and F. Krausz, "Generation of intense 8-fs pulses at 400?? nm," Optics letters **24**, 34-36 (1999).

101. C. G. Durfee, S. Backus, H. C. Kapteyn, and M. M. Murnane, "Intense 8-fs pulse generation in the deep ultraviolet," Optics letters **24**, 697-699 (1999).

102. J. Liu, K. Okamura, Y. Kida, T. Teramoto, and T. Kobayashi, "Clean sub-8-fs pulses at 400 nm generated by a hollow fiber compressor for ultraviolet ultrafast pump-probe spectroscopy," Optics express **18**, 20645-20650 (2010).

103. A. Ermolov, H. Valtna-Lukner, J. Travers, and P. St.J. Russell, "Characterization of few-fs deep-UV dispersive waves by ultra-broadband transient-grating XFROG," Optics Letters **41**, 5535-5538 (2016).

104. D. Lee, S. Akturk, P. Gabolde, and R. Trebino, "Experimentally simple, extremely broadband transient-grating frequency-resolved-optical-gating arrangement," Optics express **15**, 760-766 (2007).

105. D. Lee, P. Gabolde, and R. Trebino, "Toward single-shot measurement of a broadband ultrafast continuum," J. Opt. Soc. Am. B **25**, A34-A40 (2008).

106. T. Nagy, and P. Simon, "Single-shot TG FROG for the characterization of ultrashort DUV pulses," Optics express **17**, 8144-8151 (2009).

107. M. Isinger, D. Busto, S. Mikaelsson, S. Zhong, C. Guo, P. Salières, C. Arnold, A. l'Huillier, and M. Gisselbrecht, "Accuracy and precision of the RABBIT technique," Philosophical Transactions of the Royal Society A **377**, 20170475 (2019).

108. R. Itakura, T. Kumada, M. Nakano, and H. Akagi, "Frequency-resolved optical gating for characterization of VUV pulses using ultrafast plasma mirror switching," Opt Express **23**, 10914-10924 (2015).

109. "RefractiveIndex.Info: Refractive Index Database, Optical constants of SF11," https://refractiveindex.info/?shelf=glass&book=SF11&page=SCHOTT.

110. A. Baltuska, M. S. Pshenichnikov, and D. A. Wiersma, "Second-harmonic generation frequency-resolved optical gating in the single-cycle regime," IEEE Journal of Quantum Electronics **35**, 459-478 (1999).

111. M. Li, J. P. Nibarger, C. Guo, and G. N. Gibson, "Dispersion-free transient-grating frequency-resolved optical gating," Applied optics **38**, 5250-5253 (1999).

112. F. Capotondi, L. Foglia, M. Kiskinova, C. Masciovecchio, R. Mincigrucci, D. Naumenko, E. Pedersoli, A. Simoncig, and F. Bencivenga, "Characterization of ultrafast free-electron laser pulses using extreme-ultraviolet transient gratings," J Synchrotron Radiat **25**, 32-38 (2018).

113. T. Brabec, and F. Krausz, "Intense few-cycle laser fields: Frontiers of nonlinear optics," Reviews of Modern Physics **72**, 545 (2000).

114. E. Allaria, R. Appio, L. Badano, W. A. Barletta, S. Bassanese, S. G. Biedron, A. Borga, E. Busetto, D. Castronovo, P. Cinquegrana, S. Cleva, D. Cocco, M. Cornacchia,

P. Craievich, I. Cudin, G. D'Auria, M. Dal Forno, M. B. Danailov, R. De Monte, G. De Ninno, P. Delgiusto, A. Demidovich, S. Di Mitri, B. Diviacco, A. Fabris, R. Fabris, W. Fawley, M. Ferianis, E. Ferrari, S. Ferry, L. Froehlich, P. Furlan, G. Gaio, F. Gelmetti, L. Giannessi, M. Giannini, R. Gobessi, R. Ivanov, E. Karantzoulis, M. Lonza, A. Lutman, B. Mahieu, M. Milloch, S. V. Milton, M. Musardo, I. Nikolov, S. Noe, F. Parmigiani, G. Penco, M. Petronio, L. Pivetta, M. Predonzani, F. Rossi, L. Rumiz, A. Salom, C. Scafuri, C. Serpico, P. Sigalotti, S. Spampinati, C. Spezzani, M. Svandrlik, C. Svetina, S. Tazzari, M. Trovo, R. Umer, A. Vascotto, M. Veronese, R. Visintini, M. Zaccaria, D. Zangrando, and M. Zangrando, "Highly coherent and stable pulses from the FERMI seeded free-electron laser in the extreme ultraviolet," Nature Photonics **6**, 699-704 (2012).

115.   K. Tiedtke, A. Azima, N. von Bargen, L. Bittner, S. Bonfigt, S. Düsterer, B. Faatz, U. Frühling, M. Gensch, C. Gerth, N. Guerassimova, U. Hahn, T. Hans, M. Hesse, K. Honkavaar, U. Jastrow, P. Juranic, S. Kapitzki, B. Keitel, T. Kracht, M. Kuhlmann, W. B. Li, M. Martins, T. Núñez, E. Plönjes, H. Redlin, E. L. Saldin, E. A. Schneidmiller, J. R. Schneider, S. Schreiber, N. Stojanovic, F. Tavella, S. Toleikis, R. Treusch, H. Weigelt, M. Wellhöfer, H. Wabnitz, M. V. Yurkov, and J. Feldhaus, "The soft x-ray free-electron laser FLASH at DESY: beamlines, diagnostics and end-stations," New Journal of Physics **11**, 023029 (2009).

116.   F. Krausz, and M. Ivanov, "Attosecond physics," Reviews of Modern Physics **81**, 163 (2009).

117.   K. Ramasesha, S. R. Leone, and D. M. Neumark, "Real-Time Probing of Electron Dynamics Using Attosecond Time-Resolved Spectroscopy," **67**, 41-63 (2016).

118.   E. T. J. Nibbering, H. Fidder, and E. Pines, "ULTRAFAST CHEMISTRY: Using Time-Resolved Vibrational Spectroscopy for Interrogation of Structural Dynamics," **56**, 337-367 (2005).

119.   D. F. Gardner, M. Tanksalvala, E. R. Shanblatt, X. Zhang, B. R. Galloway, C. L. Porter, R. Karl Jr, C. Bevis, D. E. Adams, H. C. Kapteyn, M. M. Murnane, and G. F. Mancini, "Subwavelength coherent imaging of periodic samples using a 13.5 nm tabletop high-harmonic light source," Nature Photonics **11**, 259-263 (2017).

120.   K. W. DeLong, C. L. Ladera, R. Trebino, B. Kohler, and K. R. Wilson, "Ultrashort-pulse measurement using noninstantaneous nonlinearities: Raman effects in frequency-resolved optical gating,," Opt. Lett. **20**, 486-488 (1995).

121.   R. P. Prasankumar, and A. J. Taylor, *Optical techniques for solid-state materials characterization* (CRC Press, 2016).

122.   J. Itatani, F. Quéré, G. L. Yudin, M. Y. Ivanov, F. Krausz, and P. B. Corkum, "Attosecond Streak Camera," Physical Review Letters **88**, 173903 (2002).

123. H. Valtna-Lukner, F. Belli, A. Ermolov, F. Kottig, K. F. Mak, F. Tani, J. C. Travers, and P. S. J. Russell, "Extremely broadband single-shot cross-correlation frequency-resolved optical gating using a transient grating as gate and dispersive element," Rev Sci Instrum **88**, 073106 (2017).

124. D. Kane, N. Hartmann, R. Coffee, and A. Fry, *Experimental and analysis considerations for transmission/reflection spectrograms used in ultrafast x-ray pulse diagnostics* (SPIE, 2016).

125. N. P. Inc., "Newlight Photonics Inc., Newlight Photonics: Fused Silica (SiO2) Windows/Rods," https://www.newlightphotonics.com/Optical-Windows-Rods/Fused-Silica-Windows-Rods.

126. T. C. Wong, J. Ratner, V. Chauhan, J. Cohen, P. M. Vaughan, L. Xu, A. Consoli, and R. Trebino, "Simultaneously measuring two ultrashort laser pulses on a single-shot using double-blind frequency-resolved optical gating," JOSA B **29**, 1237-1244 (2012).

127. A. Leblanc, P. Lassonde, S. Petit, J. C. Delagnes, E. Haddad, G. Ernotte, M. R. Bionta, V. Gruson, B. E. Schmidt, H. Ibrahim, E. Cormier, and F. Légaré, "Phase-matching-free pulse retrieval based on transient absorption in solids," Optics Express **27**, 28998-29015 (2019).

128. W. Peters, T. Jones, A. Efimov, E. Pedersoli, L. Foglia, R. Mincigrucci, I. Nikolov, R. Trebino, R. Sandberg, M. Danailov, F. Capotondi, F. Bencivenga, and P. Bowlan, "Single-shot Measurement of Extreme Ultraviolet Free Electron Laser Pulses," in *Conference on Lasers and Electro-Optics*(Optical Society of America, Washington, DC, 2020), p. FW4D.3.

129. W. Helml, I. Grguraš, P. N. Juranić, S. Düsterer, T. Mazza, A. R. Maier, N. Hartmann, M. Ilchen, G. Hartmann, and L. Patthey, "Ultrashort free-electron laser x-ray pulses," Applied Sciences **7**, 915 (2017).

130. C. Bostedt, S. Boutet, D. M. Fritz, Z. Huang, H. J. Lee, H. T. Lemke, A. Robert, W. F. Schlotter, J. J. Turner, and G. J. Williams, "Linac coherent light source: The first five years," Reviews of Modern Physics **88**, 015007 (2016).

131. S. Düsterer, M. Rehders, A. Al-Shemmary, C. Behrens, G. Brenner, O. Brovko, M. DellAngela, M. Drescher, B. Faatz, J. Feldhaus, U. Frühling, N. Gerasimova, N. Gerken, C. Gerth, T. Golz, A. Grebentsov, E. Hass, K. Honkavaara, V. Kocharian, M. Kurka, T. Limberg, R. Mitzner, R. Moshammer, E. Plönjes, M. Richter, J. Rönsch-Schulenburg, A. Rudenko, H. Schlarb, B. Schmidt, A. Senftleben, E. A. Schneidmiller, B. Siemer, F. Sorgenfrei, A. A. Sorokin, N. Stojanovic, K. Tiedtke, R. Treusch, M. Vogt, M. Wieland, W. Wurth, S. Wesch, M. Yan, M. V. Yurkov, H. Zacharias, and S. Schreiber, "Development of experimental techniques for the characterization of ultrashort photon pulses of extreme ultraviolet free-electron lasers," Physical Review Special Topics - Accelerators and Beams **17**, 120702 (2014).

132. R. N. Coffee, J. P. Cryan, J. Duris, W. Helml, S. Li, and A. Marinelli, "Development of ultrafast capabilities for X-ray free-electron lasers at the linac coherent light source," Philosophical Transactions of the Royal Society A: Mathematical, Physical and Engineering Sciences **377**, 20180386 (2019).

133. N. Hartmann, G. Hartmann, R. Heider, M. S. Wagner, M. Ilchen, J. Buck, A. O. Lindahl, C. Benko, J. Grünert, J. Krzywinski, J. Liu, A. A. Lutman, A. Marinelli, T. Maxwell, A. A. Miahnahri, S. P. Moeller, M. Planas, J. Robinson, A. K. Kazansky, N. M. Kabachnik, J. Viefhaus, T. Feurer, R. Kienberger, R. N. Coffee, and W. Helml, "Attosecond time–energy structure of X-ray free-electron laser pulses," Nature Photonics **12**, 215-220 (2018).

134. P. Finetti, H. Höppner, E. Allaria, C. Callegari, F. Capotondi, P. Cinquegrana, M. Coreno, R. Cucini, M. B. Danailov, A. Demidovich, G. De Ninno, M. Di Fraia, R. Feifel, E. Ferrari, L. Fröhlich, D. Gauthier, T. Golz, C. Grazioli, Y. Kai, G. Kurdi, N. Mahne, M. Manfredda, N. Medvedev, I. P. Nikolov, E. Pedersoli, G. Penco, O. Plekan, M. J. Prandolini, K. C. Prince, L. Raimondi, P. Rebernik, R. Riedel, E. Roussel, P. Sigalotti, R. Squibb, N. Stojanovic, S. Stranges, C. Svetina, T. Tanikawa, U. Teubner, V. Tkachenko, S. Toleikis, M. Zangrando, B. Ziaja, F. Tavella, and L. Giannessi, "Pulse Duration of Seeded Free-Electron Lasers," Physical Review X **7**, 021043 (2017).

135. A. A. Zholents, and W. M. Fawley, "Proposal for Intense Attosecond Radiation from an X-Ray Free-Electron Laser," Physical Review Letters **92**, 224801 (2004).

136. A. A. Lutman, T. J. Maxwell, J. P. MacArthur, M. W. Guetg, N. Berrah, R. N. Coffee, Y. Ding, Z. Huang, A. Marinelli, S. Moeller, and J. C. U. Zemella, "Fresh-slice multicolour X-ray free-electron lasers," Nature Photonics **10**, 745-750 (2016).

137. M. Kowalewski, B. P. Fingerhut, K. E. Dorfman, K. Bennett, and S. Mukamel, "Simulating Coherent Multidimensional Spectroscopy of Nonadiabatic Molecular Processes: From the Infrared to the X-ray Regime," Chemical Reviews **117**, 12165-12226 (2017).

138. C. Svetina, R. Mankowsky, G. Knopp, F. Koch, G. Seniutinas, B. Rösner, A. Kubec, M. Lebugle, I. Mochi, M. Beck, C. Cirelli, J. Krempasky, C. Pradervand, J. Rouxel, G. F. Mancini, S. Zerdane, B. Pedrini, V. Esposito, G. Ingold, U. Wagner, U. Flechsig, R. Follath, M. Chergui, C. Milne, H. T. Lemke, C. David, and P. Beaud, "Towards X-ray transient grating spectroscopy," Optics Letters **44**, 574-577 (2019).

139. T. E. Glover, D. M. Fritz, M. Cammarata, T. K. Allison, S. Coh, J. M. Feldkamp, H. Lemke, D. Zhu, Y. Feng, R. N. Coffee, M. Fuchs, S. Ghimire, J. Chen, S. Shwartz, D. A. Reis, S. E. Harris, and J. B. Hastings, "X-ray and optical wave mixing," Nature **488**, 603-608 (2012).

140. F. Bencivenga, F. Capotondi, R. Mincigrucci, R. Cucini, M. Manfredda, E. Pedersoli, E. Principi, A. Simoncig, and C. Masciovecchio, "Nonlinear optics with coherent free electron lasers," Physica Scripta **T169**, 014003 (2016).

141. I. Grguraš, A. R. Maier, C. Behrens, T. Mazza, T. J. Kelly, P. Radcliffe, S. Düsterer, A. K. Kazansky, N. M. Kabachnik, T. Tschentscher, J. T. Costello, M. Meyer, M. C. Hoffmann, H. Schlarb, and A. L. Cavalieri, "Ultrafast X-ray pulse characterization at free-electron lasers," Nature Photonics **6**, 852-857 (2012).

142. U. Frühling, M. Wieland, M. Gensch, T. Gebert, B. Schütte, M. Krikunova, R. Kalms, F. Budzyn, O. Grimm, J. Rossbach, E. Plönjes, and M. Drescher, "Single-shot terahertz-field-driven X-ray streak camera," Nature Photonics **3**, 523-528 (2009).

143. R. Mitzner, A. A. Sorokin, B. Siemer, S. Roling, M. Rutkowski, H. Zacharias, M. Neeb, T. Noll, F. Siewert, W. Eberhardt, M. Richter, P. Juranic, K. Tiedtke, and J. Feldhaus, "Direct autocorrelation of soft-x-ray free-electron-laser pulses by time-resolved two-photon double ionization of He," Physical Review A **80**, 025402 (2009).

144. A. A. Maznev, T. F. Crimmins, and K. A. Nelson, "How to make femtosecond pulses overlap," Optics Letters **23**, 1378-1380 (1998).

145. Z. Bor, B. Racz, G. Szabo, M. Hilbert, and H. Hazim, "Femtosecond pulse front tilt caused by angular dispersion," Optical Engineering **32** (1993).

146. S. Akturk, X. Gu, P. Gabolde, and R. Trebino, "The general theory of first-order spatio-temporal distortions of Gaussian pulses and beams," Optics Express **13**, 8642-8661 (2005).

147. A. Leblanc, P. Lassonde, S. Petit, J. C. Delagnes, E. Haddad, G. Ernotte, M. R. Bionta, V. Gruson, B. E. Schmidt, H. Ibrahim, E. Cormier, and F. Legare, "Phase-matching-free pulse retrieval based on transient absorption in solids," Opt Express **27**, 28998-29015 (2019).

148. C. Gahl, A. Azima, M. Beye, M. Deppe, K. Döbrich, U. Hasslinger, F. Hennies, A. Melnikov, M. Nagasono, A. Pietzsch, M. Wolf, W. Wurth, and A. Föhlisch, "A femtosecond X-ray/optical cross-correlator," Nature Photonics **2**, 165-169 (2008).

149. R. Riedel, A. Al-Shemmary, M. Gensch, T. Golz, M. Harmand, N. Medvedev, M. J. Prandolini, K. Sokolowski-Tinten, S. Toleikis, U. Wegner, B. Ziaja, N. Stojanovic, and F. Tavella, "Single-shot pulse duration monitor for extreme ultraviolet and X-ray free-electron lasers," Nature Communications **4**, 1731 (2013).

150. M. Schultze, M. Fiess, N. Karpowicz, J. Gagnon, M. Korbman, M. Hofstetter, S. Neppl, A. L. Cavalieri, Y. Komninos, T. Mercouris, C. A. Nicolaides, R. Pazourek, S. Nagele, J. Feist, J. Burgdorfer, A. M. Azzeer, R. Ernstorfer, R. Kienberger, U.

Kleineberg, E. Goulielmakis, F. Krausz, and V. S. Yakovlev, "Delay in photoemission," Science **328**, 1658-1662 (2010).

Title: COMPLETE TEMPORAL MEASUREMENT OF LOW-INTENSITY AND HIGH-FREQUENCY ULTRASHORT LASER PULSES

Author(s):   Jones, Travis Nathaniel

Intended for: Doctoral Thesis

Issued: 2020-11-09 (Draft)